

Superconducting Hot Electron Bolometers on Silicon Nitride Membranes for Terahertz Waveguide Mixers

Inaugural-Dissertation
zur
Erlangung des Doktorgrades
der Mathematisch-Naturwissenschaftlichen Fakultät
der Universität zu Köln

vorgelegt von
Michael Brandt
aus London (GB)

Köln 2004

Berichterstatter: Prof. Dr. Jürgen Stutzki
Prof. Dr. Peter Reiter

Tag der letzten mündlichen Prüfung: 28.06.2004

Contents

1	Abstract/Kurzzusammenfassung	1
1.1	Kurzzusammenfassung	1
1.2	Abstract	3
2	Introduction	5
2.1	Terahertz astronomy	5
2.2	THz detectors	7
3	THz waveguide heterodyne mixers theory	10
3.1	Heterodyne detection principle	10
3.2	THz waveguide-mixer concept	11
3.2.1	Setup	11
3.2.2	Comparison of waveguides and quasi-optics	11
3.2.3	Scaling of waveguide mixers	13
4	Hot electron bolometer mixers theory	14
4.1	Bolometer principle	14
4.2	Bolometer heterodyne mixers	15
4.3	Superconducting Hot Electron Bolometers	16
4.3.1	Hot Electron gas in thin superconducting films	18
4.3.2	Lumped element HEB model	19
4.3.3	Hot-spot model	19
4.4	Cooling mechanisms in HEBs	20
4.4.1	The two main cooling mechanisms	20
4.4.2	Phonon cooled Hot Electron Bolometers	21
4.4.3	Diffusion cooled Hot Electron Bolometers	22
	Hot-spot model with diffusion cooling	24
4.5	Self-heating and electro-thermal feedback	25

4.6	Conversion gain of HEBs	29
4.7	Noise	30
4.7.1	Johnson noise	30
4.7.2	Fluctuation noise	31
4.8	Bandwidth	31
5	Development of Hot Electron Bolometer mixers on freestanding membranes strips	34
5.1	Fabrication concepts A and B - an overview	34
5.2	Thermal conductivity in freestanding membrane micro structures . . .	37
5.2.1	Introduction	37
5.2.2	Heat transfer process	38
5.2.3	Surface scattering of phonons in thin membranes	38
5.2.4	Estimated thermal transport in the membrane mixer	40
5.3	Production of membranes together with support frames - Concept A	42
5.4	GaAs based membranes	42
5.5	Silicon based membranes	44
5.5.1	Silicon and Silicon Nitride membrane structuring	44
	Silicon Nitride membrane development and fabrication	45
	Silicon membrane development	45
5.5.2	Si frame structuring	46
	Anisotropic base wet etch etching	46
	Hydrofluoric wet etching	47
	Porous Silicon etching	48
5.6	Concept A - results	49

6	Development of HEB mixers on freestanding membranes using "flip-chip" mounting	51
6.1	Separate fabrication of Si ₃ N ₄ membranes and support frames - Concept B	51
6.2	Mixer device design and fabrication concept for freestanding membranes	53
6.3	Si ₃ N ₄ etch process development	53
6.4	Si ₃ N ₄ etch mask development	54
6.4.1	AZ series photo resist multi-layer RIE etch mask	54
6.4.2	AZ/SU-8 resist multi-layer RIE etch mask	55
6.4.3	AZ-resist/Cu/AZ-resist multi-layer	56
6.5	Self-aligned lift-off for backside etch-stop	57
6.6	Intermediate DC-characterization	59
6.7	Backside etch of Silicon base wafer	59
6.7.1	Process development	59
6.7.2	Membrane Fabrication	60
6.7.3	Fabrication of the silicon support frames	61
6.8	"Flip-chip" membrane bonding	61
6.8.1	Handling and positioning of the device membrane structure .	61
6.8.2	"Flip-chip" bonding of the device membrane	63
6.8.3	Final assembly and fine-positioning of the frame/membrane unit	63
6.9	Summary, conclusion and outlook of the membrane substrate concept	65
7	Fabrication of waveguide structures and feed horns for THz frequencies	66
7.1	Basic waveguide theory	66
7.2	Waveguide technology development for 2 THz	69
7.3	Classic fabrication of copper waveguide structures at the KOSMA workshop	69
7.4	Further approaches for THz waveguides	70
7.5	2 THz waveguide antenna horns	71
7.6	Summary and status	72
7.7	KOSMA Micro Assembly Stage for waveguide device mounting . . .	73

8	HEB mixer development and fabrication	75
8.1	RF design simulation and development with CST	75
8.2	Fabrication of HEB mixers on Si_3N_4 membranes	78
9	DC measurements - Setup development and device characterization	82
9.1	Current vs. Voltage curves measurement setup	82
9.2	Interpretation and discussion of I/V measurements	83
9.3	Resistance-vs-Temperature measurement setup	86
9.3.1	Measurement principle	86
9.3.2	R/T measurement setup realization	86
9.3.3	Performing the measurements	88
9.3.4	Van der Pauw measurements of sheet resistance	89
9.4	Interpretation and discussion of R/T measurements	89
9.5	DC measurements interpretation	91
9.5.1	Comparison of different devices	91
9.5.2	Comparison of different batches in membrane technology	95
9.5.3	Comparison of devices made on Si_3N_4 membranes and on fused quartz	97
9.6	Thermal coupling of mixer device and copper mixer block	98
9.7	Summary and conclusions of the DC measurements	100
10	Heterodyne measurements of HEB mixers on freestanding membranes	102
10.1	Heterodyne setup description and basic theory	102
10.1.1	Heterodyne measurement setup	102
10.1.2	Sensitivity of a heterodyne receiver system	104
10.1.3	Noise contribution and losses in the heterodyne receiver	106
10.2	Mixer measurements of diffusion cooled HEBs on membranes	107
10.2.1	Sensitivity and stability of diffusion cooled HEBs on membranes	107
10.2.2	Direct comparison of D-HEBs on membranes and on fused quartz	109

10.2.3	D-HEB mixer performance at different bath temperatures . . .	111
10.2.4	IF bandwidth measurements of D-HEBs	112
10.3	Mixer measurements of phonon cooled HEBs on membranes	114
10.3.1	Sensitivity and stability of phonon cooled HEBs on membranes	114
10.3.2	IF bandwidth measurement of P-HEBs on membranes	115
10.4	Fourier Transform Spectrometer measurements FTS	117
10.4.1	Introduction	117
10.4.2	FTS setup	117
10.4.3	FTS measurements of D-HEBs and P-HEBs	118
10.4.4	Comparison of FTS results and CST simulations	121
10.5	Final discussion of the RF measurements	124
11	Finite element simulation of diffusion cooling in HEBs	126
11.1	Problem description	126
11.2	HEB response and its dependence on the biasing conditions	128
11.3	Simulation concept	129
11.4	Simulation routine	130
11.5	Simulation results and comparison with measurements	133
11.6	Pre-selection of devices on the basis of dipstick measurements and simulations	137
11.7	Summary and conclusion	138
12	Waveguide membrane mixer operation at the KOSMA telescope	139
13	Conclusion and Outlook	140
	Appendix	141
A	Electro/thermal feedback	142
B	Mixer Gain	144

C Fabrication and measurement data base for advanced process development	147
C.1 Data Base Concept	147
C.2 Data Base realization	149
D Micro Production Line on the Hannover Fair Industry	149
Literaturverzeichnis/References	152
Danksagung	158
Erklärung	160

1 Abstract/Kurzzusammenfassung

1.1 Kurzzusammenfassung

Gegenstand dieser Arbeit ist die Entwicklung von supraleitenden Hot Electron Bolometer (HEB) Mischerelementen auf freistehenden Membransubstraten für den Einsatz in hochauflösenden Heterodyn-Empfangssystemen für den Terahertzbereich.

Das THz-Frequenzband ist bisher für die Radioastronomie nur wenig erschlossen. Im Augenblick wird hier mit viel Aufwand an neuartigen Teleskop- sowie Detektortechnologien gearbeitet. Diese Arbeit konzentriert sich auf die Entwicklung von THz-Hohlleitermischern mit supraleitenden Hot Electron Bolometern (HEB) auf freistehenden Silizium-Nitrid (Si_3N_4) Membranen. Diese sind in erster Linie für das Flugzeug-Observatorium SOFIA (1.9 THz) und das Atacama Pathfinder EXperiment (APEX) Teleskop (1.4 THz) in Nordchile bestimmt.

Hohlleitermischer mit Rillenhörnern haben den Vorteil einer guten Kopplung an den gaußförmigen Teleskopstrahl, sind aber eine technische Herausforderung für THz-Frequenzen wegen der winzigen Hohlleiter- und Bauteilabmessungen. Hohlleiter können mit (Silizium-)Mikromechanik für THz-Frequenzen skaliert werden, aber die Skalierung des dielektrischen Substrates, klassischerweise Quarz, für Frequenzen oberhalb 1.5 THz ist sehr schwierig.

Um Hochfrequenz-(HF-)Verluste durch Hohlleitermoden im Substratkanal zu vermeiden, darf das Quarz-Substrat bei 1.9 THz höchstens 10 Mikrometer dick sein. Erheblich dünnere Substrate können erreicht werden, wenn das Mischerelement auf einer dünnen ($2\ \mu\text{m}$) Membranschicht, aufgewachsen oder aufgetragen auf einen massiven Siliziumwafer, hergestellt wird. Diese Membran wird dann in Streifen strukturiert, welche als Substrate für die Mischerelemente benutzt werden.

Im Rahmen dieser Arbeit wurden zwei Konzepte für die Herstellung dieser Membranzustrukturen entwickelt, wobei nur eins für die HEB-Fertigung verwendet wurde.

Im ersten Konzept wird durch rückseitiges Ätzen das Silizium-Vollmaterial entfernt und nur die Membranstreifen und dazugehörige Vollmaterial-Rahmen als Stabilisierung bleiben übrig. Diese Rahmen werden verwendet, um die Mischerelemente in den Mischerblock zu kleben. Ein Nachteil dieses Rahmen/Membran-Konzepts ist der relativ hohe Platzbedarf der Stabilisierungsrahmen. Da der Fertigungsprozess für die THz-Mischerelemente nur eine sehr geringe Ausbeute hat, sind die Chancen, eine genügende Anzahl guter und - wichtig für Array-Anwendungen - gleichartiger Bauteile zu erhalten, sehr gering. Außerdem ist es sehr schwierig, die Mischerelemente vor der anisotropen Ätzlösung (KOH oder TMAH über 60°C) zu schützen.

Daher wurde das zweite Konzept entwickelt, bei dem die Rahmen und die Mischerelement-Membranen separat hergestellt werden. Anschließend werden die $2\ \mu\text{m}$ dicken

Mischer-element-Membranen mit einer angepassten "Flip-Chip" Technologie auf den separat gefertigten Rahmen gebondet. Mit diesem zweiten Konzept können mehrere hundert HEB Mischer-elemente auf einem 1 Zoll Wafer prozessiert und geätzt werden. Mit diesem Fertigungskonzept wurden sowohl diffusions- und als auch phononen-gekühlte Hot Electron Bolometer Mischer auf freistehenden Si_3N_4 Membranenstreifen erfolgreich gefertigt. Mit der KOSMA Mikromontage-Station, die im Rahmen dieser Arbeit entwickelt wurde, können diese Membran-Mischer-elemente gehandhabt und präzise im Halbleiterblock positioniert werden.

3D-EM-Feldsimulationen wurden verwendet, um das HF-Design an die Membrantechnologie anzupassen. Um die Mischer-elemente für die Fertigungsentwicklung genauer charakterisieren zu können, wurden neue DC-Messsysteme entwickelt. In den DC-Messungen wurden keine Anzeichen gefunden, dass der Membran-Prozess die Bauteilcharakteristik der HEBs verschlechtert.

Es wurde ein Programm für die Finite-Elemente-Simulation von diffusions-gekühlten HEBs geschrieben und erfolgreich getestet. Die simulierten Strom/Spannungskennlinien (I/U) der HEBs unter HF Einstrahlung zeigen eine qualitative Übereinstimmung mit den gemessenen Daten. Insbesondere die Ableitung dU/dI , die als Indikator für die HEB Mischerempfindlichkeit verwendet werden kann, zeigt ähnliche Charakteristiken.

Die DC- und HF-Heterodyn Bauteilcharakteristiken der diffusions-gekühlten HEBs sind denen der auf Quarzsubstraten gefertigten sehr ähnlich. Eine Empfängerrauschtemperatur von 2000 K bei 800 GHz HF wurde mit diffusions-gekühlten HEBs auf Membranen unter stabilen Biasbedingungen gemessen. Die ZF-Bandbreitenmessungen zeigten keinen Roll-off bis 4 GHz.

Das beste Heterodyn-Ergebnis der phononen-gekühlten HEBs zeigte eine Rauschtemperatur von 1000 K bei 1 GHz ZF und einer 3dB Rauschbandbreite von 1.6 GHz.

Dies sind die ersten erfolgreichen Heterodyn Messungen mit supraleitenden diffusions- und phonon-gekühlten HEBs auf freistehenden Si_3N_4 Membranen in Halbleitertechnik. Damit wird eine Membrantechnologie für Mischer-elemente vorgestellt, die für einen 1.9 THz (SOFIA)-Mischer und höher skalierbar ist.

Ein 800 GHz HEB Mischer in Membrantechnologie wurde am KOSMA Teleskop (SMART Empfänger) auf dem Gornergrat (Zermatt, Schweiz) eingebaut und betrieben. Allan-Varianz-Messungen zeigten eine ähnliche Stabilität wie die Supraleiter/Normalleiter/Supraleiter (SIS) Kanäle und der LO Leistungsbedarf des Bolometers lag einen Faktor 5-10 niedriger als der der SIS Mischer. Spektrallinien des Kohlenmonoxid Übergangs $J=7-6$ wurden in Richtung der Galaktischen Quellen DR21 und W51 mit diesem HEB Mischer gemessen.

1.2 Abstract

The topic of this work is the development of Hot Electron Bolometer (HEB) mixers on freestanding membrane substrates for terahertz high resolution heterodyne receiver systems.

The radio astronomy in the THz frequency spectrum is still in the beginning. At present much effort is put into the development of novel telescopes as well as in detector technologies. This work focuses on the development of THz waveguide detectors with superconducting Hot Electron Bolometer (HEB) mixers. These are primarily aimed for the use in the airborne Stratospheric Observatory For Infrared Astronomy (SOFIA) (1.9 THz) and the Atacama Pathfinder EXperiment (APEX) telescope (1.4 THz) in northern Chile.

Waveguide mixers with corrugated feedhorns have the advantage of very good coupling to the telescope gaussian beam, but are technically demanding at THz frequencies due to the small waveguide and device substrate dimensions. Waveguides can be scaled to Terahertz frequencies with (Silicon-) micro-machining methods, but scaling the dielectric substrate, traditionally made of quartz, to frequencies beyond 1.5 THz is very difficult.

In order to avoid RF loss due to waveguide modes in the substrate channel, a quartz substrate at 1.9 THz would have to be at most 10 microns thin. Considerably thinner substrates are possible by fabricating the mixer device on a thin ($2\ \mu\text{m}$) membrane layer deposited or grown on a bulk silicon wafer. The membrane is subsequently structured into thin strips which are used as substrates for the devices.

In the context of this work two concepts for the fabrication of these membrane structures have been developed whereby only one of them has been used for the HEB fabrication.

In the first concept the support wafer is removed by backside etching, leaving only the membrane strips and frames of bulk material for support. The frames are used to glue the devices into a copper waveguide mixer mount. One disadvantage of the frame/membrane concept is the relatively large wafer area occupied by the support frames. As the process for the THz mixer devices has only limited yield, the chances of producing a sufficient number of good and - important for array receivers- identical devices are rather poor. Also, it is rather difficult to protect the devices from the anisotropic etch solution used for back-etching the frames (KOH or TMAH above 60°C).

Hence the second concept has been developed in which the frame fabrication is separated from the membrane device fabrication. A modified "flip-chip" process is used to subsequently bond the $2\ \mu\text{m}$ thick membrane device strips to a silicon frame fabricated separately. For future silicon micro-machined waveguides, the support frame is probably not necessary at all. With this concept diffusion cooled and phonon cooled

Hot Electron Bolometers have been fabricated on freestanding Silicon Nitride (Si_3N_4) membrane strips. With the KOSMA Micro Assembly Station which has been developed in this work, these membrane mixer elements can be securely handled and positioned into the copper waveguide mount.

3D EM simulations have been used to adapt the RF design to the membrane technology. New DC measurement setups have been designed and built to improve the characterization of HEBs and, additionally, of SIS devices. The DC measurements have not indicated that the membrane process degrades the HEB device characteristics.

A program for simple finite element simulations of diffusion cooled HEBs has been written and successfully tested. The simulated characteristic I/V curves of the HEBs show qualitative agreement with the measured data. Especially the dU/dI derivative, which can be used as an indicator for the HEB mixer response, shows similar characteristics.

The measured DC and RF heterodyne device characteristics of the diffusion cooled HEBs are very similar to bolometers fabricated on quartz substrates. A receiver noise temperature of 2000 K at 800 GHz RF has been measured with diffusion cooled HEBs on membranes under stable bias conditions. IF bandwidth measurements did not show a gain roll-off below 4 GHz.

The best heterodyne results of phonon cooled HEBs showed a receiver noise temperature of 1000 K at 1 GHz IF and a 3dB noise bandwidth of 1.6 GHz.

These are the first successful heterodyne measurements of superconducting diffusion and phonon cooled HEBs on freestanding Si_3N_4 membranes with waveguide technology. With it a membrane technology for mixer elements is presented which can be scaled to 1.9 THz (SOFIA-mixer) and beyond.

A phonon cooled HEB mixer on a freestanding membrane was subsequently mounted and used at the KOSMA telescope (SMART receiver) on Gornergrat (Zermatt, Schweiz). Allan variance measurements showed similar stability to the superconductor/normal conductor/superconductor (SIS) channels, and the LO power for the Bolometer was about a factor of 5-10 less than that of the SIS mixers. Spectral lines of the J=7-6 Carbon Monoxide transition have been measured towards the galactic sources DR21 and W51 with this HEB-mixer.

2 Introduction

2.1 Terahertz astronomy

Radio astronomy is a powerful tool to analyze the chemical and physical conditions of molecular clouds in the universe. Not only different types of molecules can be distinguished, but also various physical parameters of the environment like density, temperature profiles and dynamics can be determined. In the frequency range up to 900 GHz extensive observations have been performed in recent years which have led to important astronomical findings. Above 900 GHz, in the Far InfraRed (FIR) region, only little data have been gathered due to increasing technological difficulties and the poor transparency of the Earth's atmosphere in this frequency range. New sensitive detectors and telescope technologies are necessary to open up this field for scientific research.

The Far Infrared spectrum is very interesting, because here many cooling lines can be found. The three strongest lines which have been detected between 0.3 and 3 THz in preliminary observations of our Galaxy [1], have been traced to single ionized Carbon (CII) at 1.9 THz and single ionized Nitrogen (NII) at 1.5 and 2.5 THz, respectively. Suggested sources of CII emission are, for example, Photon Dominated Regions (PDRs) on the surface of molecular clouds. FIR astronomy of CII not only promises new knowledge about the birth and development of young stars, but also about the development of shock fronts in Photon Dominated Regions (PDRs) [2]. With observations of NII the Warm Interstellar Medium (WIM) might be studied. Another interesting field for observation are young galaxies at the rim of the universe. Here spectral lines, which originally had been in the visible or infrared range, have been red-shifted towards the THz range.

Large parts of the radio frequency spectrum cannot be observed from the ground, because the signals are absorbed in the earth atmosphere, mainly by O₂ and H₂O molecules. There are only few frequency windows, where the atmosphere becomes partly transparent and observations are possible. Thus dry high altitude locations have to be chosen, where the atmosphere becomes thinner and less molecules are found in the line of sight. Several ground based observatories like the Kölner Observatorium für Submillimeter Astronomie (KOSMA) (Gornergrat/ Switzerland altitude 3150m) or the Heinrich Hertz SubMillimeter Telescope (HHSMT) (Mt. Graham/Arizona altitude 3187 m) are routinely observing in the 495, 660 and 800 GHz windows. Above 900 GHz the windows not only become fewer, but even inside the windows the absorption is still very high. Only at extremely high altitudes and under perfect weather conditions a suitable transparency for observations can be reached, e.g. 10% transmission at 1.5 THz is reached on 35 days per year at Chajnantor (Chile, fig. 1). Two sites for ground based THz astronomy appear particularly promising: The South Pole with the Antarctic Submillimeter Telescope and Remote Observatory (AST/RO) for 1.2-

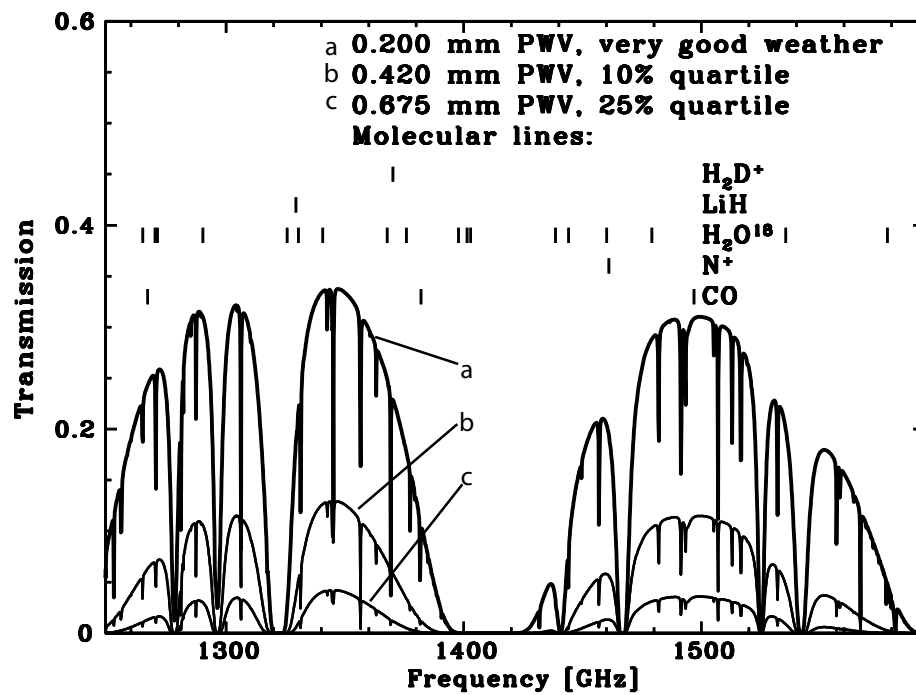


Figure 1: Atmospheric transmission at Chajnantor

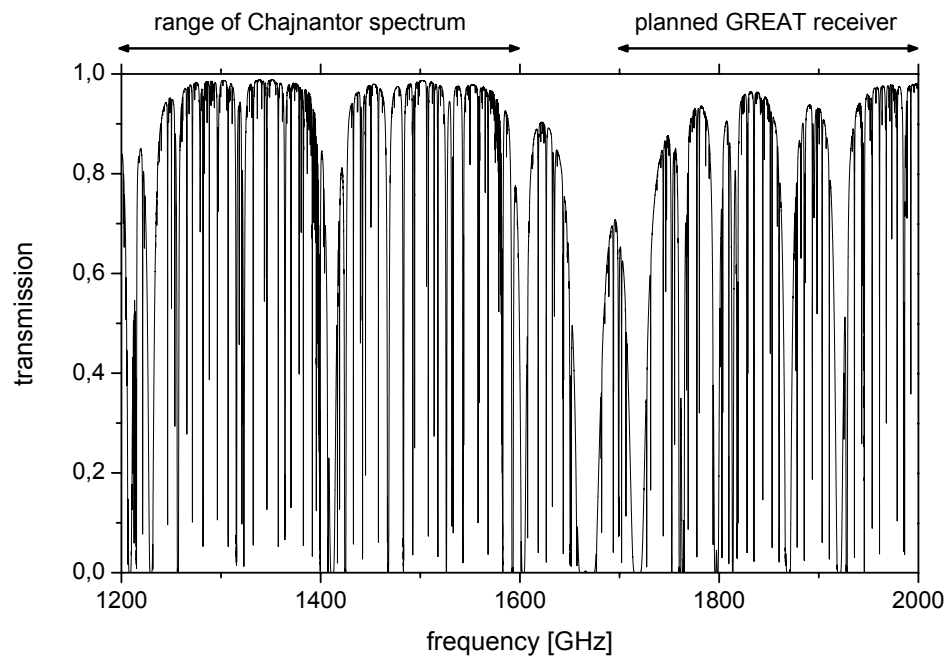


Figure 2: Atran [3] modelled atmospheric transmission in 12 km height with $7.3 \mu\text{m}$ precipitable water vapor (PWV), the planned altitude for observations with the SOFIA Airborne Telescope.

1.5 THz and the Atacama desert in northern Chile. In the frame of the work presented here, a 1.4 THz detector for the Atacama Pathfinder EXperiment (APEX) telescope in Chajnantor, Chile is being developed [4].

The next steps to overcome the Earth's atmosphere are to go to even higher altitudes, using airborne or satellite telescopes which, of course, imply significantly higher technical efforts. Here the Kuiper Airborne Observatory (KAO) has let the way to THz observations. The Stratospheric Observatory For Infrared Astronomy (SOFIA) [5] and the Herschel satellite are currently being built to open the THz region for systematic observations. In the case of the satellite observatory, the detectable frequency range and sensitivity is not limited at all by atmospheric absorption, but the technological efforts are enormous. However, the satellite needs to be equipped with reliable technology which can provide a long record of use. The big advantage of the SOFIA airplane is that it can be equipped with varying and even experimental detectors. In figure 2 the calculated atmospheric transmission at the altitude of 12 km can be seen.

Two receivers for the SOFIA telescope are developed at the I. Physikalisches Institut der Universität zu Köln / KOSMA [6]: The German Receiver for Astronomy at Terahertz Frequencies (GREAT) [7] with two channels at 1.6-1.9 THz and the 4x4 SOFIA Terahertz Array Receiver (STAR) [8] at 1.9 THz. This work focuses on the development of the corresponding detectors for both receivers. We are considering expanding this technology to a 2.7 THz receiver.

2.2 THz detectors

This work focuses on coherent detection of radiation. The output data of a coherent detector contains all information about frequency, amplitude and phase of the detected astronomical signal.

Incoherent detectors or direct detectors respond only to incoming radiated power in a known frequency band. To obtain a frequency selective response, a filter is placed in front of the detector, which determines the spectral resolution. Interference filters can provide small relative bandwidths (e.g. resolution SAFIRE: $\lambda/\Delta\lambda < 2 \cdot 10^3$ [9]). However the losses in the filter increase with higher resolutions and higher frequencies.

For coherent detection of THz frequencies commonly heterodyne mixers are used. The heterodyne mixer is used to mix the astronomical radio frequency RF signal with a locally generated coherent signal (local oscillator) to generate an intermediate frequency (IF) signal. The IF signal, for example 4-8 GHz, can be analyzed with a resolution of 0.1 MHz, corresponding to relative resolution 1 THz RF of $\lambda/\Delta\lambda = 10^7$.

Hence the heterodyne technique allows high resolution molecular spectroscopy which offers detailed conclusions about the chemical and physical properties of the astronomical source. The phase information of several detectors from different telescopes

can be used for interferometric observations. In this case the angular resolution is not limited by the aperture of the primary telescope mirror, but by the baseline between the telescopes.

At present there are three main technologies for mixer devices for THz frequencies:

1. Schottky junctions,
2. Superconductor/Normal conductor/Superconductor (SIS) junctions,
3. Superconducting Hot Electron Bolometers (HEB).

The first observations were done with Schottky mixers [10] which implement the non-linearity current-versus-voltage characteristic of a semiconductor-metal junction. Typical receiver noise temperatures are above 2000 K at 600-800 GHz. Up to 1 THz these have been replaced in most telescopes by SIS mixers with superconductor/normal conductor/superconductor junctions. With SIS mixers receiver sensitivities of nearly the quantum limit have been reached (e.g. 75 K at 490 GHz). Unfortunately the maximum detectable frequency of SIS mixers is limited by the gap frequency $\Delta E_{gap} = \hbar v_{gap}$ of the used superconductor. At frequencies above the gap frequency, the noise temperature of the SIS mixer increases and at frequencies above twice the gap frequency, the SIS junction does not function as a mixer anymore. Niobium (gap frequency ~ 700 GHz) SIS mixers have been successfully used at various telescopes up to 900 GHz. Recent developments with Nb/NbTiN SIS junctions promise mixer elements up to 1.4 THz. For 1.9 THz, which is the focus of this work, no SIS mixers are presently available.

This leaves the Hot Electron Bolometers (HEB) and the Schottky mixers. Hot Electron Bolometers need significantly less local oscillator (LO) power than Schottky mixers. LO power consumption is a major concern, as it is very difficult to generate a stable and tunable THz oscillator signal with enough power. Superconducting HEBs can be pumped sufficiently with several hundred nanowatts, while Schottky mixers need several microwatts. Recent results of HEBs showed noise temperatures of 700-1000 K at 1-2 THz ([11], [12]) which are lower than with Schottky mixers at these frequencies.

Hence HEBs have been implemented as mixers of choice into the waveguide technology developed in this work, but SIS mixers might also be integrated. The waveguide technology is used to couple the incoming high frequency signal to the HEB mixer element. New concepts have been developed to expand the established KOSMA 800 GHz waveguide concept with HEB mixers on fused quartz substrates to 1.9 THz. In this context it had been necessary to develop a reliable fabrication process for HEBs on 2 μm thick freestanding membranes, whereby the new mixer design has been optimized with 3D e/m simulations. New computer controlled DC measurement setups with automated characterization routines have been constructed for superconducting thin film development and advanced HEB device characterization. Various novel

micro-machining technologies for the fabrication of waveguide structures - smaller than 50 microns - have been explored. A Micro Assembly Stage for the mounting mixers devices of 80 microns width has been developed and integrated into space qualified production.

With the technology developed in this work Hot Electron Bolometers (HEB) have been successfully fabricated on freestanding Silicon Nitride membranes which have been tested in a heterodyne setup and used for astronomical observations at the KOSMA telescope at Gornergrat.

3 THz waveguide heterodyne mixers theory

This chapter separates into two parts. In the first part the heterodyne principle is described on which the presented detectors are based. In the second part the waveguide technology is discussed which has been used in this research to realize the receiver system. Furthermore in this chapter it is motivated why these technologies have been favored above alternative technologies.

3.1 Heterodyne detection principle

The heterodyne detection principle (also super-heterodyne or super-het) was invented in 1918 by E. H. Armstrong to enhance the frequency selectivity of the early radio systems. It has since then become commonly used in high frequency receivers up to the present day. Instead of filtering and amplifying the incoming radio frequency (RF) signal as such, it is down-converted to a significantly lower intermediate frequency (IF). This IF signal can be handled and processed with substantially less technological effort than the RF. In the IF, both phase and frequency information of the signal are preserved and can be analyzed. This technology is widely used in today's mm and sub-mm astronomical receivers.

At 2 THz RF, as it is the focus of this work, the following aspects of the heterodyne principle are important. First, no amplifiers are available for frequencies above 200 GHz. The down-converting of the RF, however, is still possible up to the far THz region. Second, the low frequency IF signal can be resolved and analyzed with far higher resolution than the RF. The third point concerns a general problem of receiver systems. The necessary receiver gain of more than 100 dB implies high risk for instabilities and feedback oscillations. The shift in frequency, however, largely prevents these oscillations.

In a heterodyne system, the RF signal is mixed with a fixed local oscillator (LO) frequency. In the classical mixer, the non-linearity of the mixer produces a product signal of the LO- and RF-frequency. A bolometer mixer, for example, has a response to the incoming power, which is proportional to the quadrature of the signal voltage. Using the addition theorems, the product of two frequencies can be solved to:

$$V_{LO} \cos(\omega_{LO}t) \cdot V_{RF} \cos(\omega_{RF}t) = \frac{V_{LO}V_{RF}}{2} (\cos[(\omega_{LO} + \omega_{RF})t] + \cos[(\omega_{LO} - \omega_{RF})t]) \quad (1)$$

The high frequency terms are filtered out and we get the intermediate or beat frequency $f_{IF} = |f_{RF} - f_{LO}|$. With other words, the RF spectrum is shifted by subtracting the constant term of the LO frequency. But not only the frequencies above the LO frequency (upper side band, USB) are shifted towards the IF band. The frequencies

below the LO frequency (lower side band, LSB) are mirrored also into the IF band. A double-side-band mixer detects both side bands while in a single-side-band mixer one of either bands is suppressed to reduce noise and misleading mirrored signals. More details about this frequency mixing in the Hot Electron Bolometer (HEB) are found in chapter 4.2.

3.2 THz waveguide-mixer concept

3.2.1 Setup

One way to realize the heterodyne principle for THz frequencies is the waveguide-mixer concept presented here. Despite the demand of considerably more technical effort than the alternative quasi-optical solutions, waveguide mixers have been the detectors of choice for heterodyne operated telescopes up to 1.2 THz (e.g. Chajnantor 1.2 THz [13], 1.5 THz in preparation) around the world. After the general description of this concept, the main advantages above the quasi-optical solution are put forward.

In the waveguide concept the RF signal of the astronomic source (ch. 2.1), overlaid with the local oscillator (LO) signal, is led through the waveguide horn (ch. 7), and is then coupled into the HEB mixer (ch. 4 + ch. 9) through the waveguide probe (ch. 8.1). In the most simple form, the waveguide consists of a closed rectangular channel with conducting inner walls. If the channel width is half the wavelength of the signal and the height is matched, signal transport with very low dispersion and losses is possible, even at extremely high frequencies. As unusual feature of the concept presented here, the waveguide probe and the HEB mixer are positioned on a free-standing membrane (ch. 5), together with the IF filter (ch. 8.1). The IF signal, produced by the HEB mixer, passes the IF filter through the substrate channel (ch. 7) to a standard SMA connector. After cryogenic low noise amplification it is analyzed in the spectrum analyzer.

3.2.2 Comparison of waveguides and quasi-optics

When the signal optics are only a few hundred times larger than the wavelength, the approximation for geometrical optics is not valid. Here the beams have to be modelled by the quasi-optical approximation. In the quasi-optics range, beams cannot be shaped into clearly limited beam shape and they cannot be focused into a single point but only into a constriction, generally called waist. Quasi-optical elements can be used to shape a gauss profile which does not show intensity side lobes. The gauss profile can therefore be fully matched to the telescope optics. In the 1-2 THz frequency range considered here, the small optical devices in and around the cryostat can be modelled with the quasi-optical approximation and a very good gaussian beam profile can be achieved. The critical point is the coupling of this beam to the electronic circuit of the mixer. In general this can be done in two ways:

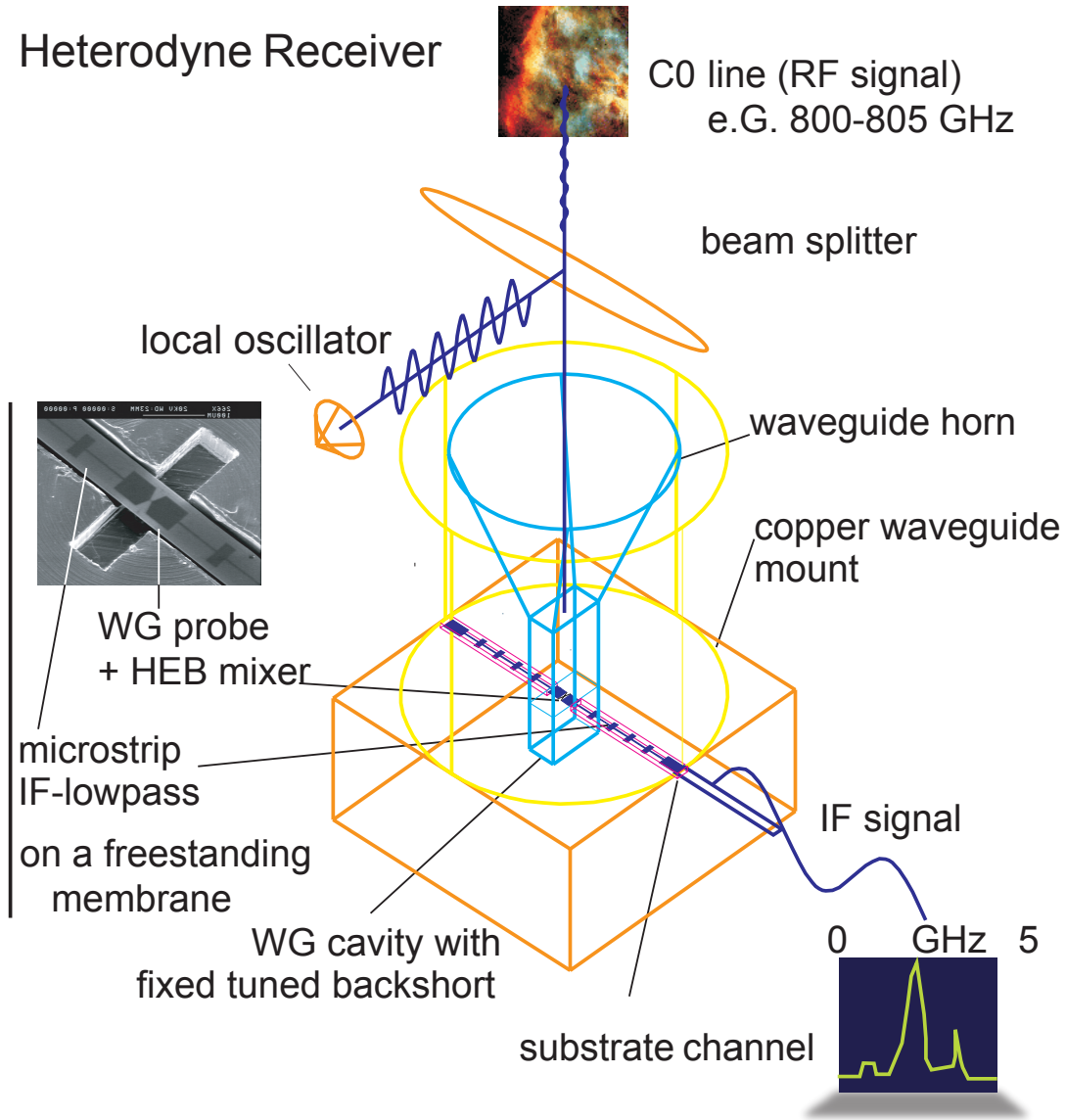


Figure 3: Heterodyne receiver(chapter numbers): The RF signal of the astronomic source (2.1) is overlaid with the local oscillator signal. Both signals are led through the waveguide horn (7) and they are coupled into the HEB mixer (4 + 9) through the waveguide probe (8.1). As an unusual feature of the concept presented here, the waveguide probe and the HEB mixer are positioned on a free-standing membrane (5), together with the IF filter (8.1). The IF signal, produced by the HEB mixer, passes the IF filter through the substrate channel (7) and is analyzed in the spectrum analyzer.

- quasi-optical lens + planar antenna,
- waveguide cavity + waveguide probe.

In the first case a waveguide horn antenna is utilized as entrance port for the signal. It shapes the beam and matches the waveguide impedance to the impedance of the free space wave. In the second case of the so called *quasi-optic mixers*, a (e.g. silicon) paraboloid with few millimeter radius is used to focus the signal onto the planar bolometer antennas. Sometimes these systems are also referred to as *open-structure mixers* to distinguish them from the closed waveguide.

Waveguide mixers at THz frequencies demand considerably more technical effort than quasi-optical mixers, but they provide a set of advantages such as:

- waveguide horns provide single mode structure and extremely high gaussivity of the beam, enabling outstanding coupling (98%) to the telescope beam. (95% for quasi-optic);
- intrinsic blocking of frequencies below the cut-off frequency, avoiding saturation;
- it is mechanically easier to make compact designs for array and satellite applications [14].

These three advantages are explained in detail, as follows.

3.2.3 Scaling of waveguide mixers

With the waveguide concept, excellent results (75K @ 490 GHz, 450K @ 780-880 GHz [15], [16]) have been achieved for up to 900 GHz with broadband, fixed tuned KOSMA-Mixers [17]. The linearity of the Maxwell equations allows scaling of this concept to 1.9 THz by down-scaling of all mixer dimensions by a factor ~ 2 .

In the technical realization the further downsizing of the waveguide micro structures is a challenge. This downsizing includes the dielectric substrate, on which waveguide probe, mixer device and IF filter are mounted. This substrate has to be sufficiently thin and narrow to prevent RF losses due to waveguide modes in the substrate channel. At 1.9 THz, a quartz substrate would be about $10 \mu\text{m}$ thick, too thin to be fabricated and handled. Therefore this work describes our efforts to develop an alternative solution for the device substrate (5). It also presents approaches for the further down-scaling of the waveguide structures (chapter 7). The limits for the micro-structuring of the filter and antenna structures are not yet reached. 3D e/m wave simulations have been done to optimize these structures and the corresponding waveguides for the membrane mixers at different RF frequencies (chapter 8.1).

4 Hot electron bolometer mixers theory

This chapter motivates the choice of Hot Electron Bolometers (HEB) as mixers for THz astronomy and reviews their basic principles and mechanisms.

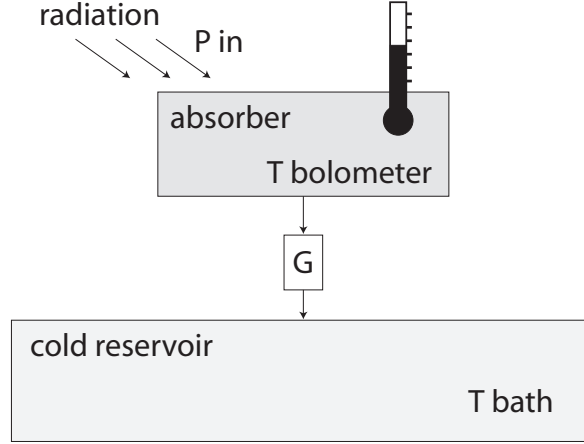


Figure 4: Schematic drawing of a bolometer

4.1 Bolometer principle

A bolometer responds to changes in the heat input from its surroundings and converts them into an electrical signal. In principle it consists of an absorber with thermal capacity C , heated up by the incoming radiation power, and a temperature dependent resistor to detect the corresponding change in temperature (see figure 4). This absorber is also coupled to a cold reservoir with defined thermal conductance G_θ . Hence we have a balance between the absorbed incoming power and the outgoing power via cooling with thermal conductance G . The balance is described in a simple model by:

$$C \frac{dT_{bolometer}}{dt} + G_\theta (T_{bolometer} - T_{bath}) = P(t) \quad (2)$$

A constant input of power results in a stationary balanced absorber temperature. Solving the equation above for a sinusoidal change of the input power with frequency f and amplitude ΔP leads to a temperature oscillation in the bolometer with the amplitude:

$$\Delta T_{bolometer} = \frac{\Delta P}{G_\theta} \frac{1}{\sqrt{1 + (2\pi f \tau_\theta)^2}} \quad (3)$$

The time constant of the thermal response $\tau_\theta = C/G_\theta$ has been introduced to describe the response time of the bolometer. As seen in the equation, the temperature oscillation fades out for higher frequencies to an average value. At the roll-off frequency $f_{roll-off} = 1/(2\pi\tau_\theta)$ the response is already reduced by $1/\sqrt{2}$. As τ_θ is of the order of pico seconds, the THz frequencies of the incoming el/m radiation are far too high for the bolometer to follow. Used as a THz detector, the bolometer only responds to the changes in the average power.

With the applied bias current I_{bias} and a gradient dR/dT in the resistance-versus-temperature curve at bias temperature, the voltage drop over the bolometer responds with:

$$S_{response} = \frac{\Delta V}{\Delta P} = \left(\frac{\Delta R}{\Delta T} \frac{I_{bias}}{G_\theta} \right) \frac{1}{\sqrt{1 + (2\pi f \tau_\theta)^2}} \quad (4)$$

4.2 Bolometer heterodyne mixers

In the heterodyne application, a local oscillator signal is added to the incoming RF signal and both are coupled into the bolometer ($\omega_x = 2\pi f_x$).

$$V(t) = V_{LO} \cos[\omega_{LO}t] + V_{RF} \cos[\omega_{RF}t] \quad (5)$$

The power $P(t)$ is dissipated at the bolometer resistance R_0 :

$$P(t) = \frac{V(t)^2}{R_0} \quad (6)$$

Inserting $V(t)$:

$$\begin{aligned} P(t) &= \frac{1}{R_0} [V_{LO} \cos(\omega_{LO}t) + V_{RF} \cos(\omega_{RF}t)]^2 \quad (7) \\ &= \frac{1}{R_0} (V_{LO}^2 \cos^2(\omega_{LO}t) + V_{RF}^2 \cos^2(\omega_{RF}t) + 2V_{LO}V_{RF} \cos(\omega_{LO}t) \cos(\omega_{RF}t)) \\ &= P_{LO} + P_{RF} + \frac{1}{R_0} (V_{LO}V_{RF} \cos[(\omega_{RF} - \omega_{LO})t] + V_{LO}V_{RF} \cos[(\omega_{RF} + \omega_{LO})t]) \end{aligned}$$

The oscillations frequencies of ω_{LO} and ω_{RF} are significantly higher than the roll-off frequency of the bolometer and only the average power of the LO/RF signal is dissipated.

$$\int \frac{V_{LO}^2 \cos^2(\omega_{LO}t)}{R_0} dt = \frac{V_{LO}^2}{2R_0} = P_{LO} \quad (8)$$

P_{RF} can be determined in the same way, but the RF signal is much weaker than the LO signal and hence its contribution to the average power dissipation can be neglected.

The oscillation frequency $\omega_{RF} + \omega_{RF}$ of term $V_{LO}V_{RF}\cos[(\omega_{RF} + \omega_{RF})t]$ is also significantly larger than the roll-off frequency and adds only a small contribution to the average power dissipation. $V_{LO}V_{RF}/R_0$ is significantly smaller than P_{LO} and is neglected in the average power dissipation.

$$\begin{aligned} P(t) &= P_{LO} + P_{RF} + \frac{1}{R_0}V_{LO}V_{RF}\cos[(\omega_{RF} + \omega_{LO})t] + \frac{1}{R_0}V_{LO}V_{RF}\cos[(\omega_{RF} - \omega_{LO})t] \\ &\approx P_{LO} + \frac{1}{R_0}V_{LO}V_{RF}\cos[(\omega_{RF} - \omega_{LO})t] \end{aligned} \quad (9)$$

Only the intermediate frequency oscillation of $f_{IF} = |f_{RF} - f_{LO}|$ can lead to an oscillating temperature, providing that the IF is in the range of the roll-off frequency. The temperature variation is detected as a voltage variation (see eqn. 4).

$$V_{IF} = S_{response} \Delta P = S_{response}(f_{IF}) 2\sqrt{P_{LO}P_{RF}} \quad (10)$$

$$= \left(\frac{\Delta R I_{bias}}{\Delta T G_\theta}\right) \frac{2\sqrt{P_{LO}P_{RF}}}{\sqrt{1 + (2\pi f_{IF} \tau_\theta)^2}} \quad (11)$$

$P_{LO/RF}$ has been introduced with $P_{LO/RF} = \delta V_{LO/RF}^2/2R$. The IF voltage oscillations correspond to the IF output power P_{IF} at the load resistance R_L of the following IF amplifier.

$$P_{IF} = \frac{V^2}{2R_L} = \left(\frac{\Delta R I_{bias}}{\Delta T G_\theta}\right)^2 \frac{2P_{LO}P_{RF}}{R_L} \frac{1}{1 + (2\pi f_{IF} \tau_\theta)^2} \quad (12)$$

The mixer conversion gain (η_{mix}) describes the power ratio of the incoming RF signal and the outgoing IF signal P_{IF} . Here only the single sideband mixer gain is presented with an assumed perfect load matching to the bolometer normal state resistance R_0 at the input and the output $R_L = R_0$ ¹.

$$\eta_{mix}^{SSB} = P_{IF}/P_{RF} = \left(\frac{\Delta R I_{bias}}{\Delta T G_\theta}\right)^2 \frac{2P_{LO}}{R_0} \frac{1}{1 + (2\pi f_{IF} \tau_\theta)^2} \quad (13)$$

In this equation the gain is proportional to the LO power. Hence it is favorable to increase the LO power. But the LO power can only be increased to a certain saturation level. If the whole bolometer is heated to normal conducting state by the LO power, the bolometer resistance becomes constant, regardless of further temperature variations.

4.3 Superconducting Hot Electron Bolometers

This section motivates the use of Hot Electron Bolometers with a superconducting micro bridge for extremely sensitive and fast heterodyne bolometers.

¹For $R_L(IF) \neq R_0$ see chapter 4.5 and 4.6

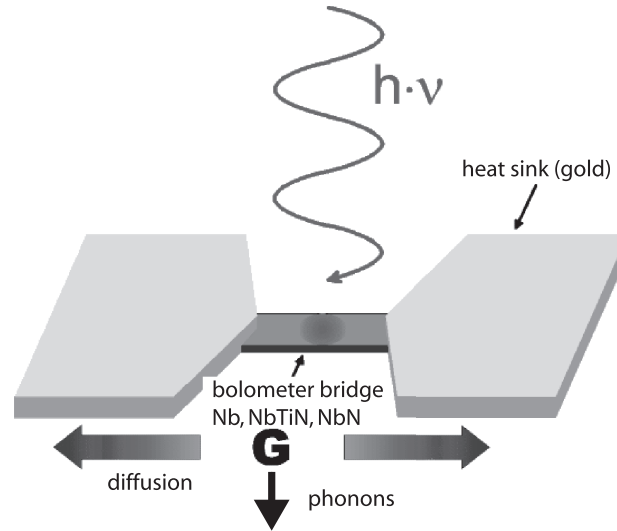


Figure 5: Simple schematic drawing of a Superconducting Hot Electron Bolometer. A short (and only a few nanometers thick) superconducting micro-bridge is confined by normal conducting heat sinks. The electron gas is heated inside the bridge by the incoming radiation and is cooled by diffusion of hot electrons into the heat sinks, or by phonon coupling to the bridge lattice and the substrate.

The thermal time constant and the corresponding roll-off frequency define the maximum difference between LO- and RF-frequency which can be detected. So only a spectrum with frequencies in this range around the LO frequency can be observed instantaneously. To expand this range, it is of high interest to reduce the thermal time constant $\tau = C/G$. One way is to reduce the thermal capacity C of the absorber, the other is to increase the thermal conductivity.

bolometer type	τ_θ	ν_{IF}
Composite bolometer	1 ms	kHz
InSb HEB	0.1 μ s	MHz
superconducting HEB	<1 ns	GHz

Table 1: Different bolometer types and the corresponding time constants.

By reducing the absorber size below 1 mm^2 and with clever cooling techniques, kHz frequencies have been reached with composite bolometers (tab. 1). In *Hot Electron Bolometers* (HEB) only the free electrons inside the conductor are heated by the radiation, while the lattice of this conductor remains on reservoir temperature. The electrons used as absorber have significantly lower thermal capacity compared to the molecules of the lattice. Hence much faster response times of MHz and even GHz frequencies can be reached. For example in superconductors, in which the resistance largely de-

depends on the electron temperature, this electron temperature can be measured via the electrical resistance.

In the general technical realization, superconducting *Hot Electron Bolometers* mixers consist of an extremely thin superconducting micro-bridge defined by normal conducting contact pads at its ends. Here the micro-bridge is only a few nanometers thick. Figure 5 shows a simple schematic drawing. The temperature profile of the hot electron gas in the bridge and the cooling mechanisms are discussed in chapter 4.4 in more detail.

In thin superconducting films, as they are used for this micro-bridge, the electron temperature can decouple from the lattice temperature. The electron gas as absorber has only vanishing, but non-zero, thermal capacity. As long as the lattice is not heated as well its thermal capacity can be neglected. The hot electron gas can be cooled very fast by diffusion of hot electrons into heat sinks, or by losing energy due to phonon coupling to the bolometer lattice. In the second case, the phonons in the bolometer lattice can escape into the substrate.

The temperature of the electron gas determines the resistance of the the micro-bridge. Superconductors are interesting as temperature dependent resistors, as they provide a step in resistance with extremely steep dR/dT slope at the critical temperature. For example a temperature change of less than 0.2 K can change the bridge properties from zero to normal state conductivity of, e.g., 100 Ω in a HEB. This would correspond to an extremely steep $\Delta R/\Delta T$ gradient of 500 Ω/K and a large bolometer response (eq. 4).

In the superconducting HEB, a small heat capacity C can be combined with a large thermal conductivity G and a large dR/dT gradient. The result is a small thermal time constant $\tau = C/G$ and a large HEB response $S_{HEB} \propto dR/dT$. Note that increasing the thermal conductivity also decreases the mixer gain at the same time (eq. 13). But the effect on the mixer gain can be compensated, with the LO power. This is possible, as the heating of the bolometer is also proportional to P_{LO}/G .

4.3.1 Hot Electron gas in thin superconducting films

The interaction time of electrons with electrons $\tau_{e \leftrightarrow e}$ and the interaction time of electrons with phonons depend on the mean free path l and the temperature T :

$$\tau_{e \leftrightarrow e} \propto lT^{-1} [18] \quad (14)$$

$$\tau_{e \leftrightarrow ph} \propto l^{-1}T^{-2} [19] \quad (15)$$

In thin superconducting films the mean free path l of the electrons decreases with film thickness. With this decrease of the mean free path, the probability for inelastic scattering of electrons with electrons increases while the probability for interactions of electrons with phonons decreases. The electron-phonon interaction time increases

faster for decreasing temperatures than the electron-electron interaction time. Hence in thin films at low temperatures the interactions among electrons through inelastic scattering become more dominant than interactions with phonons.

An incoming photon at first only transfers its energy to one single electron and heats it to higher temperature. This electron interacts mainly with other electrons because of the extremely small electron-electron scattering time constant. An increased average electron temperature is the consequence. The much slower interaction of electrons with the lattice phonons or the out-diffusion of hot electrons then cools the electron gas. This hot electron gas is giving the device the name *Hot Electron Bolometer*.

The electron gas of the superconductor serves as absorber and thermometer at the same time, because its resistance is determined by the electron temperature. Its thermal capacity C can be determined from the Sommerfeld constant γ (e.G. $\gamma_{\text{Niobium}} = 700\text{J}/\text{K}^2\text{m}^3$), the volume of the bolometer micro bridge and the electron temperature θ [19] [20]

$$C = \gamma\theta V \quad (16)$$

4.3.2 Lumped element HEB model

The first theoretical models, used to describe the physics inside the HEB, assumed the HEB as a lumped element [21]. All properties are identical for the whole bridge. The temperature dependence of the bridge resistance is given by the R/T characteristic of the superconductor. There is a steep increase near T_c , and above T_c the temperature is constant. At the operating temperature of the HEB a linear relation of ΔP , ΔT and ΔR is assumed:

$$\Delta R \propto \Delta T = \frac{\Delta P}{G_\theta} \quad (17)$$

Hence the previous calculations for bolometer heterodyne mixing (e.G. 13) can be utilized in this lumped element model. In the following, the more refined hot-spot model will be presented. Still the lumped element model will be referred to again at selected points, because certain aspects are easier to visualize with the linear properties of this model.

4.3.3 Hot-spot model

The use of one single temperature to describe the properties of the whole bolometer bridge is a crude simplification. A more refined model of the *hot-spot* has been suggested 1974 by Skocpol, Baesley and Tinkham [22] for superconducting micro-bridges and has been specified for diffusion cooled superconducting HEBs as heterodyne mixers by Wilms Floet [23],[24]. In this model the highest temperature is expected in the center of the bridge. Here the cooling is least efficient due to the large distance to the

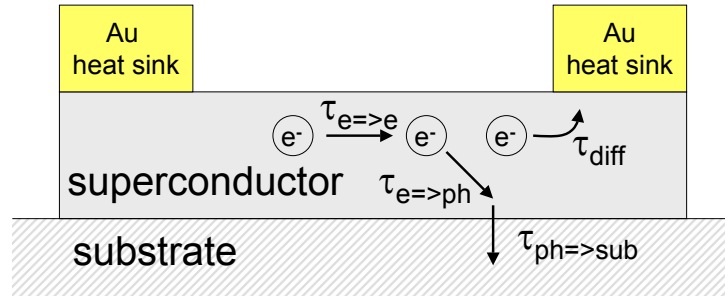


Figure 6: Cooling mechanisms of HEBs.

heat sinks. The part of the bridge, where the temperature exceeds the critical temperature T_c , becomes normal conducting. This normal conducting center of the bridge, which develops under the right bias conditions, is referred to as the hot-spot. The bolometer resistance is proportional to the length of the normal conducting hot-spot region. The DC current can only dissipate energy at the normal conducting hot-spot. The THz frequency LO power is dissipated across the whole bridge, because its photon energy is high enough to break up the cooper pairs. As a result the hot-spot size depends on DC bias power and applied RF signal and it varies with the beat frequency of the IF.

4.4 Cooling mechanisms in HEBs

4.4.1 The two main cooling mechanisms

The hot electron gas of the bridge can be cooled by two main cooling mechanisms. In the first mechanism, the heat is transferred to the lattice of the superconductor and further onto the comparably thick substrate material via phonons. This process is called *phonon cooling*.

In very short bolometer bridges, hot electrons can diffuse out into the contact pads, which serve as cooling reservoirs. This second mechanism is therefore called *diffusion cooling*. The *diffusion cooling* depends directly on the bridge length. Both mechanisms are generally present in HEBs, but the device geometry and the material properties

decide which one is dominant. It separates the bolometers in the categories of Phonon Cooled HEBs (P-HEBs) and Diffusion Cooled HEBs (D-HEBs).

The following table shows the differences in the material parameters of Niobium and some of its alloys. The large differences in the diffusion constants D lead to the distinction of devices into different categories, even if they have an otherwise comparable geometry. The third column contains the thermal healing length $\sqrt{12}\lambda$. It is an indicator from which bridge length onward phonon cooling dominates and diffusion cooling becomes negligible.

super-conductor	D [cm^2/s]	$\sqrt{12}\lambda$ [nm]	phonon cooling	diffusion cooling	citation
Nb	1.00	1000		x	[21]
NbN	0.1	70	x		[25],[26]
NbTiN	0.7		x	?	[27]
Al	10.00			x	[28]
Ta	≥ 1	≥ 1000		x	[29]

Table 2: Diffusion constants and thermal healing length $\sqrt{12}\lambda$ for different superconducting materials.

In the following the details of these two mechanisms are described. More insights into the exact calculations of thermodynamics of the HEB, are offered for example in [30], [31], [23] and [32]. Certain aspects of the HEB theory are discussed and compared to simulations in chapter 11.

4.4.2 Phonon cooled Hot Electron Bolometers

The hot electrons can create ballistic phonons in the lattice of the thin superconductors, which then can escape into the substrate. The thermal time constant is given by [33]:

$$\tau_{\theta} = \tau_{e \Rightarrow ph} + \tau_{ph \Rightarrow sub} \frac{C_e}{C_{ph}} \quad (18)$$

In this case the electron-phonon interaction time $\tau_{e \Rightarrow ph}$ and the phonon escape time $\tau_{ph \Rightarrow sub}$ have to be added to determine the thermal time constant. Note that the ratio of heat capacities of the electron gas C_e and the lattice C_{ph} play an important role. With $C_e \ll C_{ph}$ the energy escape into the substrate is enhanced.

The phonon escape time $\tau_{ph \Rightarrow sub}$ should be much smaller than the energy reabsorption time of the electrons $\tau_{ph \Rightarrow e}$ to keep the bolometer temperature low and to prevent feedback of energy back to the electrons. $\tau_{ph \Rightarrow sub}$ directly depends on the film thickness [34], hence large effort in the development of P-HEBs is spent on reduction of the film

thickness and improvement of the acoustic matching at the film substrate interface. For sufficiently thin films, $\tau_{ph \Rightarrow sub}$ becomes negligible and the time constant is only limited by the electron-phonon interaction time $\tau_{e \Rightarrow ph}$. The latter is approximately 1 ns for Niobium, and 15 ps for 5 nm thick NbN. This would result in an IF roll-off of 160 MHz for Niobium, which is far too low for astronomical research, and 10 GHz for the NbN film, respectively. Another material which has been recently used for phonon cooled HEBs is NbTiN. No data is available for the electron-phonon and phonon escape times of NbTiN. Estimations assume that both time constants are 20% higher than in NbN and that the diffusion constant D in NbTiN is approximately 7 times larger than in NbN [26]. Hence diffusion cooling might play a role in small NbTiN bolometers.

With 3.5 nm thick NbN films, IF bandwidths of 5 GHz [35] and 6 GHz [12] have been reached in the experiment, which is only half of the calculated value. NbTiN is being successfully used at KOSMA to fabricate 3-5 nm thick phonon cooled bolometer films [36]. With these films quasi-optical P-HEBs have been produced with 2.7 GHz and 3.5 GHz noise bandwidth [11]. The film for the waveguide P-HEB on a freestanding membrane, which is presented in this work, has also been produced at KOSMA.

One approach to increase the IF bandwidth is to improve the lattice matching of the superconducting film and the substrate by using buffer layers like MgO [37] or AlN [36].

4.4.3 Diffusion cooled Hot Electron Bolometers

If the normal conducting contact pads of the superconducting microbridge are close enough to the hot spot, hot electrons with high kinetic energy can diffuse out of the bridge into the pads to thermalize. Prober [21] presented the idea in 1993 to use this effect for HEB mixers. Important for the diffusion cooling capability is the ratio of the material-specific diffusion constant D and the distance of the hot electron gas to the cooling contact pads or so-called heat sinks. If the bridge length is shorter than the thermal healing length $\sqrt{12}\lambda$ the diffusion cooling becomes dominant. λ is linked to the diffusion constant and the electron-phonon interaction by $\lambda = \sqrt{D\tau_{e,ph}}$. In Niobium for example, D is approximately $1 \text{ cm}^2/\text{s}$ and $\sqrt{12}\lambda$ is about 1000 nm. The constant factor $\sqrt{12}$ results from the device geometry [38],[39].

The thermal time constant depends in first order estimation on the length of the microbridge L and the diffusion constant D [40]:

$$\tau_{\theta} = \frac{L^2}{\pi^2 D} \quad (19)$$

The value of the diffusion constant D again depends largely on the temperature of the superconductor.

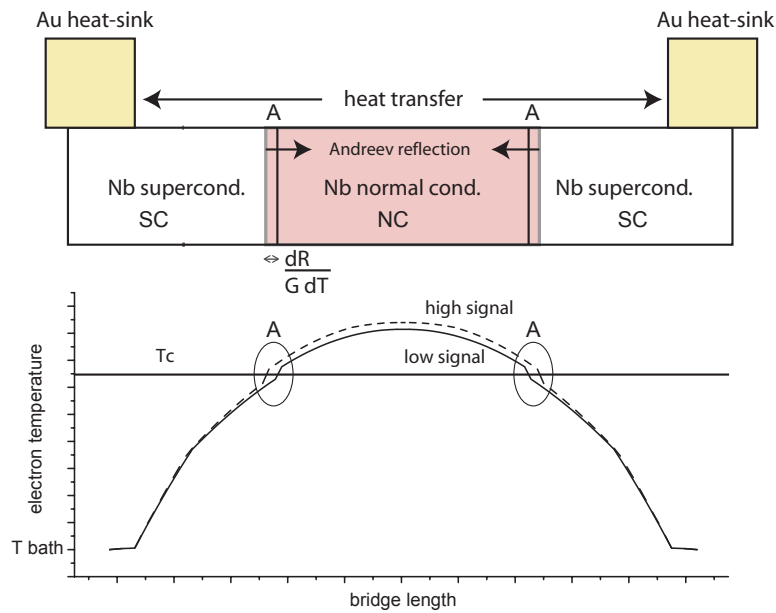


Figure 7: Simulated temperature profile of the electrons in the bolometer bridge. In the sections where the temperature exceeds the critical temperature T_c , the bridge becomes normal conducting. At the normal conductor/superconductor interface the heat is reflected due to Andreev reflection. More details about the simulations in ch. 11.

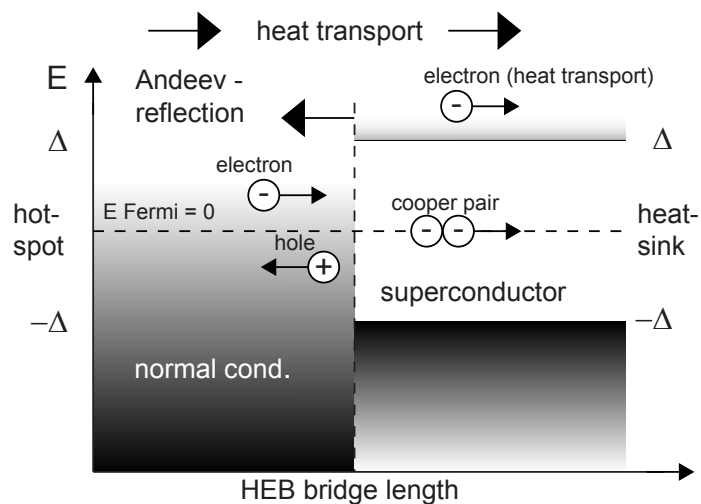


Figure 8: Heat transport through normal conducting electrons in the superconductor and Andreev reflection at the normal conductor/superconductor interface.

Hot-spot model with diffusion cooling The heat transfer from the hot-spot to the heat sinks is visualized in figure 7 with a simulated temperature profile. In the following, three different regions of the bridge are discussed:

- **NC** normal conducting region (high thermal conductivity)
- **SC** superconducting region (low thermal conductivity)
- **A** superconductor and normal conductor interface (Andreev reflection)

NC region

The thermal transport in metals is determined by the mobility of the free electrons in the electron gas. Inside the hot-spot the thermal conductivity and diffusion constant D_{NC} are high as it would be expected for normal conducting metal. The diffusion constant is determined by the ratio of the thermal conductivity K and the electron specific heat c_e . In normal conducting metals, both are decreasing linearly with temperature, so that D_{NC} remains temperature independent.

SC region

Inside the superconductor electrons pair up to cooper pairs and are not available for the heat transport anymore. The cooper pairs on the other hand have a significantly higher thermal capacity. The ratio of normal conducting electrons and cooper pairs drops with temperature, hence in the superconductor $c_e \sim \frac{1}{T}$ increases for small temperatures while K decreases with T^2 [20]. In the case of a Nb bolometer, the diffusion constant in the normal conductor is about 3-5 times higher than in the superconductor at 4.2 K [23]. Around T_c , where only a small amount of electrons has paired to cooper pairs, the thermal conductivity of the normal conductor and the superconductor converge. Hence the thermal conductivity is higher in the center than near the heat sinks where the temperature is lower. As a result the temperature profile is not parabolic but is broader in the center and steeper near the heat sinks (fig. 7). The total thermal conductivity depends on the temperature profile. In a first order approximation, the thermal conductivity rises with the hot-spot temperature.

A region

At the interface between the normal conductor and the superconductor the thermal transport is reduced due to Andreev reflection (fig. 8) [41]. An electron in the normal conductor can only enter the superconductor under three conditions:

- the energy is above the Fermi level,
- the energy is in the range of the energy gap of the SC ($E_{Fermi} \pm \Delta E_{gap}$),
- and there is an electron available at the NC interface with which it can recombine to a cooper pair.

When the Cooper pair is generated, a hole is reflected into the normal conductor, taking along the major part of the energy. Through the hole generation, energy, charge and transverse moment are preserved. What we see, especially at temperatures well below the critical temperature, is a transport of electrons in absence of thermal transport. This leads to the small step in the temperature profile at the position of the interface.

This section about the diffusion cooling is closed with a very rough estimation of the thermal time constant in dependence of the device dimensions. The diffusion constant D of Nb is approximately $1 \text{ cm}^2/\text{s}$ (tab. 2). To reach an IF gain bandwidth of 6 GHz with Niobium for example, a bridge length of 140 nm would be needed. The length of the bridge also scales the normal conducting resistance R_N . But R_N has to be large enough because the HEB serves as load for the RF antenna. To increase the resistance for short HEBs, the bolometer bridge has to become narrow and thin. In the above mentioned example, a 90 nm wide bolometer bridge, made of a 12 nm thick Nb film, would show an R_N of about 20 Ohm. These are extremely small dimensions, but HEBs with these specifications can be produced at KOSMA ([30] + ch. 9). The 20 Ohm impedance can be matched to the waveguide antennas developed with the aid computer simulations in chapter 8.1.

4.5 Self-heating and electro-thermal feedback

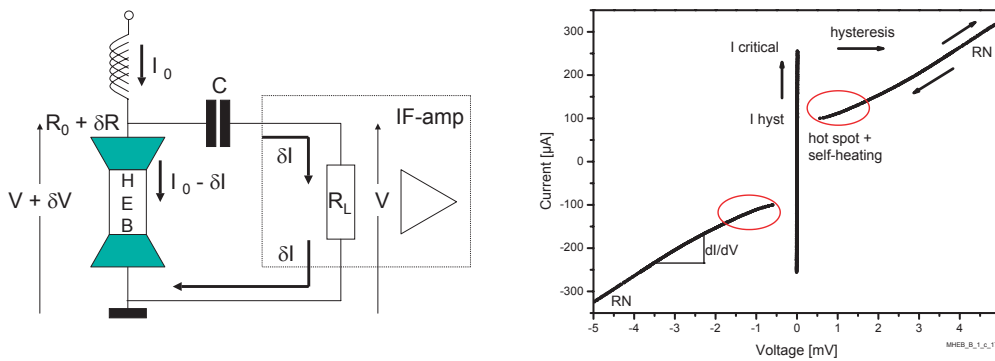


Figure 9: Left) HEB-circuit. Right) Current vs. Voltage curve of a HEB. The *self-heating* causes the nonlinearity.

The HEB is operated as part of an electronic circuit. In the following the interdependency of the electronic circuit and the HEB response is discussed. In figure 9 (left) the schematic application of a HEB with bias supply and IF amplifier can be found. The DC bias current I_0 is coupled to the HEB via an inductance. The IF signal is coupled capacitively to the load R_L of the first IF amplifier. The heat dissipated by

the bias current is causing the so-called *self-heating*. It leads to the non-linearity in the current-vs-voltage (I/V) curves of HEBs (fig. 9, right). At low biasing voltages the resistance increases due to the increasing temperature of the device. Hence the current does not increase proportional with a rise in voltage. At high bias voltages the whole bolometer is heated above T_c and the resistance is constant. Then the current is of course proportional to the voltage.

Vice versa, the changing resistance of the device influences the bias conditions and the *self-heating*. This interdependency of HEB temperature and electrical power dissipation is called *electro/thermal (el/th.) feedback*. It is related to the interplay of electrical bias circuit and thermal response of the device. The *electro/thermal feedback* influences the performance of the mixer and therefore a proper choice of bias and IF coupling to the device is important. In the following the considerations of Ekström [42] about the *el/th feedback* in the lumped element model are used for the calculations. In the end of this section the influence of the hot-spot size, which has been neglected in this approach, are discussed.

At first the DC characteristics of the *el/th feedback* are discussed. If the thermal time constant of the bolometer is larger than the time constant of the DC supply, the biasing has an influence on the mixer time constant. This effect can be observed with slow transition edge bolometers used for direct detection. The time constants of the HEBs presented in this work are smaller than the time constant of the DC supply by several magnitudes. Hence the time constant of these HEBs is only influenced by the IF coupling to the IF amplifier and not by the DC biasing. The simple considerations about the DC biasing are utilized here to explain the more complex influence of the IF circuit.

In the case of constant current DC bias or *current-bias*, the dissipated power is proportional to the HEB resistance R_0 : $P_{DC} = I_0^2 R_0$. Hence a small increase in the resistance due to a small change in input power ΔP_{input} , causes an increase of the dissipated DC power ΔP_{DC} . With the dissipated power the bolometer temperature T rises. Hence the increase in DC power results in further increase of the resistance supporting the initial increase of R_0 in a *positive* feedback loop. As a result the change in temperature is larger than without *el/th feedback*:

$$\Delta T = \frac{\Delta P_{input}}{G} + \frac{\Delta P_{DC}^{cl}(\Delta P_{input})}{G} = \frac{\Delta P_{input}}{G} + I_0^2 \frac{\Delta R}{G} \quad (20)$$

The second term, which corresponds to the *self-heating*, is deduced in Appendix A. The additional heating opposes the cooling of the HEB. The net effect is sometimes expressed as reduction of the thermal conductivity by additionally dissipated power. From Ekström [43] we get:

$$G_{eff}^{cl} = G_\theta - I_0^2 \frac{dR}{dT} \quad (21)$$

The reduction of the effective thermal conduction G_{eff}^{cl} enlarges the thermal time constant $\tau = C/G_{eff}$ and consequently slows down the bolometer².

If, on the other hand, the bolometer would be biased with a constant voltage source, then an increase of resistance would cause a decrease of the current: $P = V^2/R_0$. Hence a decrease of the dissipated power is the result, which again decreases the temperature and device resistance, respectively. In summary the reduction of the DC power dissipation, caused by the change in the input power ΔP_{input} , partly compensates this input. This effect has been calculated in the Appendix A:

$$\Delta T = \frac{\Delta P_{input}}{G} - \frac{V^2}{R_0^2} \frac{\Delta R}{G} \quad (22)$$

Hence we have a *negative* feedback loop and a more stable bolometer temperature. The net effect can be considered in an increased thermal conductivity:

$$G_{eff}^{cV} = G_\theta + \frac{V^2}{R_0^2} \frac{dR}{dT} \quad (23)$$

As a result the mixer time constant $\tau = C/G_{eff}$ is reduced and the bolometer response becomes faster¹.

In the heterodyne setup, the bolometer with resistance R_0 is capacitively coupled to the IF amplifier load R_L . Hence the IF voltage oscillations at the bolometer cause an IF current which can flow through the capacitor. Note that this effect does not change the DC bias conditions, because the DC bias is decoupled through the inductance. At R_L and R_0 , respectively, we have the voltages:

$$R_L : \quad V + dV = (I - dI)(R_0 + dR) \quad (24)$$

$$R_0 : \quad dV = dIR_L \quad (25)$$

The change in the power dissipation due to the IF current through the load resistance can be calculated (App. A):

$$dP = I^2 dR \frac{R_L - R_0}{R_L + R_0} \quad (26)$$

This can be expressed by introducing the effective cooling G_{eff}^{IF} :

$$G_{eff}^{IF} = G_\theta - I^2 \frac{R_L - R_0}{R_L + R_0} \frac{dR}{dT} \quad (27)$$

In the case of $R_L > R_0$ we have positive feedback with reduced effective cooling, similar to the constant bias current case (eq. 21). Hence the bolometer is slowed down for the IF oscillations and the roll-off frequency is reduced. If R_L is smaller than R_0

²The DC biasing only influences bolometer time constant if the time constant of the DC bias is smaller than G_θ

the algebraic sign of the equation above changes and less heat is dissipated. With this *negative* feedback the effective cooling is enhanced and therefore the IF bandwidth increases.

With G_{eff} a new time constant τ_{eff} can be calculated:

$$\tau_{eff} = \frac{C}{G_{eff}} = \frac{\tau_{\theta}}{1 - \frac{I_{bias}^2}{G_{\theta}} \frac{dR}{dT} \frac{R_L - R_0}{R_L + R_0}} \quad (28)$$

$\tau_{\theta} = C/G_{\theta}$ is the time constant without *el/th-feedback*. If R_0 and R_L are equal, the time constant is not altered.

Until this point we have assumed a linear response of the HEB to changes in the power input (lumped element model, eq. 17). In the hot-spot model the effective cooling additionally depends on the hot-spot size. First, the thermal conductivity of Nb depends largely on the temperature. Above T_c the diffusion constant is about 3-5 times higher than at the LHe bath temperature. Second, the distance between hot-spot and heat-sinks shrinks when the hot-spot becomes larger. Hence if the hot-spot size increases with temperature, the thermal conductivity of the bridge increases, too. The enhanced cooling leads to negative feedback which opposes the increase of the hot-spot. As a result large temperature swings are suppressed. If only small signal variations are considered at a certain bias point, the previous linear calculations can still be used as first order approximation.

The DC bias and IF matching properties can be set independently from each other. To achieve stable bias conditions, a constant voltage bias is favorable. In this case even small fluctuations in the LO power do not change the bolometer temperature, as long as these are slow enough. An IF load resistance smaller than the HEB resistance would increase the IF bandwidth, which would be of high interest. Unfortunately it is very difficult to build low noise GHz IF amplifiers with small input impedances. Diffusion cooled HEBs impedances are mostly below 20 Ω , while phonon cooled HEBs can be designed with impedances above 100 Ω . IF amplifiers are found with input impedances of 30-100 Ω . It might be possible to tune the input resistance of the IF load with a tuning circuit. The silicon support frames, which have been developed in the context of this work, would allow the design of very interesting superconducting micro-strip IF tuning circuits.

Note that the *el/th-feedback* is not an effect of IF reflection due to mismatch. The IF mismatch has to be considered additionally. In the current discussion it is assumed that the IF impedance of the HEBs is determined by the differential resistance at the bias point. In this case the IF impedance of the HEB is different from its resistance R_0 at the bias point.

4.6 Conversion gain of HEBs

Section 4.2 has introduced the mixer gain. The *electro/thermal feedback*, described above, influences the mixer gain.

The thermal efficiency C is introduced to describe the change of bolometer resistance in relation to dissipated power.

$$C = \frac{\partial R}{\partial P} = \frac{1}{G} \frac{\partial R}{\partial T} \quad (29)$$

With C and the relation of $dT = dP/G$, equation 3 can be simplified and used to determine the resistance response of the HEB:

$$\delta R_{bolometer} = C \delta P \frac{1}{\sqrt{1 + (2\pi f \tau_\theta)^2}} \quad (30)$$

In the following, a distinction between C_{RF} and C_{DC} is made to separate the heating effects of the RF and the DC power fluctuations, because in the superconducting regions of the HEB only the RF signal and not the DC bias dissipates power.

$$C_{RF} = \frac{\delta R}{\delta P_{RF}} = \frac{RN}{L_{bridge}} \frac{\delta L_{hot-spot}}{\delta P_{RF}} \quad (31)$$

$$C_{DC} = \frac{\delta R}{\delta P_{DC}} = \frac{RN}{L_{bridge}} \frac{\delta L_{hot-spot}}{\delta P_{DC}} \quad (32)$$

According to [43] C_{DC} can be determined from the pumped I/V curve with the differential resistance $R_D = (dV/dI)_{DC}$ at the bias point (deduced in App. B, eq. 109).

$$C_{DC} = \frac{dR}{dP_{DC}} = \frac{d(V/I)}{d(IV)} = \frac{1}{I^2} \frac{R_D - R_0}{R_D + R_0} \quad (33)$$

The fluctuations of the DC and the RF power add up for the HEB resistance response:

$$\delta R = (C_{RF} \delta P_{RF} + C_{DC} \delta P_{DC}) \frac{1}{\sqrt{1 + (2\pi f \tau_\theta)^2}} \quad (34)$$

The applied bias current I_0 leads to a voltage drop at the HEB of $V_0 = I_0 * R_0$. Changes in the HEB resistance $R_0 + \delta R$ are causing an alternating voltage δV and current δI , respectively, which can pass the coupling capacitor C and runs through the IF load resistance R_L (fig. 10). The oscillating IF voltage has to have the same value at both the HEB and the load due to the capacitive coupling. Hence δI and the corresponding *el/th-feedback* are related to R_L and R_0 by:

$$V + \delta V = (R_0 + \delta R)(I_0 - \delta I) \quad (35)$$

$$\delta V = \delta I * \delta R \quad (36)$$

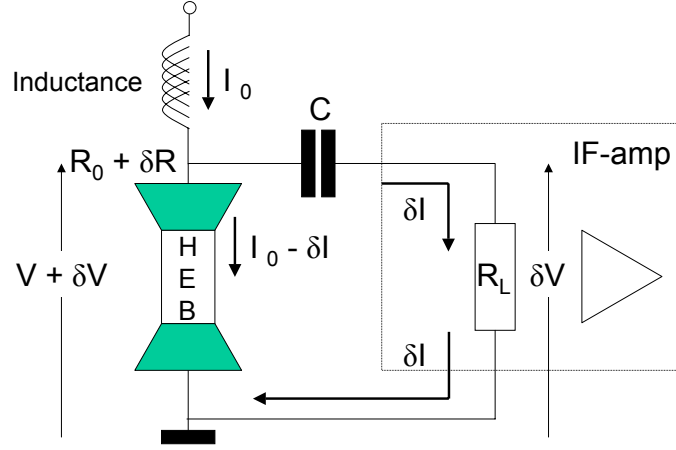


Figure 10: HEB-circuit

Solving the equations in the Appendix B, the mixer gain can be calculated.

$$\eta_{mix}^{el/th} = \frac{P_{IF}}{P_{RFsig}} = \frac{2I_0^2 C_{RF}^2 P_{LO} R_L}{(R_L + R_0)^2 (1 - I_0^2 C_{DC} \frac{R_L - R_0}{R_L + R_0})^2} \frac{1}{(1 + (2\pi f \tau_{mix})^2)} \quad (37)$$

In this equation the electro-thermal feedback is considered in the gain magnitude as well as in τ_{mix} (eq. 28), which defines the roll-off frequency.

4.7 Noise

The main noise contributions for HEB mixers are the Johnson noise and the fluctuation noise. In the following both are discussed in terms of origin and their effect on the mixer performance. With output noise temperature T_{noise}^{out} and mixer gain η_{mix} , the equivalent input noise temperature is given by:

$$T_{noise}^{in} = \frac{T_{noise}^{out}}{\eta_{mix}} \quad (38)$$

4.7.1 Johnson noise

The resistance R at temperature T produces thermal noise, the so called Johnson noise. It is caused by the statistic movements of the electrons due to thermal excitation. In the

case of the HEB we have to consider the electron temperature T_e . The thermal noise voltage signal of a resistor, here the HEB with R_0 , can be written as:

$$\langle v^2 \rangle = 4\kappa_B B T_e R_0 \quad (39)$$

The Johnson noise results in equivalent noise power or noise temperature at the output of the HEB:

$$T_{Jn}^{out} = \frac{4R_L R_0 T_e}{(R_L + R_0)^2 (1 - I_0^2 C_{DC} \frac{R_L - R_0}{R_L + R_0})^2} \quad (40)$$

It is independent of the IF frequency at the output. The equivalent input noise is defined as output noise divided by mixer gain (η_{mix} , eq. 37 and eq. 38)

$$T_{Jn}^{in} = \frac{R_0 T_e}{I_0^2 C_{RF}^2 P_{LO}} (1 + \omega^2 \tau_{mix}^2) \quad (41)$$

The equivalent input noise due to Johnson noise increases when the mixer gain decreases for higher IF.

4.7.2 Fluctuation noise

The largest noise contribution at frequencies below the roll-off frequency comes from the thermal fluctuation noise. Fluctuations in the electron temperature lead to resistance variations and therefore to output noise power. Only the fluctuations with frequency smaller or equal to the bolometer response frequency, can cause resistance variations and a corresponding noise signal. The thermal fluctuation noise can be written as:

$$T_{Tfl}^{in} = \frac{2T_e^2 \tau_\theta}{c_e V C_{RF}^2 P_{LO}} \left(\frac{\partial R}{\partial T} \right)^2 \left(\frac{1 + \omega^2 \tau_{mix}^2}{1 + \omega^2 \tau_\theta^2} \right) \quad (42)$$

The electron heat capacity c_e and the volume V of the bolometer have to be considered here. As the mixer time constant τ_{mix} is typically close to the electron temperature relaxation time constant τ_θ , the equivalent input fluctuation noise appears IF independent. Hence the mixer can be operated for IF above $f_{roll-off}$, because the main noise contribution does not increase. In the following section the bandwidth limitations due to the other noise contributions are discussed.

4.8 Bandwidth

As mentioned before, we have two bandwidth figures for HEBs: the gain bandwidth which defines the point, where the mixer gain is reduced in half (-3dB, ch. 4.2), and the noise bandwidth, where the noise temperature has doubled compared to low IF values. It is generally larger than the gain bandwidth [44]. For the heterodyne system,

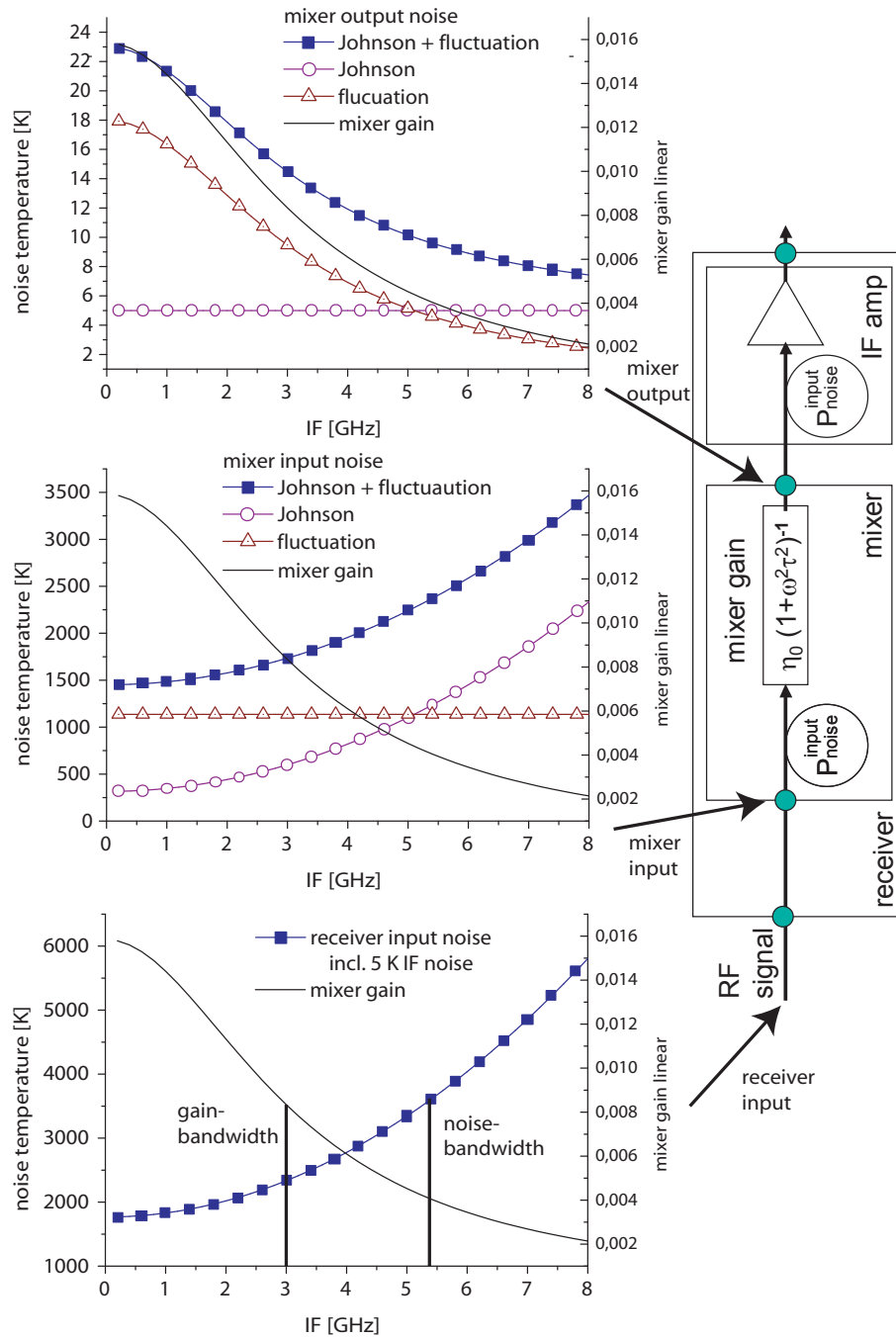


Figure 11: Schematic IF dependence of the different noise contributions and the mixer gain. (calculated curves)

the noise contribution of the IF amplifier T_{IF} has to be taken into account, too. The IF dependence of fluctuation and Johnson noise at the input and output are:

$$T_{mixer}^{in} * \text{mixer gain} = T_{mixer}^{out} \quad (43)$$

$$T_{Tfl}^{in} * \frac{\eta|_{\omega=0}}{1+\omega^2\tau_{mix}^2} = T_{Tfl}^{out}|_{\omega=0} \frac{1}{1+\omega^2\tau_{mix}^2} \quad (44)$$

$$T_{Jn}^{in}|_{\omega=0}(1+\omega^2\tau_{mix}^2) * \frac{\eta|_{\omega=0}}{1+\omega^2\tau_{mix}^2} = T_{Jn}^{out} = \text{constant} \quad (45)$$

The frequency dependent noise contributions have been separated into a frequency independent factor for $\omega = 0$, and a frequency dependent factor. In figure 11 both the input and the output noise contributions have been plotted against the IF with arbitrary test values of a virtual mixer. While the Johnson output noise is small but constant, the fluctuation noise is large for small IF and decreases in analogy to the mixer gain for high IF. Adding both noise contributions, the output noise first decreases strongly with the IF and then asymptotically approaches the Johnson noise value.

This summed output signal is amplified, together with the IF input noise, in the following IF amplifier (schematic drawing in fig. 11). The equivalent input noise temperature of the receiver system T_{rec}^{in} with mixer and IF amplifier is interesting, because it defines the system sensitivity in relation to the input signal. The total equivalent input noise temperature of this system can be calculated with (see also eq. 69):

$$T_{mixer}^{in} + T_{IF}^{in} / \text{mixer gain} = T_{rec}^{in}$$

$$T_{Tfl}^{in} + T_{Jn}^{in}|_{\omega=0}(1+\omega^2\tau_{mix}^2) + \frac{T_{IF}^{in}}{\eta|_{\omega=0}}(1+\omega^2\tau_{mix}^2) = T_{rec}^{in}$$

The receiver input noise temperature T_{rec}^{in} is shown in figure 11 at bottom. Note that the -3dB gain value is reached at $f_{gain} = 3$ GHz, while a noise temperature of 3600 K ($2*1800$ K) is reached at $f_{noise} = 5.4$ GHz. An approximation of the noise bandwidth can also be calculated directly with:

$$f_{noise} \approx f_{gain} \sqrt{\frac{T_{Tfl}^{out} + T_{Jn}^{out} + T_{IF}}{T_{Jn}^{out} + T_{IF}}} \quad (46)$$

Hence this mixer could be operated up to 5.4 GHz when a 50% reduced sensitivity is acceptable.

5 Development of Hot Electron Bolometer mixers on freestanding membranes strips

This chapter and the subsequent one describe the development of a novel technology to produce membranes for HEB mixers (chapter 4) which extend the standard KOSMA waveguide mixer technology towards 2 THz. Before the fabrication process is described in detail, a discussion about cooling problems is inserted which might result from the change in technology.

5.1 Fabrication concepts A and B - an overview

The astronomical RF signal is coupled from the waveguide to the device via the waveguide antenna probe. It is necessary for the very high frequencies considered here, that the substrate with antenna probe, HEB detector and IF filter are very thin and narrow enough ($80 \times 35 \mu\text{m}$ at 800 GHz) to prevent RF losses through the substrate channel (ch. 8.1). For 800 GHz mixers the standard procedure is to grind a quartz wafer down to $35 \mu\text{m}$, which is almost the limit in quartz thickness that can be reliably fabricated and handled. For 2 THz the mixer substrate needs to be even much thinner than this. To realize such considerably thinner substrate the general idea is to fabricate the mixer device on a thin ($\sim 2 \mu\text{m}$) membrane layer. The membrane layer is deposited or grown on a bulk wafer. The device fabrication is done subsequently. The membrane is then structured into the thin strips which are used as the substrates for the devices. Here the process can be continued in two different general directions:

Concept A: Producing the membranes together with the support frames:

By backside etching, the support wafer is taken away, leaving only the membrane strips and their frames of bulk material for support [45] (this chapter).

Concept B: Separate fabrication of membranes and support frames:

The support wafer becomes fully removed and the membrane strips are mounted on frames which are separately fabricated [46] (chapter 6).

These frame/membrane units can be glued into a copper mixer mount, similar to the standard fused quartz devices. Figure 12 shows the frame/membrane unit and its principle assembly into the mixer mount. After fixing the frame, the membrane spans freestanding in the substrate channel. The waveguide probes are centered in the RF waveguide. Finally the unit is electrically contacted with wire bonds.

Both concepts (A+B) have been pursued before for other device technologies [47], [46], [45]. The main task of this work was to find a membrane technology which would be compatible to the fabrication and operating of HEBs. Right now other groups are also working on the development of similar technologies with HEBs, but to our

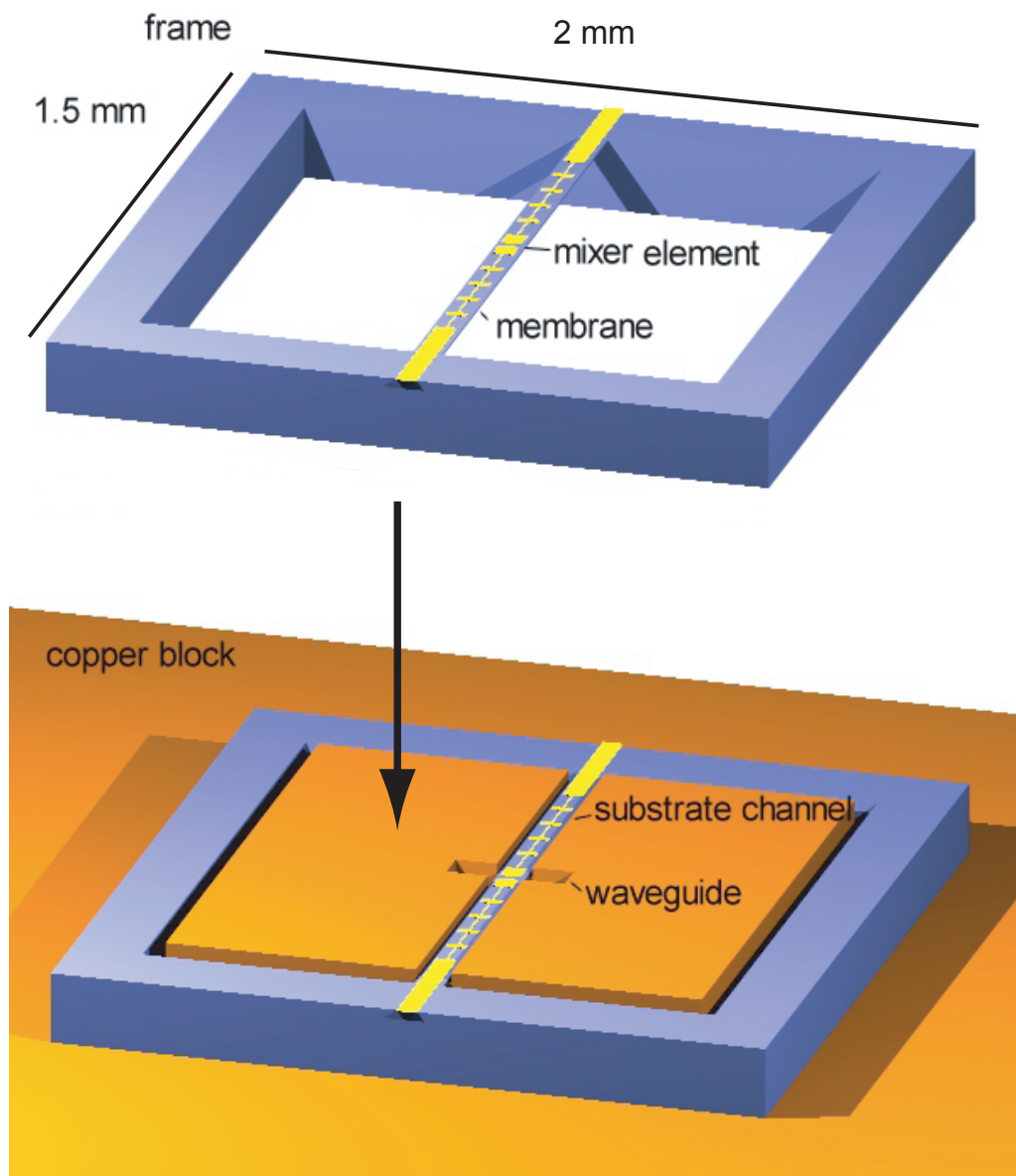


Figure 12: Mounting concept of a frame/membrane unit with device and micro-strip filter

knowledge no finished mixers or heterodyne measurements have as yet been presented in this field [48].

Materials tested were GaAs membranes on GaAs wafers with an AlGaAs etch-stop, and Low Stress Silicon-Nitride on Silicon wafers. With both material combinations, frames with membrane strips have successfully been produced. Another material tested was Silicon On Isolator (SOI), which can be structured for use as crystalline silicon membranes, but it did not show satisfying results in our experiments. This was more likely a problem of the wrong base material than of the general concept, as it is very difficult to acquire the matching SOI material in small amounts.

In principle the developed technology could also be used for superconductor/normal conductor/superconductor (SIS) devices, but there are no SIS mixers for 1.9 THz available up to now.

5.2 Thermal conductivity in freestanding membrane micro structures

5.2.1 Introduction

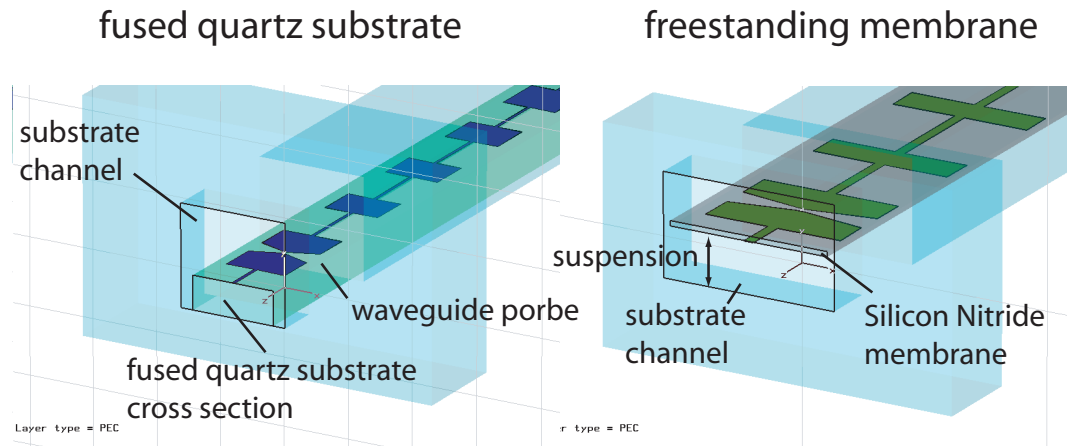


Figure 13: Cross section of dielectric filled substrate channel (old design) and suspended membrane substrate

The new membrane technology described here, allows the production of micro-structures with dimensions much smaller than with quartz. Therefore not only the RF properties, but also the mechanical properties of the membranes in terms of thermal transport have to be considered, because the mixer devices have to be cooled to 4.2 K. This section discusses the changes in thermal transport from the HEB devices to the mixer block, when using $\sim 2 \mu\text{m}$ membranes instead of solid $30 \mu\text{m}$ crystalline quartz substrates (fig. 13). It focuses on Silicon Nitride membranes, as they were chosen for the final device production. Otherwise the considerations about the heat transport properties are valid for both concepts A+B.

In the classical concept, a quartz bar is glued into the substrate channel and therefore has direct contact with the mixer block in about 200 microns distance of the HEB. The membranes of the concept presented here are freestanding inside the support frame. Hence only at the outer ends of the membrane strip, a thermal contact is provided through the frame to the mixer block. The distance of the frame to the HEB is about 0.7 mm. In addition, the silicon nitride membrane is about 10 times thinner than the quartz substrate. In a classical picture the thermal conductivity of a beam is proportional to its cross section. At very low temperatures in thin membranes, as it is the case in this concept, phonon scattering at the beam surfaces can influence the thermal

conductivity. For reasonable estimation of the heat transfer we therefore have to take low temperature effects in low dimensional systems into account.

5.2.2 Heat transfer process

The important parameter, linked to thermal conductivity G of a beam is the phonon mean free path

$$l_{eff} = 3\kappa/cv_s \quad (47)$$

where κ is the specific thermal conductivity, c the specific heat per volume and v_s the average sound speed. In general at room temperature the phonon mean free path is very small and in the range of several lattice spacings, hence the influence of scattering can be neglected. At very low temperatures l_{eff} can reach several microns and therefore exceed the membrane dimensions. Scattering and reflection of phonons at the membrane surface can therefore become the dominant factor for thermal transport.

For further analysis we have to divide the membrane materials into crystalline semiconductors like Silicon and GaAs, and amorphous insulators as low stress silicon nitride. In crystalline materials at room temperature, l_{eff} is primarily limited by Umklapp processes. A *normal process* is a phonon collision in which the total initial energy and the final crystal momentum are strictly equal. In an *Umklapp process* they differ by a non-zero reciprocal lattice vector K_0 , which is reducing the thermal transport [49]. Below 20 K the Umklapp processes decrease dramatically making it negligible for considerations at 4 K. In amorphous materials, the mean free path is mainly limited by scattering from disorder. For silicon nitride at room temperature, l_{eff} is in the order of one lattice spacing.

In crystalline and amorphous materials the dominant phonon wavelength $\lambda_d \propto 1/T$ increases with the decrease of temperature. Therefore, scattering becomes less effective at very low temperatures, and l_{eff} and the thermal conductivity increases. At sufficiently low temperatures, l_{eff} can exceed sample dimensions, so phonon surface scattering is important.

5.2.3 Surface scattering of phonons in thin membranes

The thermal conductivity through thin dielectric membranes in the surface scattering limit can be written as:

$$G = 4\sigma AT^3\xi \quad (48)$$

The factor ξ has been introduced to describe the effect of surface scattering of phonons on the thermal conductivity. A is the cross section area of the membrane and

$$\sigma = \sum_i (\pi^5 k_B^4 / 15h^3 v_i^2) = 15.7 [mW/cm^2 K^4] \quad (49)$$

with sound speeds of the two transverse

$$v_t = 6.2 \cdot 10^5 \text{ [cm/s]} \quad (50)$$

and one longitudinal

$$v_l = 10.3 \cdot 10^5 \text{ [cm/s]} \quad (51)$$

acoustic modes in silicon nitride.

If the phonons are scattered diffuse at the surface, a certain percentage is reflected back in the opposite direction. It effectively reduces the heat flow, resulting in $\xi < 1$. The limit of totally diffuse scattering is called the Casimir limit. With specular scattering the phonons are reflected in the same reflecting angle as the incident angle. Hence the phonons are not reflected in the opposite direction. The heat flow is therefore not reduced. The case of $\xi = 1$ is called specular limit. ξ can be determined by plotting G over T . Holmes et al. (ref. [50]) examined 1μ thick low stress silicon, very similar to material used for the heterodyne measurements, between 0.06 and 6 K. They tested the influence of the different scattering mechanisms by changing the membrane surface with Ag particles to induce diffuse scattering and by changing the membrane geometries. In the range of 4 to 6 K the samples showed comparable values of κ to those of bulk samples. This led the authors to the conclusion that l_{eff} was in the range of $1 \mu\text{m}$ and bulk scattering was dominant. For very low temperatures the surface scattering became more important and l_{eff} rose to about 10-100 μm . Below 0.2 K the samples with untreated and smooth surface even reached the specular limit. To investigate the influence of different surface scattering mechanisms, the authors changed the surface properties of their samples. The thermal conductivity of the samples with treated surface was reduced by a factor of 5. If the sample would have been in the Casimir limit, an even stronger reduction would be expected. The investigated samples are therefore between the Casimir and the specular limit. As an intermediate interpretation we can keep in mind, that surface treatments can reduce the thermal conductivity in thin structures at low temperatures. Hence the process for the membrane device fabrication might cause a reduction, too.

In the case of long and narrow membrane strips we have to consider scattering at the side of the membrane, too. If l_{eff} is larger than the membrane width, e.g. $40 \mu\text{m}$ at 2 THz, the thermal conductivity can be reduced by diffuse scattering. The RIE etch process, here used to structure the membranes, leaves rough side-walls with mostly diffuse scattering. Experiments by M. M. Leivo et al. [51] have shown a reduction of G in 200 nm thick membranes at 1 K with a factor of 10 when cutting the membrane into $50 \mu\text{m}$ stripes. At 4 K Leivo has not observed a reduction of G .

In summary, Holmes et. al. and Leivo et. al. found influences of surface scattering in 0.2 and $1 \mu\text{m}$ thick Si_3N_4 membranes at temperatures below 4 K. The material used for the membranes at KOSMA is $2 \mu\text{m}$ thick. Hence we assume that the surface scattering in this membranes is not dominant for the heat transfer through the membrane.

The phonons would have to go at least 4 times their mean free path, but the design is uncomfortably near to this limit. On the other hand these estimations are too vague for further conclusions.

When the membranes are used for phonon cooled HEBs, another mechanism might interact with the device operation. Phonons which escape from the HEB micro-bridge into the substrate might be reflected onto the bottom side of the membrane. Then specular reflected phonons might backscatter into the HEB and reduce the thermal time constant. Baubert et. al [52] recently presented theoretical considerations about the performance of phonon cooled HEBs on thin membranes. They estimated that a HEB on a 2 micron thick membrane would need about 3% less LO power due to the reduced cooling. The limit, how thin the membrane can become before the device performance becomes significantly reduced, has not been tested with these phonon cooled devices up to now. The heterodyne measurements of phonon cooled HEBs on freestanding 2 micron thick membranes are a step to investigate into this direction.

5.2.4 Estimated thermal transport in the membrane mixer

Assuming that the thermal conductivity in the membranes is roughly similar to that in bulk material, estimations about the thermal transport in the membranes can be made. These estimations can be compared with thermal transport in quartz bulk substrates. The 1 μm silicon nitride films described in (ref. [50]) showed a conductivity of about 0.4 W/mK at 4 K which is comparable to fused quartz. This leads to an overall conductivity of 1E^{-7} W/K for a 2 μm thick membrane which is 1.3 mm long and 80 μm broad. Being 15 times thicker than the membranes, the 30 μm thick quartz beams should have an accordingly higher thermal conductivity of about 1.5E^{-6} W/K. We do not know, if this difference of one order of magnitude is significant or can be compensated by adapting the mixer design.

Not only the substrate membrane can transport heat from the device to the mixer block. The IF micro-strip filter can be used for an additional heat transfer, to compensate the reduced heat transfer in the substrate. In the classical design for 800 GHz on quartz substrates, the RF/ filter and waveguide antenna probes are made of superconducting Niobium with a thin gold passivation and bonding layer. The superconductor material provides a low-loss coupling of the RF signal to the mixer, but it also has extremely low thermal conductivity.

To increase the heat transfer in the membrane setup and due to additional reasons (ch. 6.2), 300 nm thick gold is used for the IF filter structures instead of 250 nm Niobium. The superconducting Niobium only provides very small thermal conductivity. Using thick Au layers of 300 nm on the membranes adds a significant path for the heat transfer. The IF filter consists of micro-strip lines with differing width. The total conductivity is calculated by adding up the thermal resistances of all elements. Using

the same RF design as for the quartz substrates, the thermal conductivity is increased to about 2E^{-6} W/K. This value is comparable to the classic design with fused quartz and superconducting metallization.

To further increase the conductivity by a factor of two, the number of thin micro-strip lines with high inductance was reduced from 5 to 4 on each side. Additionally the width of these elements was doubled from 1 to 2 μm for the 1900 GHz design. This also simplifies the fabrication, as 1 micron wide micro-strip lines would be difficult to structure. 3D E/M simulations with CST, described later in chapter 8.1, were used to find a good trade off between optimizing thermal transport and RF performance.

DC and heterodyne measurements (ch. 9.6) were used to analyze the cooling properties of the membrane devices. According to these measurements, the cooling is not as efficient as with fused quartz substrates, but it is sufficient for the HEB operation.

5.3 Production of membranes together with support frames - Concept A

As mentioned in the introduction, we need extremely thin membrane which can be mounted freestanding and suspended into the substrate channel. A support frame provides the necessary mechanical stability for both assembly and operating of the devices. In this chapter **Concept A** *Production of membranes together with support frames* of the introductory section 5 is presented in detail.

In general we can divide the fabrication of the frame/membrane units in three basic sections:

1. device fabrication,
2. membrane structuring,
3. frame structuring.

The device fabrication will be discussed in chapter 8.2.

The frame and membrane production will be discussed in two sections, for two groups of semiconductor materials: GaAs- and Si-based materials. The general fabrication concept is similar for both groups. After the device fabrication, the membranes are structured. A mask which later has to be removed, is used to pattern the membrane material and to protect the sensitive devices. Then the wafer is glued device-side down onto a carrier wafer with wax or a similar material. This wax serves as the main protection of the devices for the following backside etch step, hence its properties are very critical. The bulk wafer is thinned by lapping down to the designated thickness of the later frame. The lapping leaves a rough surface, which cannot be masked properly. Thus it has to be polished with Chemical Mechanical Polishing (CMP) or/and with a suitable etch dip.

Then an etch mask is applied and patterned on the backside of the thinned wafer. Now the frames can be etched out of the bulk wafer, whereby the devices and the membrane strips have to be secured against the etchant. Here different methods can be applied for the corresponding processes. When the frame structuring is finished, the wax can be dissolved and the frame/membrane units are taken of.

5.4 GaAs based membranes

GaAs is an extremely brittle material compared to, e.g., Si. But it offers much larger freedom for semiconductor band-gap engineering. The As can be substituted in any proportion with Al whereby the height of the band-gap is reduced. Therefore it is

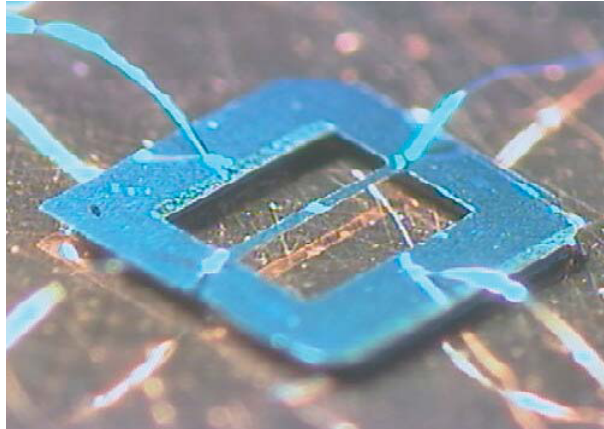


Figure 14: Freestanding GaAs membrane with support frame

possible to design etch-stop or membrane layers in nearly any sequence. Also the etch solutions which can be used here, are far less aggressive than those needed for other materials.

In this work, GaAs membranes with an etch-stop made of GaAlAs were used. The membrane base material was produced in cooperation with the Universität München [53]. The concept of etching is based on [45] and has been further developed at Universität München and at KOSMA.

The GaAs wafer material used has a 500 nm GaAlAs (50%Al) etch-stop layer and a 2200 nm GaAs membrane layer. The membrane layer has been structured with a combined etch process with the first step of HCl:H₂O 1:1 for 30 sec, and the second step of citric acid : H₂O₂ 6:1 for about 5 min. The device strips can be masked and protected with standard photo resist. The process halts at the etch stop layer. Then the membrane wafer is glued device-side down, onto a carrier with CrystalBond.

The membrane wafer is thinned down to 50 μm by lapping, and polished with CMP and an HCl dip. The frames can be masked and patterned with standard photo resist. A solution of H₂O₂ : NH₃ 19:1 is used to etch through the backside of the wafer down to the etch-stop layer. This takes about 45 minutes at room temperature. The etch-stop is not attacked by the backside etch, and subsequently it has to be removed with concentrated HF for about 5 sec. Now the finished frame/membrane units can be separated from the carrier wafer by solving the CrystalBond with acetone.

GaAs frame/membrane units have been successfully produced at KOSMA (see fig. 14). There have been problems with bending membrane strips, though. It looks as if the epitaxial membrane layer of the used wafer material has a different lattice constant than the bulk wafer. But there were also other reasons which led to the decision to look further for other materials:

The first point concerns the frame which takes up considerable space on the wafer. So only a few units can be fabricated with one wafer and these wafers are extremely expensive. This problem becomes enhanced because the fabrication of the HEB devices has a very low yield. The yield problem also applies to the Si frame/membrane unit fabrication at present. It was one of the main reasons to pursue **Concept B: Separate fabrication of frame and membrane** (ch. 6).

The second point of concern when GaAs is used is the high toxicity of arsenic. The base wafer has to be thinned down to 80 μm before it can be etched from the backside. This thinning by lapping produces GaAs powder as a waste product, which is highly toxic. In the facilities at KOSMA, this could not be tolerated for the high wafer throughput in the device fabrication stage. But if GaAs devices or structures are needed in the future, this problem might be solved involving new partners in fabrication, or with adapted facilities. Some device technologies, for example multipliers or quantum-well structures, need GaAs base material.

5.5 Silicon based membranes

Silicon unites several outstanding advantages for micro-structures.

- very robust especially in micro-dimensions,
- a vast variety of processes and know-how provided from semiconductor industry,
- fairly cheap.

In the following section the structuring processes for the two membrane materials Silicon and Silicon Nitride are discussed which have been used here. It is followed by a section about describing different frame fabrication schemes. The last section discusses the presented schemes and suggests the general concept pursued further.

5.5.1 Silicon and Silicon Nitride membrane structuring

Silicon and Silicon Nitride (Si_3N_4) have been used in the development of thin membranes. Both materials have been tested in parallel, whereby Silicon Nitride has become the material of choice for the developments pursued further. The experiences with fabrication of Silicon membranes will also be discussed here, because these might be needed for later developments. If it turns out, that e.g., phonon cooled HEBs have significantly higher performance on Si than on Si_3N_4 , these approaches can be used to fabricate thin Si membranes.

Silicon Nitride membrane development and fabrication For the fabrication of Silicon Nitride membrane, Si wafers with a low stress $2\ \mu\text{m}$ thick Si_3N_4 layer were used [54]. This membrane material is extremely robust. It can even be gripped with standard tweezers and bent to certain angles, provided the membrane is not folded. In our experiments, the intrinsic stress of the used material was so low that the membrane did not bend, even when the bulk wafer was totally removed. The later described concept of separate fabrication of membrane strips and support frames is based on this feature.

Si_3N_4 is inert against most wet etch solutions. So on the one hand, no additional etch-stop layer is necessary, but on the other hand, Reactive Ion Etching (RIE) is needed to structure the membrane. This process is very aggressive upon most mask materials. The wafer is exposed to the etching attack for considerably long total time of about 10-15 minutes, because $2\ \mu\text{m}$ of Si_3N_4 have to be removed. The development of the structuring process with a complex masking system is described in detail in chapter 6.3. There the identical process is used for the membrane structuring.

We can summarize, that the Silicon Nitride membranes can be produced reproducibly with acceptable effort and at moderate prize. Hence they have been used successfully for the device production up to now.

Silicon membrane development For the fabrication of Silicon membranes, Silicon On Isolator (SOI) wafer were used. When the bulk wafer is removed through backside etching, the process has to stop when the membrane layer is reached. Therefore we need an etch-stop layer between membrane and bulk wafer. In this case Silicon Oxide (SiO_2) is used, giving it the name *Silicon On Isolator*. It is extremely difficult if not impossible to grow thick crystalline Silicon on SiO_2 . Therefore a bare Si wafer is bonded onto the oxidized handle wafer. Then the bonded wafer is thinned down to the desired membrane thickness, e.G. $2\text{-}7\ \mu\text{m}$. The membrane Si can be structured by various etching methods. Because the structures are only a few micro-meter thick and $40\text{-}80\ \mu\text{m}$ wide, the etching is not very critical. It has to be taken care, though, that the etch-stop SiO_2 is not damaged. The SiO_2 is removed when the backside structuring is finished.

Unfortunately it was not possible to fabricate freestanding Si membrane structures with the SOI material available at KOSMA. They mostly broke during fabrication. Even if not all possible fabrication schemes have been run through, one point of concern has crystallized here. The used material had an oxide thickness of $2\ \mu\text{m}$ and membrane thickness of $2\ \mu\text{m}$. One conclusion might be that the membranes broke because of the intrinsic stress of the comparably thick SiO_2 . A custom-made batch of SOI wafers with the desired membrane films would have been far too expensive for the experimental research. Thus it was tried to work with left-overs from other industrial productions. The approach with SOI has also been used at the University of Virginia [48] to fabricate device membrane strips, but no finished mixers have been reported up to now.

Another possibility to fabricate thin Si membranes is the use of differently doped Si layers. Some etch solutions which can be used for backside etching, have different etch speeds according to the type and concentration of the doping. So the etch speed becomes reduced when the etch-stop layer is reached. At this point the wafer has to be taken out of the etch solution to prevent etching into the etch-stop or the membrane layer. The membrane layer has to be designed with high resistivity to prevent RF losses in the device substrate. Hence processes which are based on a highly doped membrane layer are excluded. The *porous Si etch process* described later can be used to fabricate thin Si membranes with high resistivity, because it selectively etches highly doped Si.

One reason not to pursue this technology here has been the high costs of basic wafer fabrication. In this case we need specially grown membranes, which have to be made by Molecular Beam Epitaxy (MBE). Standard doping processes are not feasible here, because it is extremely difficult to dope Si wafers into the depth of several micrometers.

5.5.2 Si frame structuring

The crucial part in this concept is the development of a feasible backside etch process. On the one hand, it must not damage the extremely sensitive HEB devices. On the other hand, it has to be aggressive enough to take down the chemically robust Si with sufficient speed. The processes developed and tried out in this work can be filed into three categories and sections, respectively:

- anisotropic base wet etching,
- Hydrofluoric wet etching,
- Porous Silicon etching.

The Inductively Coupled Plasma Etcher (ICP), which has recently become available for the KOSMA laboratory, might also be used in this context.

Anisotropic base wet etch etching The anisotropic wet etching of silicon with base solutions is a very common process in the Si micro-machining. Boiling KOH or Tetra-Methyl-Ammonium-Hydroxide (TMAH) show different etch speeds for the different crystal axes of Si. Using for e. g. [100] orientated wafers, it is possible to etch rectangular structures, as they would be needed for the frames, with 70° side-walls. TMAH has the advantage over KOH that it has high selectivity of 1:100 against SiO_2 . Hence SiO_2 can be used as masking and etch-stop. It cannot, however, be used as protection mask for the devices during the etching through the bulk wafer from the backside. First the risk of pin-holes, which might let TMAH diffuse to the devices,

is too high. Second with the given selectivity, a protection mask of at least 2 μm would be needed. The application of the mask and/or the removal of it would be very dangerous for the devices.

A significant effort was spent on the development of protection for HEBs during this etch process. Two main obstacles turned up, which have not been solved satisfactorily up to now. First the process temperature has to be above 70 °C for several hours. But the diffusion cooled HEBs, for which this process has been developed in the first place, are very sensitive to heat. Second, the hot base does dissolve or removes most materials which might be used to protect the devices against the etchant. As described in the introduction, wax or a similar material is used to glue the wafer device down onto a carrier for protection. If the sides of this sandwich are sealed, the etchant cannot reach the wax before the membrane wafer is etched through. But when the backside is etched through, the wax can be attacked and if it is solved, the devices are destroyed. In this work a variety of waxes and similar materials, for instance CrystalBond [55] or two-component glues, were tested. However it was not possible to find a suitable wax or glue which would withstand the etchant long enough to save the devices.

If the wafer has an etch-stop layer between the structured membrane layer and the bulk wafer, the etchant cannot attack the wax and so the devices are secured. This would apply, for example, for the above described SOI wafers when using TMAH for the etching. But here still the problems of the SOI technology apply as mentioned before. In principle Silicon Nitride membrane layers with an underlying etch-stop layer of SiO_2 can be fabricated, too. In both cases the protection with wax is not that critical anymore. But first new wafers with the right layer combination would have to be ordered here. Hence the further pursuit of this concept has been put on temporary hold.

Hydrofluoric wet etching Silicon can also be etched at room temperature, with acid etchants containing Hydro-Fluor (HF). HF can only attack SiO_2 so an oxidizing agent, for example HNO_3 has to be added. In most cases water or acetic acid is added to thin the solution. The characteristics of the solution can be read from diagrams in literature for the corresponding ratio of HF, HNO_3 and water or acetic acid [56]. In general these solutions are etching nearly isotropically. That means, that the etch speed is the same in all directions and it is difficult to produce three-dimensional structures like frames.

A recipe containing HF: HNO_3 :acetic acid in the ratio 1:3:10 (Vol) can be used, though, to produce structures with an aspect ratio of about 1:2. This is not much compared to the steep side-walls of the base recipes, but it can be sufficient to fabricate simple frames. The main drawback of the HF recipes is the high diffusivity and aggressive potential of the Fluor ions. Fluor ions peel off or dissolve most masking or protection materials. It even solves Niobium which in general is inert against most solvents. There is only Silicon Nitride and a few metals which can be used for masking. Metals, however, cannot be used because they can hardly be removed afterwards from the

HEB devices. Left on the membrane, they would short-cut the devices. The Silicon Nitride has to be stoichiometric and has to be applied at temperatures above 200 Deg C to be resistant against the HF. This could not be done at KOSMA, and it would have destroyed the HEBs anyway. Several materials were tested to glue the device wafer onto the carrier wafer for protection. In the experiments WWax by Apiezon [57] has been withstanding the HF for the longest time.

In chapter 6.5 a process with self-aligned gold etch-stop is described, which is applied only close to the membrane stripes and not onto those stripes directly. It can be used to additionally protect the devices during backside etching. This process was developed at KOSMA for the later presented Concept B: *Separate fabrication of membranes and frames*. In principle it could also be used here, but it has not been tested up to now.

The isotropic etching of HF solutions makes it difficult to structure frames. There might be a feasible combination with the previously described TMAH process, but it has not been tested up to now [58]. In this combination the frames are structured with TMAH, but the etching is stopped before the wafer is etched through. In this case it is much easier to protect the devices from the TMAH solution. Only the final etch through is done with a HF solution. In this short etching period, the isotropic etching has only a small impact on the frame structure.

Porous Silicon etching A less common way to structure Silicon is to make the Si porous before it is removed [59]. Si becomes porous in a solution of HF and Ethanol 1:1, when a bias current is applied whereby the wafer is one of the electrodes. It is highly selective to high n-doped Si, hence high resistivity Si can be used as membrane layer or as etch-stop layer. The use of an etch-stop layer in addition to the membrane layer increases the process security. The etch-stop layer remains untouched when the membrane is structured. Thus the backside etch solution cannot reach the front device side of the wafer, when the bulk wafer is etched through.

The porous Si can be removed extremely fast with a very light 1% KOH solution at room temperature. The properties of the porous Si can be determined in a large parameter space. One possibility is to produce vertical channels with sub-micron diameter. They can span hundreds of micrometers from one wafer surface to the other and are approximately rectangular to the surface. In general these channels are used as micro structures by themselves, but in this work it was tried to produce these channels in areas, where it was planned to remove the Si. After the removal, steep side-walls were expected at the interface between the original Si and the porous Si. Unfortunately it turned out, that the vertical channels can only be produced homogeneously when the whole wafer is made porous. When the wafer is patterned into areas, whereby some are not to become porous, we get interface sections of original Si and porous Si. At this interface to the original Si, where there are no adjacent channels, the channels also grow to the sides. But these side channels run underneath the etch mask and the etching becomes as isotropic as with other HF solutions.

Hence we can summarize the advantages of this process:

- membranes with high resistivity Si are feasible,
- membrane and etch-stop layer can be grown with low intrinsic stress on Si,
- room temperature process.

On the other hand we have the disadvantages and obstacles:

- highly concentrated HF etch solution,
- masking and protection problems similar to the other HF processes (but there is the possibility of an etch-stop layer),
- isotropic etching.

It is difficult to structure frames with the *porous Si* etching concept. The combination of this process with the TMAH process, similar as described for Hydrofluoric etching, might be a solution. The *porous Si* process on its own might be useful for the total removal of the bulk Si wafer. In the concept of separate fabrication of frame and membranes this would be the case. With the process presented here, it might be possible to fabricate frameless Si membranes.

5.6 Concept A - results

Silicon Nitride membranes have become the material of choice for the device fabrication. It is cheap, robust and inert against most backside etch solutions. One obstacle which turned up in all the processes tested, was the problem to find durable masking and protection materials. It must be possible to apply and to remove this material without destroying the HEB devices. None of the above described processes did provide the necessary features for a complete frame/membrane process. Two approaches might lead further from here: One way could be to combine the different processes in a smart way. Another way would be to shift to a different general concept. In this second option (**Concept B**) the frames and membranes are produced separately on different wafers. It is described in the following chapter. The different experiences and solutions developed for the previously presented **Concept A** have been implemented into this new approach.

In general the anisotropic base etch process is the best choice to fabricate frames with low effort. Thus it is chosen when frames without devices have to be produced. The isotropic HF etch process is used for the total removal of the bulk Si wafer to fabricate

Silicon Nitride membranes. For future developments the *porous Si* and the SOI etch process might be useful for the production of Si membrane strips.

But the technology transfer might also be interesting in the opposite direction: Some of the developments done for the following **Concept B**, might also be used to improve the processes described in **Concept A**. If the yield of the HEB fabrication should become significantly larger, not as many devices have to be fabricated on one wafer as it is necessary at present. Then this reason for the frameless fabrication concept would become negligible, because it would not matter, if the frame/membrane units take up valuable wafer space. In this case it might be interesting to use the new experiences for improved integrated fabrication of frames and membranes. Also the new ICP system might offer new opportunities here.

6 Development of HEB mixers on freestanding membranes using "flip-chip" mounting

One disadvantage of the frame/membrane concept (**Concept A**, ch. 5) is the relatively large wafer surface occupied by the support frames. As the process for the THz mixer devices has only limited yield, the chances of producing a sufficient number of good and - important for array receivers - identical devices are comparably poor.

This and some other points of concern, which will be presented later, have led to a fundamental redesign and optimization of the concept: separating the processes of fabricating the mixers and the Si support frames (**Concept B**). In some cases, e.g. for a silicon micro-machined mixer block, the support frame is not necessary at all. These processes are described in this chapter.

6.1 Separate fabrication of Si_3N_4 membranes and support frames - Concept B

In Concept B, the mixers are fabricated on wafers with a $2\ \mu\text{m}$ Silicon Nitride membrane layer, while the support frames are produced on similar, but separate wafers. Then the finished devices on their thin membrane strip substrates have to be mounted individually onto the frames, where they are electrically connected (fig. 15). The mounting process, of course, is delicate and requires a special process. We therefore developed an adapted "flip-chip" process, taking advantage of the KOSMA Micro Assembly Station 7.7. With this process about 400 devices fit easily on one 1" wafer, about 20 times as many as with the frame/membrane concept described previously, or with quasi-optical open structure devices.

A second problem of producing the frames together with the devices is solved with this approach at the same time. Anisotropic etching of the frames from the back side is necessary to achieve a reproducible mechanical interface to the mixer mount. Most reasonably anisotropic etch processes with high etch rates only work well at temperatures above 70°C . At this process stage, the wafer already carries the delicate and temperature sensitive bolometer devices on the front side, so that etch protection is of utmost importance. As described in the previous chapter (5.5), we have not found a reliable way of protection for small wafers. However a lot of experience and know-how has been needed to be implemented for this new process.

In the following sections, the processes of creating these membranes and the corresponding support frames are described. New process steps were needed for this task of creating such reliable and identical micro-structures.

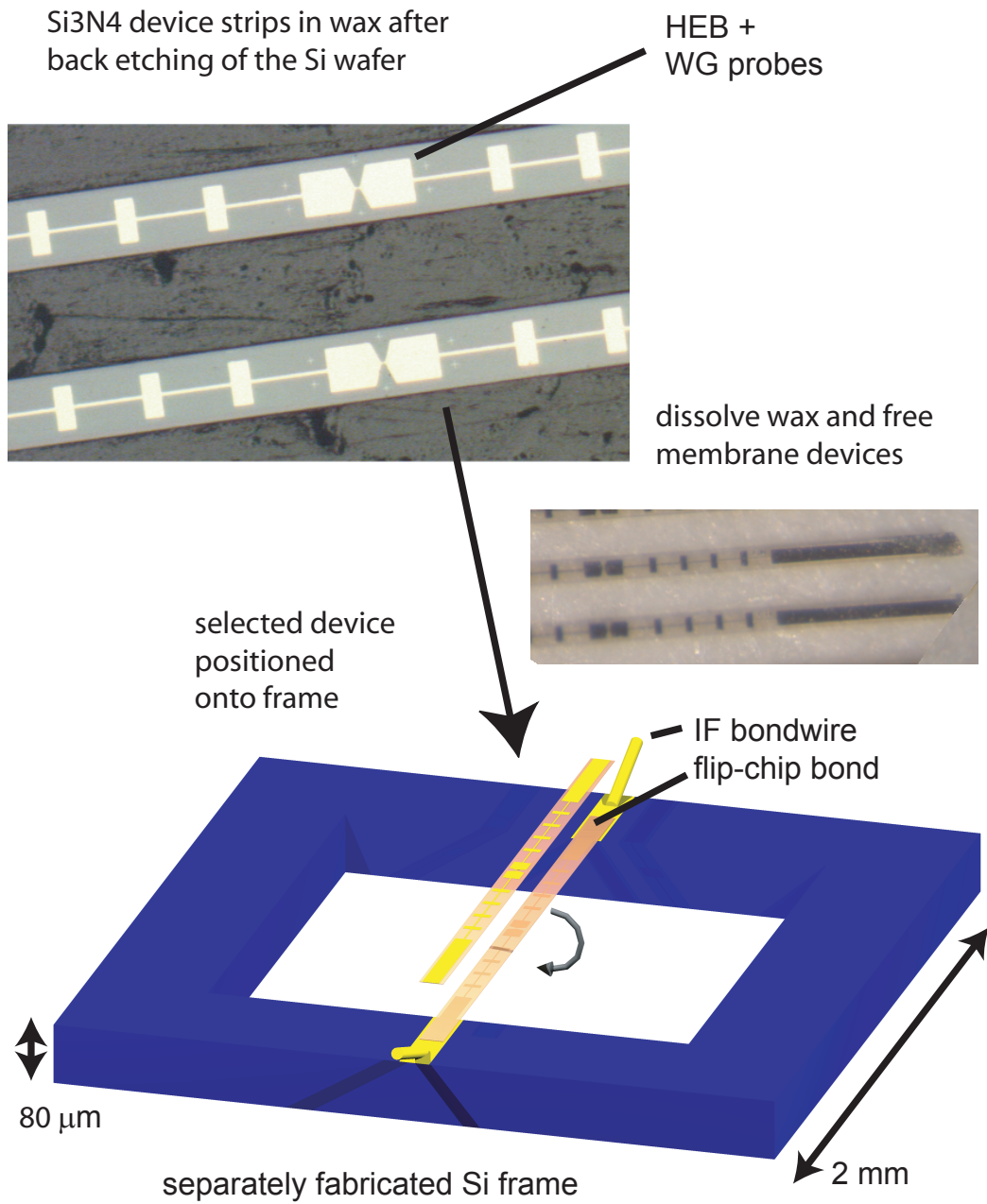


Figure 15: "Flip-chip" mounting of Si₃N₄ device membrane strips onto the Si support frame

6.2 Mixer device design and fabrication concept for freestanding membranes

The HEB devices are fabricated on a 2 μm thick, low stress Silicon Nitride (Si_3N_4) film deposited on a silicon wafer [54]. Up to now diffusion cooled (D-HEB) and phonon cooled (P-HEB) HEBs have been produced. Both have been tested in a heterodyne setup and have shown comparably good results. The process for the D-HEBs is the same as described by J. Stodolka in [30] with only minor changes. In chapter 8.2 a brief summary of this process is given. For the membrane devices, the IF filters, the waveguide probes and the bond pads consist of 300 nm Au instead of Nb. The RF structures have to be made of a normal conductor, mainly because of three reasons. First the Niobium has high surface impedance for the designated frequency of 1.9 THz. Second, the intrinsic stress of the Niobium would bend the membrane. And third, the thermal conductivity of Au is much larger than that of a superconductor. It is expected to compensate part of the reduced thermal conductivity of the membrane. The bond pads, which are later used for the "flip-chip" bonding, are also made of 300 nm thick gold for good electrical and thermal contact. Hence all these listed elements of the device structure can be made in one process step, as all need the same material properties.

The films for the P-HEBs were developed and fabricated by Sven Bedorf [36] while the actual P-HEB device fabrication was done by P. P. Muñoz [60].

In the last step the Si_3N_4 membrane is cut into 80-140 μm strips with Reactive Ion Etching (RIE). These strips are going to be the membrane beams which will span freestanding through the substrate channel and across the RF waveguide channel. For 1.9 THz these strips are scaled down to a width of 40 μm .

In the following sections, the different complex etching processes are described which were specifically developed for this application in micro-machining. The process development has been rather difficult, because the diffusion cooled HEBs are significantly more sensitive to heat and electrostatic discharge (ESD) than, for example, semi-conductor devices.

6.3 Si_3N_4 etch process development

It is very difficult to etch Si_3N_4 as it is inert to most chemicals. Another point is the thickness of 2 microns. Wet etch processes would take a rather long time and would not be anisotropic enough to structure these membranes. The best choice therefore is to use Reactive Ion Etching (RIE) with a fluor based process gas. Here the silicon nitride is removed through a bombardment with positive F^+ ions and excited Fluor molecules. At the same time the highly aggressive F^+ ions chemically attack the Silicon nitride and build volatile compounds with the removed material. The volatile components

are pumped out of the process chamber through the turbo molecular pump. The F^+ -ions themselves are produced in a radio frequency plasma (RF-plasma) between two electrodes. The positive ions are much slower than the electrons which can leave the chamber through the grounded chamber housing. This leads to a potential difference (self-bias potential) between the plasma and the electrically floating substrate table, which accelerates the positive ions in the direction of the substrate.

The process was optimized with process pressure of 100 μ Bar NF_3 and self-bias potential of 80 V. Higher voltages did not significantly raise the process speed, but they increased the problems with etching through the silicon nitride into the bare silicon. After every 2 minutes of etching, a cooling break of 2 minutes was introduced to reduce the thermal impact on mask and devices. A total etching time of 12 minutes has been needed to etch through the Si_3N_4 membrane.

In the near future, the use of an ICP etch system, which has recently become available at KOSMA, might further improve the membrane etch process.

6.4 Si_3N_4 etch mask development

The combination of F^+ -Ions with high kinetic energy also attacks the etch mask. It can lead to its total degradation, especially as etching through 2 μ m can take more than 12 mins. Thus the development of an etch mask which is durable but also removable, has been the most critical part in the membrane etch scheme. As mentioned before, the etch mask does not have to be designed to withstand the backside etch of the wafer, due to the improved frameless process. But three other points have to be taken into consideration.

First, the topography differences are nearly 400 nm because of the RF filter structures. In this thickness metals would leave insufficient edge coverage, so that photo resist has to be used. Second, the mask application and removal must not have a negative effect on the HEB devices. Third, the thermal impact of the etching on the devices should be kept at minimum. These points speak against metals as etch mask in favor of a dielectric or photo resist mask. Here the focus was set on photo resist masks, leading to the specific approaches of step covering and utilizing the potential of self-aligned lift-off processes. These processes will be described later in this section (ch. 6.5). In the following section three processes are described which have been developed and tested. The third process is successfully used for the device fabrication.

6.4.1 AZ series photo resist multi-layer RIE etch mask

AZ 7218 [61] is spun onto the wafer at 2000 rpm and thus it becomes 2.2 μ m thick. It degrades with NF_3 with about 0.5 μ m/min, when used for the reactive ion etching.

Hence for 15 minutes of etching time, more than 6 μm thickness are needed. The AZ 7218 resist can be used in several layers, but the application becomes more and more critical with every additional layer.

Even with 4 layers of resist the process has not been reliable. When the Silicon Nitride is etched through, the Silicon of the base is attacked. At this moment we observed a fast degradation of the resist. The used etching recipe has a significantly higher etch rate in Si than in Si₃N₄. The degradation might be related to a corresponding change in the etching chemistry. As a result, this recipe could not be used for the device fabrication.

6.4.2 AZ/SU-8 resist multi-layer RIE etch mask

The resist SU-8, described in chapter 7.4, not only has outstanding capabilities for high aspect micro-structures, it also withstands most chemicals known. It is one of the few resists to cope with HF and KOH for considerable time when used with adhesion promoter. The same capability, on the other hand, makes it nearly impossible to remove it after the etch process. Therefore a little trick was developed here: A buffer layer was introduced underneath the SU-8 which can be easily removed. It enables a kind of lift-off process for the SU-8. The buffer layer only offers a very small flank at the side of the multi-layer which can cope with the NF₃ attack. Also only the chemical component of the etch attack has to be taken into account, as the ions diffusing from the side underneath the SU-8 have negligible kinetic energy.

For the buffer layer, another AZ 7212 [61] resist was used. It is applied and baked out in a process similar to the previous one, and subsequently the SU-8 is spun onto the wafer. It is used with a high ratio of solvent to make it highly viscous. Thus it forms a thin layer of 2-4 μm . It has to be baked after spinning and after exposure. When developed the non-exposed parts are dissolved together with the buffer layer. Subsequently the wafer is ready for the RIE etch step. The SU-8 can withstand the etching, even when the process is not stopped in time and the Silicon adds to the process chemistry. Finally it can easily be removed with the help of the buffer layer by applying acetone after the RIE step.

Despite obvious advantages of this complex process, the main disadvantage of the use of SU-8 - next to its long bake-out times - is its tendency to develop bubbles in thin layers which are extremely difficult to avoid. These bubbles can cause a breakthrough of the RIE etchant which would destroy the devices. But as the buffer layer concept itself proved to be very promising, a replacement was needed for the SU-8. This has led to the development of the final process described in the next section.

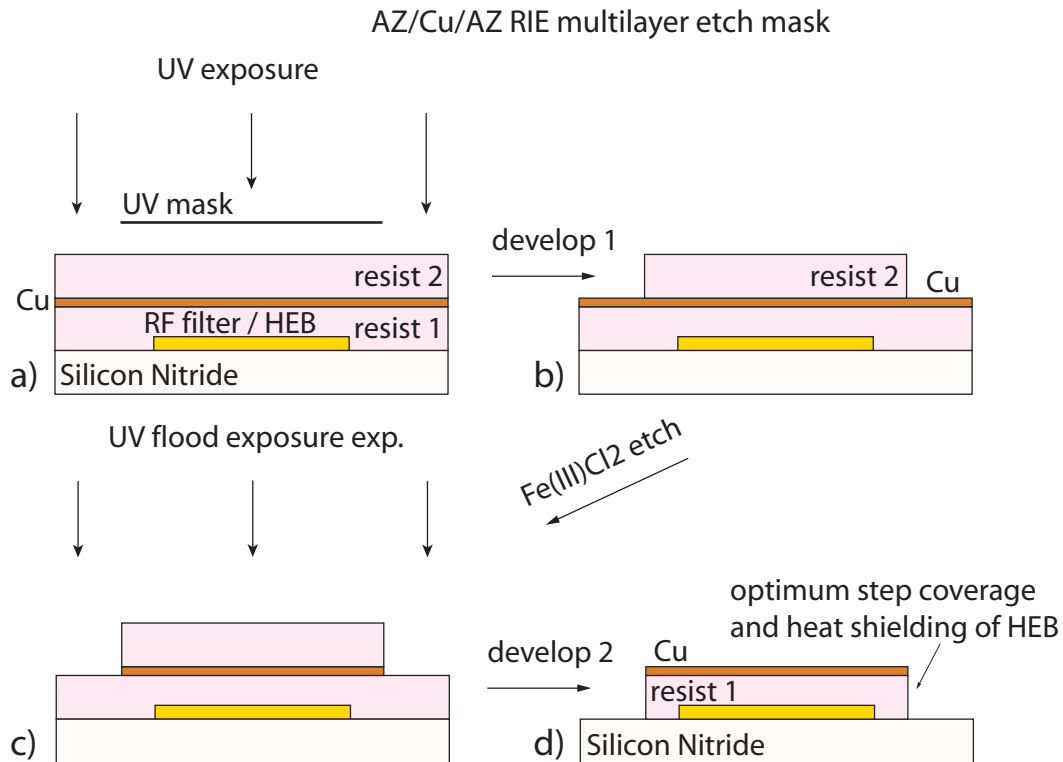


Figure 16: Fabrication of the AZ/Cu/AZ multi-layer etch mask for the RIE Silicon Nitride etch process

6.4.3 AZ-resist/Cu/AZ-resist multi-layer

As mentioned before, certain metals like Al, Au or Cu can be used as etch masks for NF_3 . By usage of the buffer layer as described before, the obstacles of removability and step-covering mentioned there, can be bypassed. Hence in the first etch masking tests, aluminum was DC-sputtered on top of the resist. As the sputtering plasma exposes the resist, it can be dissolved in the last development step, undercutting the multi-layer structure.

It proved to be much better, however, to deposit the metal via thermal evaporation without a previous plasma clean. This showed even better results than the AZ/SU-8 process. The materials tested here were gold and copper, whereby copper was chosen in the end. For some unknown reasons, the gold process sometimes failed when gold was attacked in the RIE step. After achieving good results with the copper process, the reproducible process for the device production was established. It included implementing a new infra-red oven (IR-oven) specially designed for this process.

Thus the final fabrication process was designed as follows here.

In the first step, AZ 7212 is spun onto the wafer and baked out at 120°C on a hot plate to bake out the solvent. Then a 150 nm thick copper intermediate layer is thermally evaporated onto the resist. There is no previous plasma clean step done in the evaporator to prevent resist exposure. After the deposition, right before the spinning of the second resist, an oxygen plasma clean is done in the RIE chamber. This cleans the copper layer to enhance the sticking of the second resist onto the metal. The first resist is not exposed, as it is covered by the copper layer.

Now the second resist layer of AZ 7212 is spun onto the copper and baked out in the IR-oven. As mentioned before, the IR-oven was specially developed for the baking of thick SU-8 and multi-layer resist films. It consists of a ceramic heater element with a reflector which focuses the radiation onto the wafer. The oven itself is kept open and stays cold compared to a normal oven. The main vaporizing effect on the resist solvent is therefore done by the IR radiation rather than by thermal means. The bake-out takes 3 minutes, whereby the wafer temperature increases to 90°C.

Before the actual exposure can be done, the rim of the two resists at the edge of the wafer has to be removed. It can be several micrometers thicker than the overall resist. This would keep the exposure mask too far above the wafer and would prevent precise mask structuring. The rim is exposed with a special mask which blanks out the center of the wafer where the devices are located. Then the wafer is developed to remove the rim. Now the mask for resist 2 can be aligned and exposed for the silicon nitride structure (fig. 16 a).

After developing resist 2, the copper can be removed at the exposed areas with highly thinned and filtered Fe(III)Cl₂ etch solution. The now structured Cu layer works as the intrinsic exposure mask for resist 1 at the next flood exposure step (fig. 16 c). After a last development step and a final bake to harden the multi-layer, the etch mask is ready for the RIE step (fig. 16 d). The areas where the silicon nitride is to be removed are open. The devices are covered by 1.2 microns of resist and 150 nm of copper which can reproducibly withstand the 12-minute silicon nitride etch.

6.5 Self-aligned lift-off for backside etch-stop

After RIE, a gold layer is deposited to cover the silicon area between the strips using the same photo resist for lift-off (fig. 17). This gold film protects the strips from being attacked by the etch solution when it breaks through from the backside. Then the resist is solved in acetone and the copper removed. Subsequently the wafer is again covered with a closed layer of etch resistant material, either with gold or silicon nitride. Now the only way for the backside etchant to reach the device side of the wafer is via pin holes in the gold layer, or at the edges to the silicon nitride. To control these comparably small attacks of etchant, wax has been introduced as sufficient barrier, as described later.

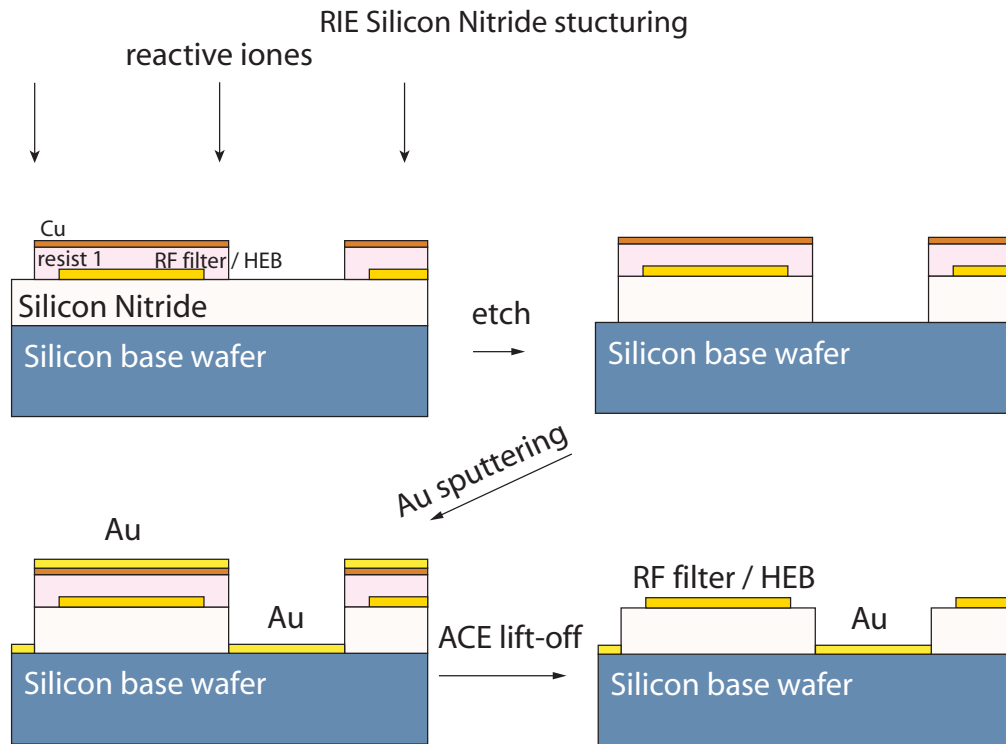


Figure 17: Reactive Ion Etching (RIE) of the Si_3N_4 membrane and self-aligned lift-off for gold backside etch-stop.

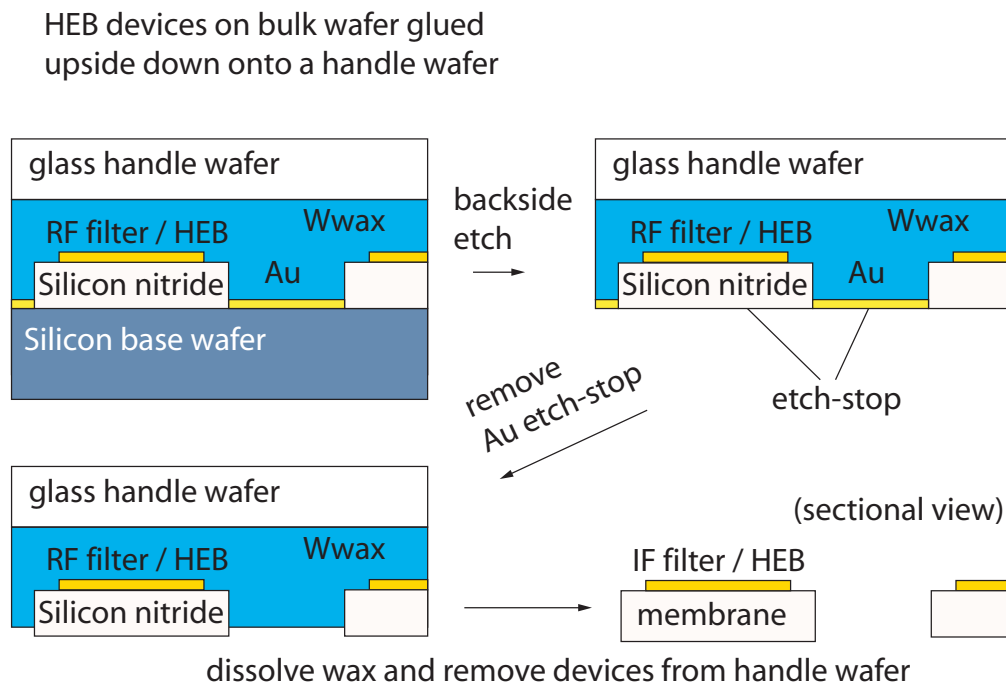


Figure 18: Backside etch process for the total removal of the Si bulk wafer.

6.6 Intermediate DC-characterization

Before the wafer is further processed in the clean room it is taken out for the first DC-testings. The wafer is sliced into small pieces of 33 devices. Furthermore ground connections are cut to allow DC-testing of the devices while they are still supported by the bulk wafer. Testing the devices at this stage of the process is significantly easier than to electrically contact the separated membrane strips. It would also be difficult to measure the individual temperatures for the R/T characterization. Only the most promising devices with the specified parameters are mounted into the mixer block. The standard DC testing and characterization procedures are described in chapter 9. After successful DC-testing, the manufacturing of the devices is continued by the back-etching of the support wafer.

6.7 Backside etch of Silicon base wafer

6.7.1 Process development

A critical part of the process is the final back-etching of the supporting Silicon wafer, leaving the devices on free-standing Silicon Nitride strips. Obviously this etch process does not have to be anisotropic. Still, all isotropic recipes with reasonable etch rates either use HF, or they need about 80°C process temperature. On the one hand, long exposure to higher temperatures deteriorates the bolometer characteristics. HF on the other hand, attacks nearly any material or peels it off, making it difficult to find suitable masking materials (see ch. 5.3).

First experiments in the development of this process were done with a slow etching solution containing $\text{Cu}(\text{NO}_3)_2$ and NH_4F . It has a selectivity to SiO_2 . Thus SiO_2 can be used as etch stop and passivation for the HEBs. In contrast to this first idea, a very fast etch step with a highly aggressive etchant containing fluorid acid (HF), nitric acid (HNO_3) and acetic acid, gave the most reliable process (HNA etch process). It seems that the total time of exposure of the wafer to the etchant is very critical, as the F-ions have extreme ability to diffuse through most barriers. This is the main reason for the gold etch stop which had been applied after structuring the Silicon Nitride. The F-ions can diffuse, though slowly, along the W Wax /refWwax wafer interface. The gold prevents the ions to reach this interface.

The ratio of HF, HNO_3 and acetic acid controls the speed and the quality of the etched surface. If cracks are etched more slowly than the plane surface, these cracks are removed and levelled out leaving a smooth surface. If edges are etched with a different speed than the plane surface, it leads to a convex or concave etch front. In both cases, certain parts of the wafer are etched through faster than others, increasing the risk of etchant by-passing the etch stop and destroying the sensitive device structures on the wafer front. If however, the etch speed at the outer parts of the wafer is slightly

faster, the Silicon in the center vanishes last. Therefore the under-etch will be smaller in those areas where the HEBs are positioned. This process was optimized with the volume ratio of 3:5:3 of HF(48%), HNO₃(65%) and acetic acid(100%), with the etch rate of about 0.4 $\mu\text{m/s}$. Thus the wafer is left inside the solvent for about 3 mins.

6.7.2 Membrane Fabrication

As described above, the devices had been DC-tested during an intermediate production step. The bonding of the wafer for this DC characterization in the dipstick leaves residues on the auxiliary bond pads. For their removal these auxiliary bond pads are sawn off. On the other side, the devices are still connected with the common ground line.

Subsequently the wafer is glued onto a glass sub-wafer with W Wax by Apiezon [57]. The levelling should be in the range of $\pm 5 \mu\text{m}$. The homogenous covering of the wafer is very important for the later silicon etch step. It can be controlled through the glass sub-wafer. The glass sub-wafer itself is glued onto the glass carrier of the lapping machine. In difference to the previous step, standard bee wax with a considerably low melting point is used here. This enables the easy removal of the wafer-sub-wafer sandwich of the glass carrier. The silicon wafer is lapped down to a thickness of 150 μm with 9 μm slurry. Then the system is changed to 1 μm slurry and another 70 μm are lapped off. The final thickness leaves a bit of tolerance as the silicon is going to be fully removed during the next step.

The wafer-sub-wafer sandwich is taken off the heated glass carrier. It is very important not to spoil the lapped surface with wax of any sort which might work as an unwanted etch mask in the later processes. The rest of the silicon wafer supporting the silicon nitride membrane, is removed with the HNA etch solution mentioned previously: it contains HF, HNO₃ and acetic acid. After about 3 mins the RF metallization shines through. When all of the silicon has disappeared the wafer is taken out and rinsed with water. Finally it is cleaned twice in water for 10 mins.

Before the wafer is further processed it is controlled under the optical microscope to check for silicon residues. If there are such residues the wafer has to be etched further. The gold etch is removed with J/JK solvent until the black W Wax is plainly visible. Here a further process step can be inserted for better handling of the membranes with the Micro Assembly Station. Before the membrane structure is removed from the wax, a glass beam of 0.2x0.2 mm and about 2 mm length is glued onto the ground line with Stycast [62]. The glass beams are residuals of the classical device sawing. The finished Silicon Nitride membrane with or without beam is taken off the glass wafer and cleaned with TRI and acetone. The device strips are still connected to each other on the ground side, giving the membrane a comb-like structure. But even this assembly of about 30 devices is so light-weight that it is reasonable to wear mouth

protection to prevent breathing the membrane away by accident. Hence it is necessary to secure these extremely sensitive devices and make them manageable, as described in section 6.8 after the following section.

6.7.3 Fabrication of the silicon support frames

The first task of mounting is the fabrication of support frames. Because of the separate fabrication, these can be made in sufficient numbers and stored. The support frames are made of the same Si wafers with a $2\ \mu\text{m}$ Si_3N_4 layer. Two Nb/Au auxiliary bond pads are then deposited for each frame, and the Si_3N_4 is structured to serve as the etch mask for the frame patterns. The frames are etched with TMAH at $80\ ^\circ\text{C}$, which produces anisotropic TMAH 70° side walls in $\langle 110 \rangle$ Si, into a depth of about $150\ \mu\text{m}$. Finally the Si wafers are thinned down to $80\ \mu\text{m}$ from the backside by lapping. As the the TMAH structuring goes deeper than the lapping, the frames are now getting separated. Together with the auxiliary bond pads, more complex metallization structures on the frames can be made to incorporate IF matching circuits.

6.8 "Flip-chip" membrane bonding

For reproducible and secure handling, the $2\ \mu\text{m}$ thick membranes are mounted onto a silicon frame, implementing an adapted "flip-chip" process. It provides the mechanical, thermal and electrical connections at the same time. This frame unit is then fine positioned and contacted.

In the first step, the silicon support frame is glued into the copper mixer block structure with W Wax [57]. It fits into the depression surrounding the waveguide structure with enough tolerance to enable later fine-adjustment. The block carrying the depression is heated to $95\ ^\circ\text{C}$ to apply the wax and to glue in the frame. Subsequently it is cooled down to room temperature again in order to mount the membrane. This process of mounting the micro-device onto the block is described as follows, in some detail.

6.8.1 Handling and positioning of the device membrane structure

The membrane strips to be mounted are still connected on one side to the ESD protection or grounding line. This kind of comb structure is now laid onto the frame with the metallization facing downwards. If a handle has been glued to the comb structure as mentioned before, it can be gripped and handled by the KOSMA Micro Assembly Station 7.7. All devices are laid out in parallel to each other, due to the comb like structure of the membrane. They can be moved back and forth until the selected device is hanging exactly over the substrate channel. The waveguide probe has to be roughly centered in the RF waveguide. The structure can then be lowered until the

Flip-chip Mounting with KOSMA Micro Assembly Station

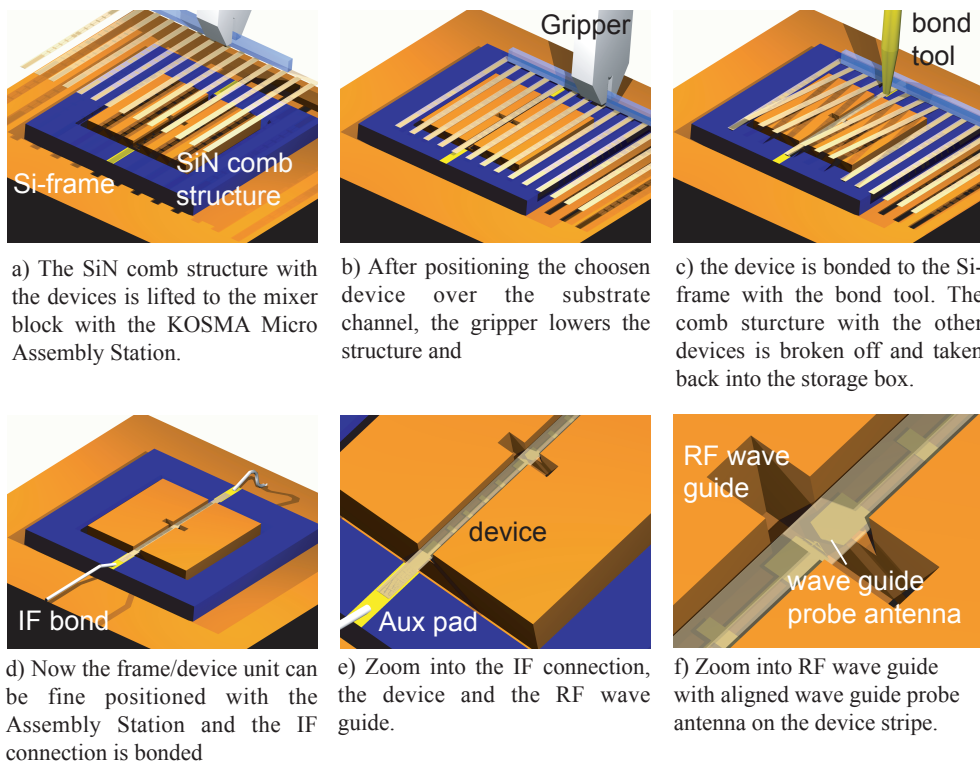


Figure 19: "Flip-chip" mounting of the Si_3N_4 comb structure with the KOSMA Micro Assembly Station

device substrate comes to lie inside the substrate channel with its bond pads located on the auxiliary pads of the frame. These devices show a certain amount of adhesion to the frame, as most microparts do, which keeps them in place even when the gripper has been opened again and driven away.

If no handle has been applied to the membrane, the handling has to be done manually. In this case a single hair, which has been a little bit pulled out of an antistatic brush, is used. It is shoved between two device strips and the common ESD line to take the membrane up and transport it to the frame. The whole "comb" is dangling from this single hair. To ease the identification of the individual devices, every tenth device has got a different, distinguishable bond pad.

6.8.2 "Flip-chip" bonding of the device membrane

The two bond pads of the support frame should now lie directly underneath the bond pads of the mixer device. The bond tool is changed to a brass needle with a flat stamp of 100 μm radius. It is used to ultrasonic-bond the pad of the mixer device onto the pad of the frame. To prevent cracking of the membrane, a test bond impression of the needle is done on the copper block. It should be round and homogenous. Otherwise the needle has to be changed or it may just need to be tilted and realigned. The depth of the depression is a hint for the actual bond force, but it is difficult to describe it in absolute numbers. This process needs a fair bit of experience. The best way is to start with parameters for which the depression is hardly visible, and to repeat the bonding with increasing force and ultrasonic power until the membrane is securely attached to the frame. The membrane is quite flexible so it can be bent a little to check the strength of the bond. The bonds which in tests had taken a little bending, did not go off with thermo-cycling. But it is sensible to dipstick a finished block to 4.2 K and to check whether the device is still alive.

When the first bond is done on one side, the membrane should stretch through the substrate channel. Sometimes it rotates a little bit, and if it is pressed to the sidewalls of the substrate channel it might bend. In this case the block has to be heated up again, releasing the stress by rotating the frame, and therefore realigning the strip to the channel.

6.8.3 Final assembly and fine-positioning of the frame/membrane unit

If both bonds turn out all right, the remaining devices with the common ESD line can be broken off by applying pressure onto the ESD line with the needle. As it runs outside the frame it is not supported and will tilt. Thus the chosen mixer device should break free. The membrane usually cracks where it runs over the edge of the frame. This is another test for the strength of the bond connection. If it should go off, it still

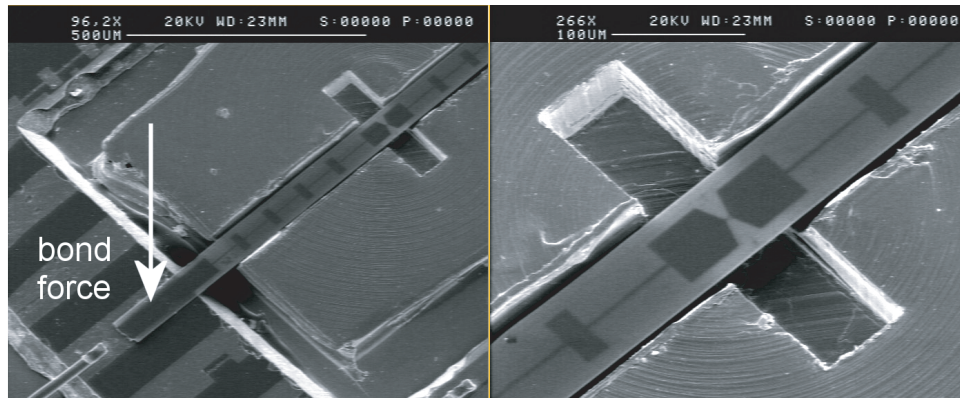


Figure 20: SEM photo of "flip-chip" mounted HEB device. The left photo shows one part of the frame with the IF bond wire connection, the right photo shows a close-up of the RF waveguide and the freestanding device substrate. The substrate channel is $40\ \mu\text{m}$ deep.

can be rebonded at the same position. The remaining devices are taken back into their ESD protected storage.

The resulting device/frame assembly can be easily handled, put into position and electrically connected via the bond pads of the frame. With the help of the KOSMA Micro Assembly Station (K-MAS) this unit can be positioned and aligned with an accuracy of microns. For this the W Wax is heated to 95°C again with the heater of the K-MAS. It makes the wax soft enough to shove the frame into the right position. The waveguide probes, situated halfway along the membrane strip, have to be centered in the RF waveguide in order to allow coupling to the incoming signal. Also the RF filters have to be aligned to the substrate channel for proper IF matching.

The mixer-frame unit can without problems be taken out of the block in order to assemble it in a different block, or to store it for later reuse. In our tests, some of these units have been taken out and reassembled several times without loss.

The bond pads on the support frame are only partially covered by the membrane strip. Standard bonds can be set next to the membrane onto the frame bond pads to connect one side to the copper of the block and the other to the SMA connector. Figure 20 shows the assembled membrane device and the IF connection in a SEM picture. For improved IF transmission it would be recommended to set two or three bond wires in parallel to decrease their inductance.

6.9 Summary, conclusion and outlook of the membrane substrate concept

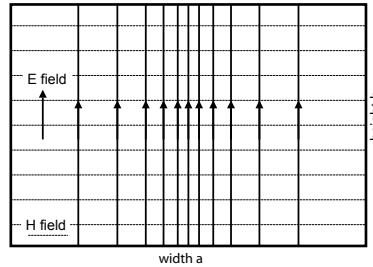
A practical and reliable fabrication process for freestanding Si_3N_4 membranes with HEB devices has been developed and successfully integrated into the production chain at KOSMA. The DC and RF measurements described later, have not indicated that the membrane process degrades the device process. For further projects, other membrane materials might be useful.

7 Fabrication of waveguide structures and feed horns for THz frequencies

The mixer devices on the membranes, as described in the previous chapter, have to be mounted into a waveguide structure which leads the RF signal to the mixer. The waveguide system consists of the horn antenna, a RF waveguide with backshort cavity and substrate channel (fig. 21 and ch. 3.2). At 2 THz, waveguide channel dimensions below $60 \mu\text{m}$ are needed which are a challenge to fabricate with classical metal cutting tools in copper. But here we reach the limits of classical technology and totally new ways of fabrication have to be considered especially when 2 THz is not taken as limit for further developments. Hence we are investigating photolithographic and etching methods to fabricate waveguide structures.

For the fabrication of broadband waveguide antenna horns even smaller and much more complex structures are needed. The following chapter discusses the limits of classical mechanical fabrication and presents new approaches, which can be realized at KOSMA or in cooperation with other micro-technology companies and institutions.

7.1 Basic waveguide theory



Inside the waveguide electro-magnetic waves (e/m waves) can propagate if their frequency f_{RF} is above the cut-off frequency $f_{cut-off}$ [63]. The cut-off frequency is defined by the waveguide width a (rectangular waveguide) which has to be larger than half the signal wavelength λ_0 . Signals with a frequency in the interval

$$f_{cut-off} < f_{RF} < 2f_{cut-off} \quad (52)$$

can only propagate in a *single-mode* or *fundamental-mode*. At $f_{RF} \geq 2f_{cut-off}$ other modes than the fundamental mode can propagate. But for the mixers presented here, fundamental mode waveguides are necessary mainly due to three reasons. First, a guided fundamental mode wave can be coupled most efficiently to the beam of the telescope. Second, efficient waveguide probes are designed to couple to the fundamental

mode. Especially the first mode above the fundamental mode ($f_{RF} = 2_{cut-off}$) couples particularly poor to the probe. Third, the higher modes do propagate with higher dispersion.

Hence the waveguides presented here are designed for frequencies between the cut-off and twice the cut-off frequency. In the case of 1.9 THz this would lead to a waveguide width of 130-150 μm .

The ratio of width a and height b of the waveguide channel determines the impedance Z_ω for a certain frequency.

$$Z_\omega = \sqrt{\frac{\mu_0}{\epsilon_0}} \frac{\lambda_L}{\lambda_0} \frac{2b}{a} \quad (53)$$

λ_0 is the free space wavelength of the signal, while λ_L is the wavelength in the waveguide. It is reduced compared to the free space wavelength as a function of the cut-off wavelength λ_c :

$$\lambda_L = \frac{\lambda_0}{\sqrt{1 - (\lambda_0/\lambda_c)^2}} \quad (54)$$

The commonly used full-height waveguides with a $b:a$ ratio of about 1:2 have a impedance of several hundred Ohms. This impedance can be matched to phonon cooled HEBs of 100-200 Ohms with waveguide probes. Diffusion cooled HEBs impedances are in the range of 10-20 Ohm. Half-height waveguides with a $b:a$ ratio of 1:4 have a smaller impedance, which is easier to match to the diffusion cooled HEBs. But at high frequencies as 1.9 THz, the reduced channel height of 33 μm can become an obstacle in the production.

The impedance of the waveguide probe also depends largely on its distance to the backshort. At THz frequencies, fixed tuned backshorts are preferred to movable ones, mainly because of two reasons. First, the fabrication of a movable backshort of micrometer dimensions with good electrical contact to the waveguide sidewalls is extremely difficult. Second, the small value of the optimum distance between backshort and probe of about $\lambda/4$ would be too narrow for a movable backshort, because the risk of collision with the probe would be too high. The backshort can also be positioned in other multiples of the wavelength, but then the RF bandwidth of the cavity is significantly reduced. The disadvantage of the fixed tuned design on the other hand is that exact simulation and modelling are needed to specify the backshort position for the production. Tolerances in the fabrication of the waveguide and the backshort or inaccuracies in the calculation can cause mismatch between the HEB and the incoming RF signal, and part of the signal gets reflected.

Hence we can summarize that the whole waveguide environment with RF waveguide probes and IF filters has to be carefully designed and simulated as discussed in chapter 8.1 and that these specifications have to be kept in the fabrication.

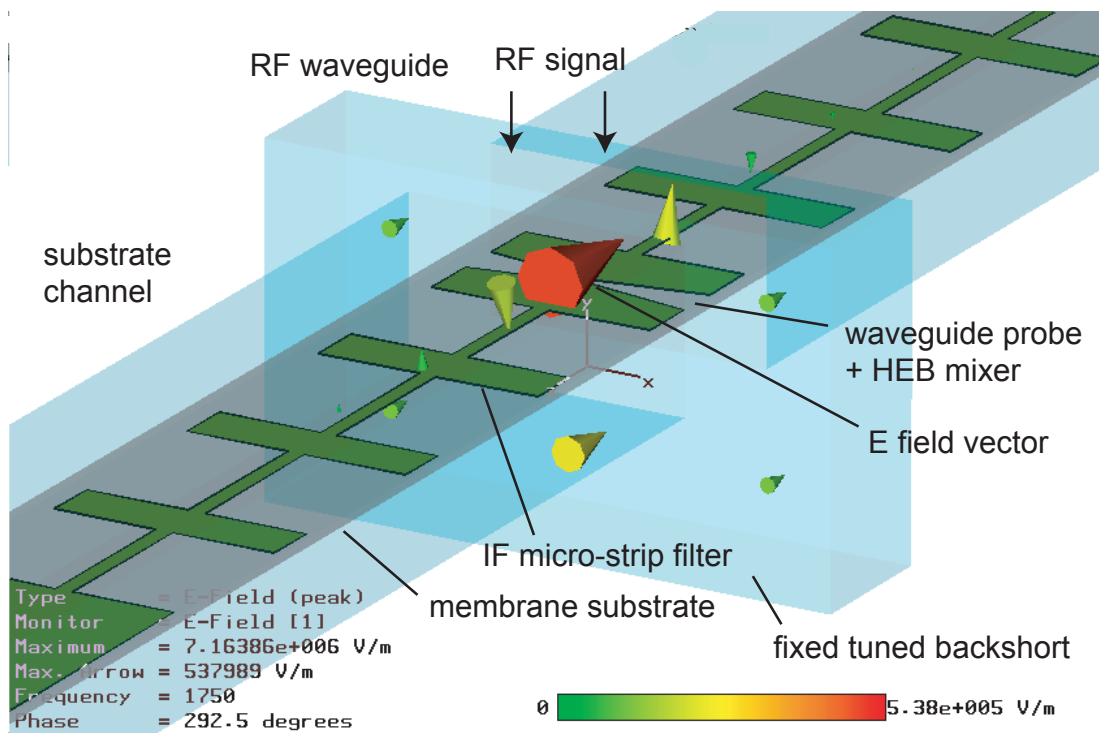


Figure 21: Mixer model

7.2 Waveguide technology development for 2 THz

In the early phase of this work it was not clear, whether the needed waveguide specifications for 2 THz could be met with the classical fabrication at KOSMA. Therefore feasibility tests with the fabrication in the KOSMA workshop and with alternative approaches were done in parallel. This section summarizes the achievements and limitations of these technologies.

In the following table, the most critical dimension are presented for 800 GHz and 1900 GHz mixer blocks. The two types of full height and half height waveguides for the different types of HEB devices are filed in separate rows. The maximum substrate channel width varies for the type of substrate used. The fused quartz substrate is glued directly onto the channel ground. Hence the lower part of the channel is filled with a dielectric. The freestanding membrane design defines a suspended substrate, which can be operated with a significantly wider channel (ch. 8.1).

The last column shows the achievements reached with the classical technology of the KOSMA workshop as discussed in the subsequent subsection.

frequency waveguide channel	800 GHz [μm]	1900 GHz [μm]	KOSMA classic fab.
half height waveguide	325 x 81	143 x 33	failed
full height waveguide	308 x 116	133 x 59	OK (limit)
substrate channel height	100	40	OK
suspended sub. ch. width	150	70	OK (limit)
dielectr. filled sub. ch. width	100	40	failed

7.3 Classic fabrication of copper waveguide structures at the KOSMA workshop

The KOSMA mechanical workshop developed a mainly automated fabrication process with self-developed tools for the waveguide structures in the mixer mount. It includes levelling of the mount surface, stamping of the backshort cavity and dicing of the substrate channel. Then the mixer mount is carefully inspected and measured. The differences between design and measurement are taken to calibrate the machinery. The fabrication process itself takes only several minutes and can be applied repetitively to the same block. In this way the operator can reach tolerances of a few microns by iterative approximation.

The main lower limit for the RF waveguide dimensions are given by the stamping tool. Stamp sizes of 143 x 33 μm for a half height 1.9 THz waveguide have been reached, but the stamp broke when used. Only stamps with more than 50 μm height had sufficient stability to produce repetitive structures. In this way 1.9 THz, full-height waveguide mounts for phonon cooled HEBs have been successfully fabricated. But

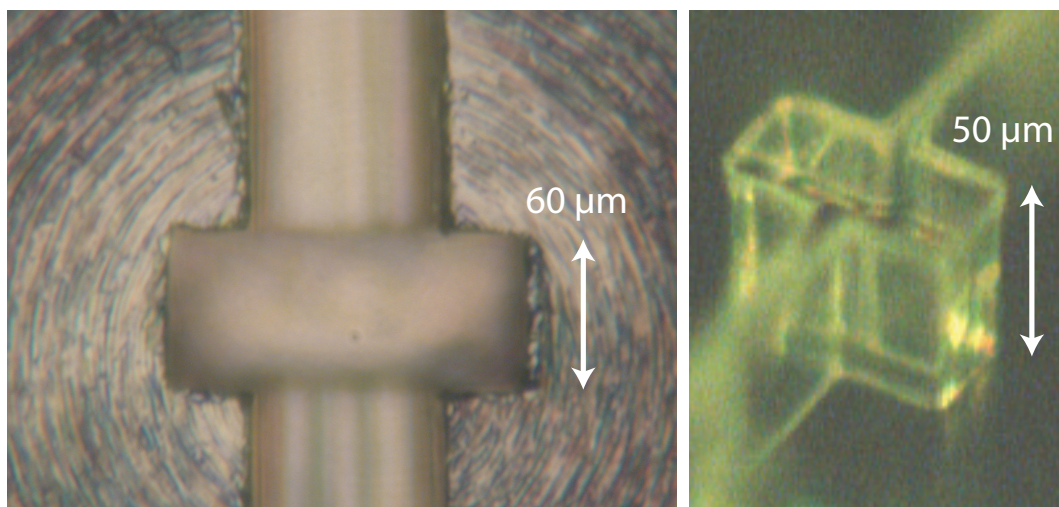


Figure 22: Left) 1.9 THz full height waveguide structure in a copper mixer block fabricated in the KOSMA workshop. Right) SU-8 resist prototype structure for THz waveguide mixers made in the KOSMA micro-structure laboratory.

half-height waveguides, as they are needed for diffusion cooled HEBs have only be fabricated up to 1.2 THz.

As second part of the structure, the substrate channel has to be diced perpendicular and centered through the RF waveguide. $60\ \mu\text{m}$ wide and $40\ \mu\text{m}$ deep channels have been diced which are used in the 1.9 THz mixer mounts. CST [64] simulations and scaled heterodyne measurements at 800 GHz indicate that this value is small enough for suspended substrate devices with thin membranes. For a dielectric filled substrate channel with a fused quartz substrate, the channel has to be 30-40 percent smaller. Hence this is another promoting point for the membrane concept.

In summary, complete 1.9 THz waveguide mounts for phonon cooled HEBs have been successfully fabricated (fig. 22, left). For the diffusion cooled HEBs which need half-height waveguides, 1.4 THz mixer mounts have been fabricated, but 1.9 THz mounts are not yet feasible. For developments above 2 THz we might have to consider alternate ways of production, as they will be discussed in the following sections.

7.4 Further approaches for THz waveguides

Recently thick photo resist SU-8 [65] has been developed. With its aid, micro structures with vertical sidewalls of several hundred microns can be fabricated. SU-8 can

be spun onto the wafer with a standard resist spinner in a thickness range from 2-2000 μm . The bake-out is a bit difficult because of the resist height, but an infrared (IR) oven has been developed as part of this work to meet this problem. The infrared radiation evaporates the resist solvent, whereby the resist is only heated gently and uniformly. A common mask-aligner with ultra-violet (UV) light is used for the exposure. After post-exposure bake and development, a resist structure remains with vertical ($\pm 1 \mu\text{m}$) sidewalls. The smoothness is in the nanometer range. These structures can be used as a negative mold for electro-forming of channels and cavities. SU-8 can be spun on and exposed in several layers, thus complex structures like a RF waveguide and a crossing substrate channel would be feasible. At KOSMA 20-100 μm high test structures for substrate channels and waveguides have been fabricated (fig. 22, right).

Inductively Coupled Plasma (ICP) etching can be used to produce high aspect ratio structures in Silicon. KOSMA has recently acquired an ICP etcher which will be used to fabricate THz waveguides.

7.5 2 THz waveguide antenna horns

The waveguide antenna horn transforms the free space wave mode into a waveguide mode. Two types of horns are in the focus of this work: the potter or dual-mode horn [66], which shows a good gaussivity of the beam pattern, but only for a narrow detection band, and the corrugated horn [67], which is significantly more broadband, but much more difficult to fabricate. This section focuses on the latter, because potter horns are commercially available up to several THz. The corrugated horn consists of up to one hundred concentric corrugations in the direction of the beam. These corrugations are in the order of 30 μm strong at 2 THz and have to be cut with rectangular sidewalls (fig. 23). Even for 800 GHz with 70 μm corrugations this is a difficult task. Here a negative aluminum mandrel is cut on a lathe, which is used as mold for electro-forming. After the electro-forming the mandrel is dissolved.

In the following two new technologies for the horn fabrication are described. The first technology (laser induced etching) is used by our cooperation partner, the University of Arizona, to fabricate horns for the 1.9 THz mixers, which are going to become part of the KOSMA contribution for the SOFIA airborne telescope. The second technology (laser 3D micro-lithography) has been presented by KOSMA as a new concept in [68] and has been evaluated by the University of Virginia and by Virginia Diodes, respectively [69].

In Laser Induced Etching (LIE) a silicon wafer is exposed to a laser beam in a chlorine gas mix environment. The etching gas can only dissolve the Silicon at the position of the laser spot. By moving position and speed of the spot, highly complex structures with different height can be "written" into the silicon [70]. The horn is made of two halves as such a silicon structure (fig. 23 right). The two silicon halves are metalized to make the inside conductive and are attached and aligned afterwards.

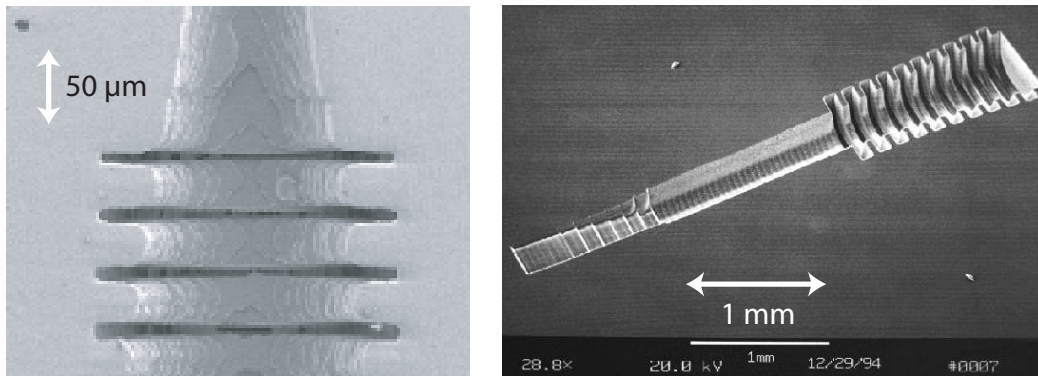


Figure 23: (Left) inverse corrugated horn structure, made with micro 3D stereo lithography by microTEC for the University of Virginia. (Right) One-half of a silicon corrugated horn structure, made with Laser Induced Etching at the University of Arizona. Two half are set together form a split-block horn.

In rapid prototyping, 3D laser lithography systems have become quite common. Here a liquid resin becomes hard, where three laser beams triangulate and heat up a certain spot within the resin. This system has been further improved by microTEC, Dortmund [71] to produce small structures with micro-meter resolution. First results have been achieved by the the University of Virginia [69] which can be seen in figure 23 left. It is not yet proven, though, that the necessary resolution for corrugated horn at 2 THz can be reached by this method. Structures with $15\ \mu\text{m}$ width have been produced, but the sidewalls are significantly rounded.

7.6 Summary and status

From the experiments, the following conclusions can be drawn:

In the frame of this work, the waveguide structures for 1.9 THz can still be fabricated in the KOSMA workshop with classic machinery and their self-developed tools. The corrugated horn for the planned 2 THz mixer will probably be fabricated by the University of Arizona with LIE. In parallel a potter horn is fabricated in at RPG, Meckenheim [72].

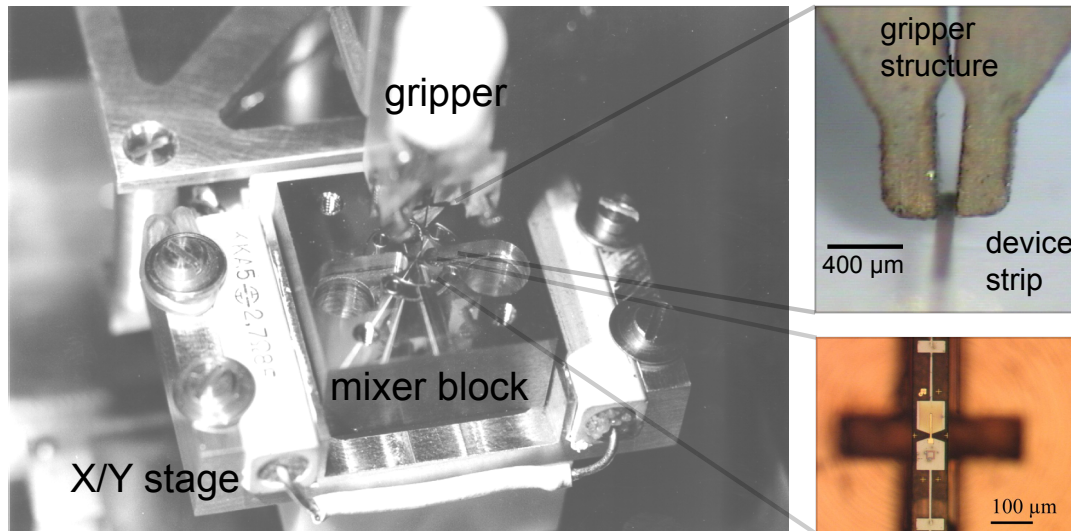


Figure 24: KOSMA Micro Assembly Station K-MAS with standard quartz devices

7.7 KOSMA Micro Assembly Stage for waveguide device mounting

At 800 GHz the fused quartz mixer substrates are $80\ \mu\text{m}$ by $35\ \mu\text{m}$ (width times height) and approximately $2\ 000\ \mu\text{m}$ long. The manual mounting and micrometer positioning of these devices into the substrate channel is rather difficult, and it is not very reproducible. For multi element (array) (AST/RO South Pole, KOSMA Gornergrat) and satellite (FIRST) applications a reliable and reproducible mounting procedure is of utmost importance. The requirements for the coming 1.9 THz receiver for the SOFIA-airplane will be even higher. Another point of concern is the sensitivity of some of the devices against electrostatic discharge.

These problems have been solved by the development of the KOSMA Micro Assembly Stage (K-MAS, fig.24), implementing a Klocke Nanotechnik microassembly stage [73]. The main problem is the gripping of the fragile device. The two fingers of the gripper are only $200\ \mu\text{m}$ by $300\ \mu\text{m}$ strong. Any standard stepper motor would bend and break these fingers or the device as soon as they try to grip it. The solution has been to implement piezo driven Nanomotors. A sliding clutch in every Nanomotor secures the safety of gripper and device, even when the gripper hits an obstacle full speed. The Nanomotors move the gripper in a volume of 2 by 2 by 1 cm with a resolution of a few nanometers.

Two Nanomotors are driving an x/y translation stage. It takes the mixer block together with its PID-controlled heater and the storage box for the devices. The heater serves to melt the thermoplastic glue (CrystalBond [55]) used to fix the substrate in the channel. Crystalbond becomes viscous at about 90°C, and solid after cooling down again. One Nanomotor© controls the z-movement of the gripper and another the gripper itself. The gripper is rotated by a standard dc-motor. An injection needle can be attached on the z-drive. This needle can be used to apply micron sized glue drops into the channels, to shift devices into position or to remove copper burrs and dirt from inside the channels. The system is run by keyboard or by a 5-axis control panel under control of a stereo microscope. To secure the safety of the handled mixers, the setup is thoroughly grounded. Even the extremely sensitive Hot Electron Bolometers have, thus, been mounted without loss.

In a first step of mounting the device, micrometer sized glue-drops are placed at controlled places of the substrate channel to secure reproducible mounting. Then the chosen device is taken out of its box by the gripper and positioned inside the substrate channel (fig.24, top right). By means of the Nanomotor-controlled needle the device can now be aligned totally plane and precisely centered in the waveguide (fig.24, bottom right). The precision is only limited by the resolution of the microscope. When the glue has hardened, the mixerblock is ready for bonding the electrical connections.

With this step the fabrication of the waveguide environment and the assembly of the device is finished. In the following chapter, the development and fabrication process of the HEB devices is summarized. It has been taken out of the chronology, because the devices are not the focus of this work.

8 HEB mixer development and fabrication

In the previous chapters the fabrication concept for freestanding membranes for HEB mixers has been presented. In this chapter the development and fabrication of the corresponding membrane HEB devices is discussed. Due to the different geometry and high frequency properties of the waveguide system compared to the fused quartz substrate design, the RF and IF structures have to be redesigned.

8.1 RF design simulation and development with CST

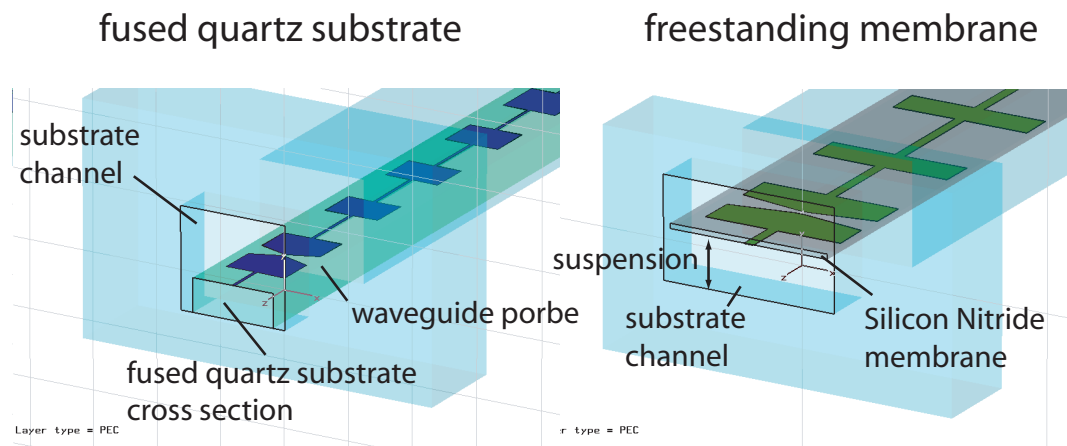


Figure 25: Cross section of dielectric filled substrate channel (old design) and suspended membrane substrate

The waveguide probes, which are needed to couple the signal to the HEB, and the micro-strip IF filters have to be adapted to the membrane technology. The impedance of the filter elements and the probes strongly depends on the dielectric properties of the substrate. The fused quartz substrates with a dielectric constant $\epsilon_{\text{quartz}} = 3.8$ are about $30 \mu\text{m}$ thick and glued directly onto the substrate channel ground. The freestanding membrane substrate is made of $2 \mu\text{m}$ thick Silicon Nitride with $\epsilon_{\text{Silicon Nitride}} = 7.5$. The suspended design additionally changes the micro-strip impedances. In the context of this work, a commercial 3D e/m simulation program CST [64] has been used to adapt and optimize the micro-strip structures for D-HEB membrane mixer devices. The optimization for P-HEB devices was done by T. Tils [74].

In general it is rather difficult to match diffusion cooled HEBs of about 20 Ohm to waveguide probes, because the waveguide impedance is several hundred Ohm. The

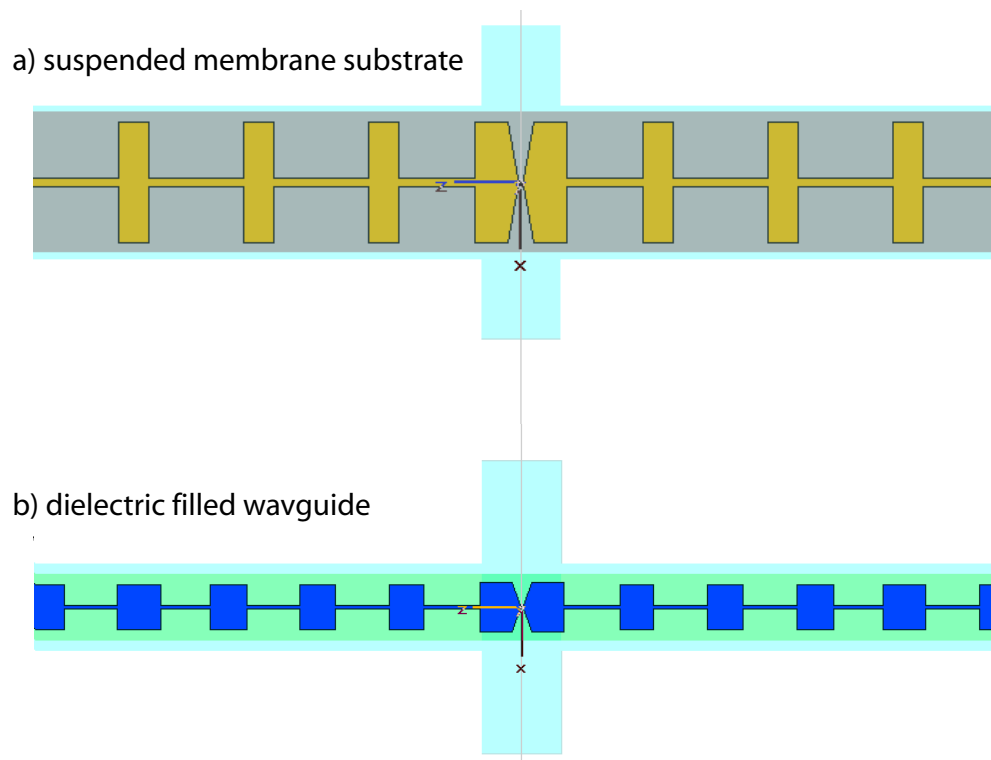


Figure 26: a) New micro-strip filter and probe design for suspended substrate membrane D-HEB mixers. b) 800 GHz design for solid fused quartz substrates.

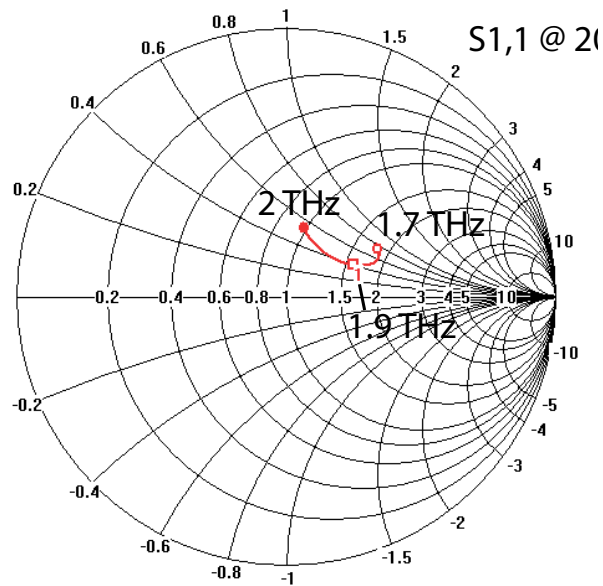


Figure 27: Smith chart of the suspended substrate membrane filter design for 20 Ohm D-HEBs.

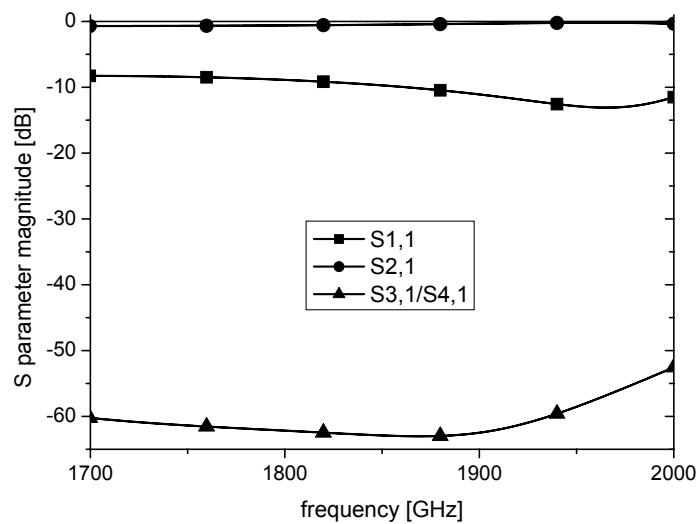


Figure 28: S parameter magnitude of the suspended substrate membrane filter design for 20 Ohm D-HEBs. S1 is the load at the waveguide probe, S2 is the waveguide port and S3/S4 are the bondpad ends of the IF filters.

Smith chart of the new waveguide probe design for D-HEB membrane mixers can be seen in figure 27. It visualizes the impedance of the waveguide normalized to 20 Ohm HEB resistance. For the goal frequency of 1.7-2 THz the matching is good, but further improvement would be interesting. The RF blocking at the IF filters (S3,1/S4,1) is better than -50 dB, which is more than sufficient (fig. 28). The reflection of the RF signal at the waveguide probe is in the range of -9 to -11 dB (S1,1). A smaller value would be preferable, but here the small HEB impedance makes further improvements difficult. The reflection losses are still below 1 dB. For phonon cooled HEBs with about 100 Ohm impedance the matching is significantly easier.

The IF filter and the substrate channel have to be designed in a way that the RF is blocked from leaking into the channel. The maximum blocked frequency and the filter design depends on the width and the dielectric filling of the substrate channel. CST has been used to determine the maximum substrate channel width with sufficient blocking of the RF by -50dB. A dielectric filled channel for a 1.9 THz mixer must not be wider than 40 μm , while the suspended substrate channel can be designed 70 μm wide. The latter can be fabricated at the KOSMA work shop. Figure 26 a shows the new membran micro-strip filters and waveguide probes. Comparing this design to the fused quartz design (b) the membrane and the micro-strip lines are significantly wider. A scaled 800 GHz version of the new suspended membrane filter has been tested with an HEB as direct detector and a Fourier Transform Spectrometer to test the predictions of the simulations (see chapter 10.4).

8.2 Fabrication of HEB mixers on Si_3N_4 membranes

This chapter gives a brief summary of the fabrication of the diffusion cooled HEB devices for the membrane processes. The fabrication of the phonon cooled HEBs can be found in [36], [60]. With both types of devices, membrane waveguide mixers have been successfully realized. The base material have been silicon wafers with a 2 μm thick Si_3N_4 membrane layer.

In a first step, alignment crosses for the later Electron Beam Lithography (EBL) are applied onto the bare Si_3N_4 membrane of the base wafer. They consist of 150 nm Nb and 40 nm Au. The crosses are structured with Ultra-Violet Lithography (UV-Litho) and photo resist lift-off. In the next step the 12 nm thick Nb film is sputtered, which will be structured into HEB micro-bridges later. So this process step is crucial in terms of cleanliness and reproducibility. Before the film is sputtered, the wafer is cleaned with oxygen plasma in the load-lock of the sputtering chamber. Then the Nb film is sputtered in the main chamber. On top of the 12 nm Nb film, a 15 nm of gold film is sputtered in-situ as protection for the Nb and as contact layer for the heat-sinks, which are applied later (fig. 29).

Now the wafer can be taken out of the chamber to apply the heat sinks for the HEBs. The heat sink structures are written into PMMA resist with an Electron Beam Lithog-

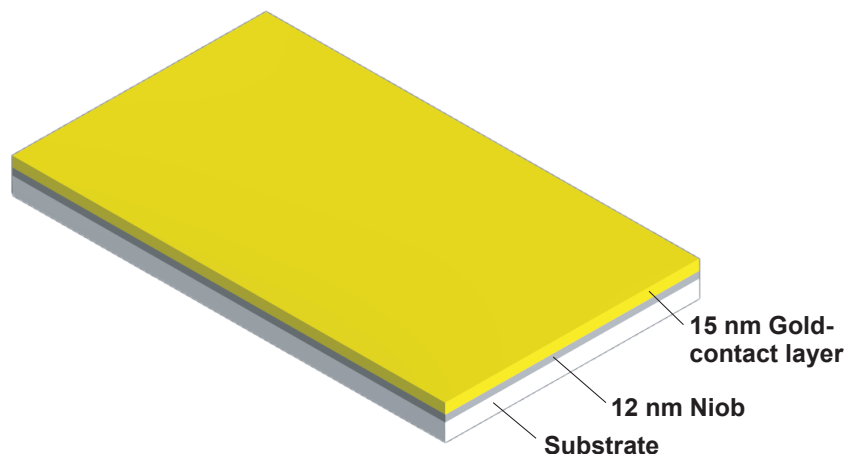


Figure 29: In-situ sputtering of 12 nm Niobium and 15 nm Au contact layer.

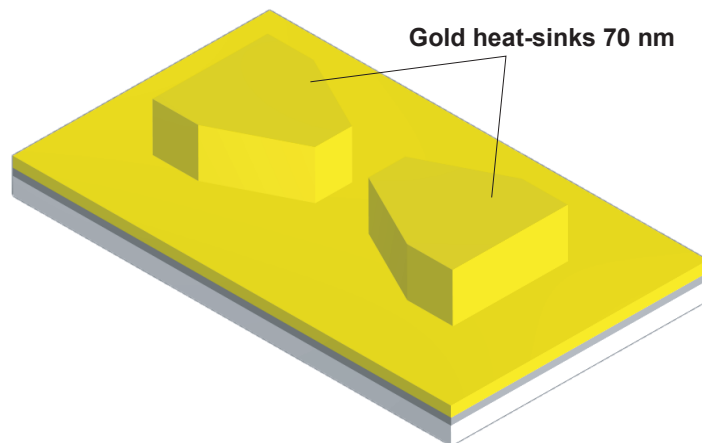


Figure 30: Deposition of 70 nm thick Au heat-sinks on the Nb/Au bi-layer.

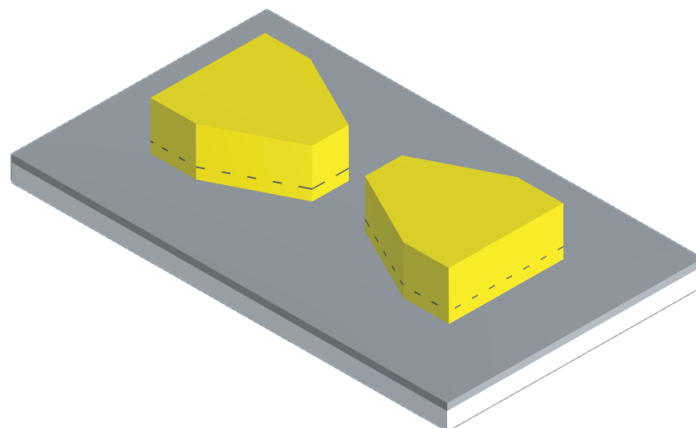


Figure 31: Removing of the Au contact layer via Ar RIE etch step.

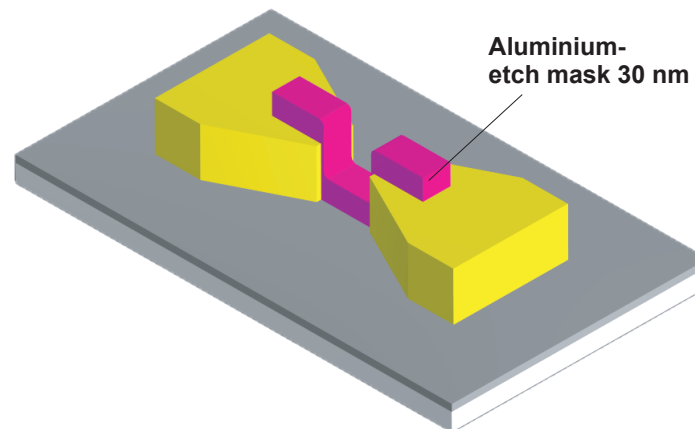


Figure 32: Sputter deposition and lift-off structuring of 10 nm thick Al strips. These are used as etch mask for the following bridge structuring.

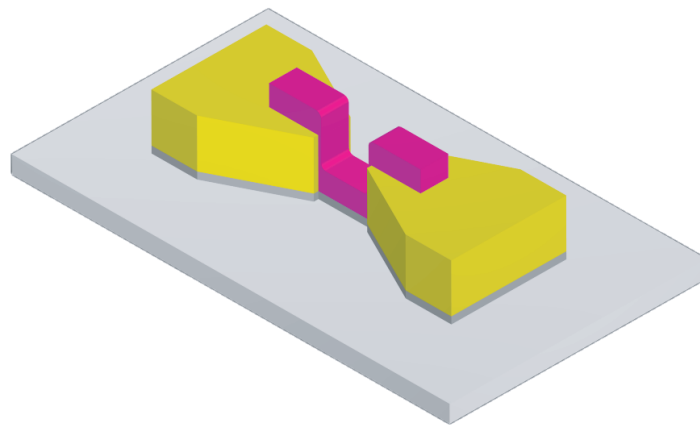


Figure 33: Dry reactive ion etching of the HEB bridge structure.

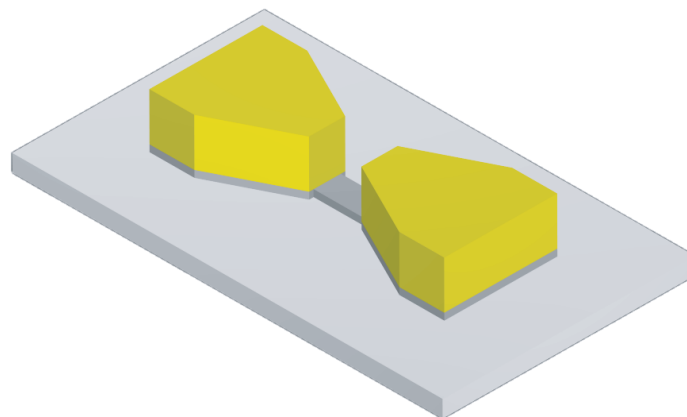


Figure 34: Removing of the Al etch mask.

raphy system. They are made of 70 nm thick gold, which is thermally evaporated onto the structured resist. Then the resist is dissolved, leaving the heat sink structures after this lift-off process (fig. 30).

The interface transparency between the Nb HEB film and the heat sinks is of utmost importance for the *diffusion cooled* HEBs. In this process we can expect a very high transparency, because the gold protection layer is used as contact layer for the heat sinks. It prevents oxidation of the Nb film, when it is taken out of the vacuum of the process chamber.

The RF waveguide probes, IF filters and bondpads are applied in one step before the HEBs are structured. 300 nm gold with a 80 nm Nb adhesion layer is sputtered into a UV lithographed resist mask for lift-off. The Nb layer also serves for the elimination of the DC series resistances. Hence the superconducting properties of the device itself can be distinguished in the DC characterization.

Finally the HEBs are structured. First the gold protection layer is removed by physical etching with Ar. This is done in the chamber of the Reactive Ion Etching (RIE) system (fig. 31). Then PMMA resist is applied and structured with EBL. It is used to pattern a 10 nm Al etch mask with lift-off. A RIE step with a mixture of SF_6 and CHF_3 removes the Nb film while sparing the Nb micro-bridges between heat sinks. Here the SF_6 provides the necessary F ions and radicals for the etching, while the CHF_3 passivates the sides of the etch mask to prevent under-etching.

At this point the HEB devices are finished. Before they are DC tested the membrane structuring is done as described in ch. 6.

9 DC measurements - Setup development and device characterization

The first step in the characterization of the finished HEB devices, before they are mounted into the mixer blocks, is to characterize them through a series of DC measurements at 4.2 K. These measurements take place in a dipstick, a measuring probe which can be dipped into a standard LHe transport dewar. As mentioned in chapter 6.6 the devices are still on the bulk support wafer so the handling is very comfortable. For HEBs characterization, current versus voltage (I/V) (ch. 9.1) and the resistance versus temperature (R/T) (ch. 9.3) curves are needed to determine the important parameters, which allow conclusions about the quality of the device for heterodyne use, and about the fabrication process.

In this context several PC-linked measurement systems have been built. A computer controlled measurement setup for R/T measurements has been successfully developed. The manual I/V setup has been upgraded to a computer controlled setup, with fitting routines which automatically determine the important characteristic parameters of HEB (and SIS) devices. All determined parameters and characteristic curves are also automatically filed into a central database (Appendix C) and linked to the process parameters. Integrated into the measurement programs are data base browsers, providing a direct access to the already acquired data for further comparisons. The whole system has been developed inside this work but has also been extended for the SIS device characterization. It has shown benefits for the development and quality management of other projects like the ESA Herschel satellite. Especially the quality assurance, demanded for the Herschel project, showed the necessity for precise documentation of these parameters.

9.1 Current vs. Voltage curves measurement setup

The complex dependence of the size of the hot spot in the center of the bolometer bridge on the various bias conditions is indicated in chapter 4.4.3. One of the ways of characterizing the actual bolometer is the measurement of the DC current versus voltage I/V curve. The I/V curve allows conclusions about the nature of the hot spot and the *self-heating* of the HEB (ch. 4.5). Note that $dR/dT = dU/(dIdT)$. The resistance of the HEB in the normal conducting state at high bias currents is an important parameter that determines the RF matching to the waveguide probe.

For the measurements, about 30 devices are bonded and cooled down on shuttle carrier inside the dip stick. One device after the other is selectively connected to the bias supply box via a switch at the head of the dipstick. The bias supply box provides a very small oscillating bias current for the device and amplifies the returning voltage.

The characteristics of the HEBs can vary for more than one order of magnitude, depending on the concept and the design. Therefore the settings of the bias supply and the instrumentation amplifiers are adapted to each HEB measurement by an iterative autorange routine. A data acquisition cycle is started by rising the amplitude of the bias current oscillation from zero until its maximum exceeds the critical current of the HEB. With these oscillations the HEB switches between the normal conducting and the superconducting state showing a hysteresis between $I_{critical}$ and the current where the hot spot disappears ("I hyst"). After optimizing the gain settings of the current and voltage AD converters for a good signal to noise ratio, the data acquisition can be started by the operator. The data of 8 cycles of the bias current oscillator are sampled and written into different data objects, sorted to certain areas in the characteristic curves. Of course the sorting parameters depend on the characteristics of every HEB. A special algorithm combines the data of the autorange function with the sorting parameters to reduce the risk of misinterpretation. The sorted data is processed further to calculate the normal resistance (RN), the critical and the hysteretic current, and the ratio of both currents. These are displayed together with the I/V plot on the program screen (see figure 35).

The program can read the HEB dimensions from the central data base (App. C) to calculate the sheet resistance of the bolometer film. Finally the whole set of device parameters is filed into the data base. A data base browser, integrated into the control screen, enables the direct comparison of the measured devices. The data base entries can be double-clicked to show the corresponding I/V plots as a link to the I/V file is automatically added to each entry. The number of points written to this file is reduced with the knowledge about the important parameters, so a very high ratio of data compression can be reached with a minimum of loss in data. An additional program can be used to gather the dI/dU derivative through optimized sorting and interpolation routines. The development of a hot spot inside the HEB is changing the slope of the I/V curve and can therefore be visualized in the derivative.

9.2 Interpretation and discussion of I/V measurements

A current-versus-voltage characteristic of a typical device is shown in figure 36. The curve is point symmetric, hence only the positive quadrant will be discussed. This quadrant can be divided into three parts: First a superconducting part, where the voltage drop is zero across the device for currents below the critical current $|I| < I_c$. Here the gradient dI/dU is infinite. Second a non-linear resistive region with a significant hysteresis. And third a linear or normal conducting region at higher bias voltages. Note that exceeding the critical current does not mean, that the linear part of the I/V curve has been reached. In some devices the curve is non-linear for currents up to $2 * I_c$.

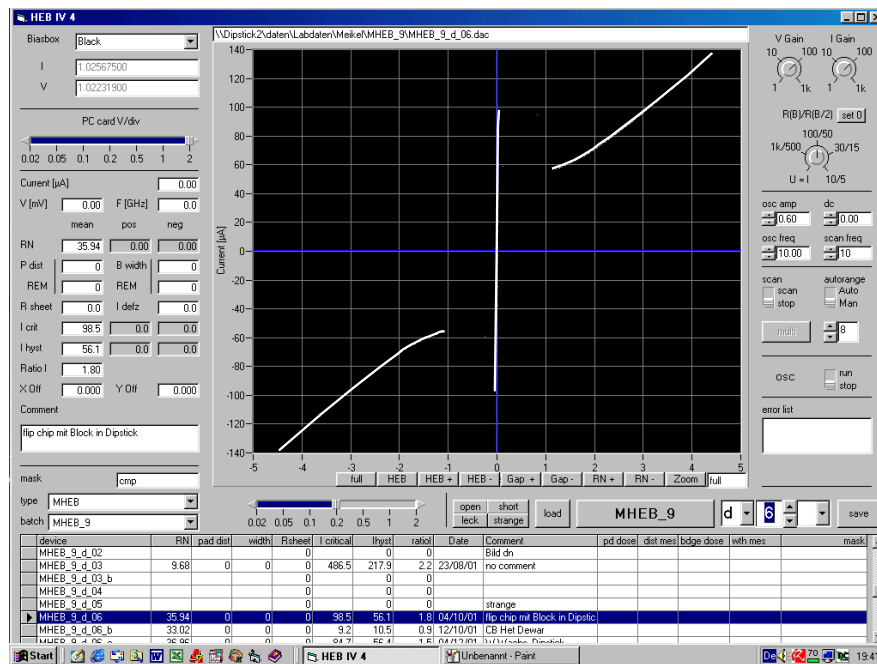


Figure 35: Screen shot of the HEB-IV-4 program with a characteristic Current vs. Voltage curve of a HEB

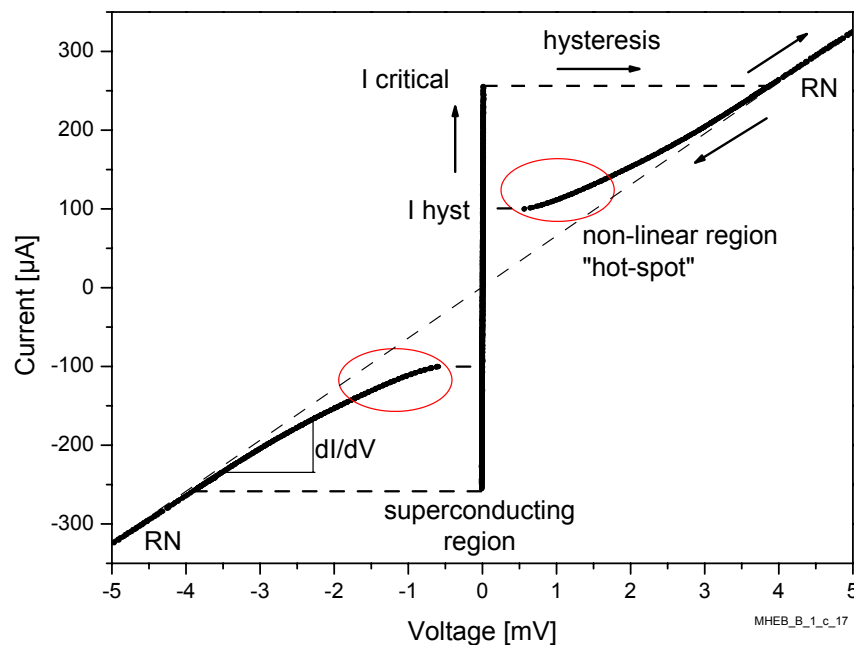


Figure 36: Current-versus-voltage curve of a diffusion cooled bolometer made on silicon nitride, measured in liquid Helium in a dipstick. There are no differences to be seen to devices fabricated on fused quartz.

Between the superconducting region and the normal conducting bias region, there is a significant discontinuity in the curve. A switching from the superconducting state directly to a resistive state with no intermediate voltage values is observed, when the critical current is exceeded. It can be assumed that a large part of the bridge turns normal conducting, when the critical current is exceeded only in a small region with the smallest I_c . Then this part would dissipate power which slightly heats the rest of the bridge. With the rise in temperature the critical current decreases in this region and consequently a larger part would turn normal conducting and would also dissipate power. In a simple model this self-heating effect would heat up the whole HEB bridge above T_c . A more detailed description of self-heating in superconductors can be found in [75] and [76].

At bias currents between 2 times and 3 times the value of I_c , well outside the non-linear region, the normal conducting resistance RN is fitted to the curve. To date it is assumed that HEB impedance and RN of the HEB are of similar value. Hence the RN value is used to design and to simulate the RF matching between HEB and waveguide probes (ch. 8.1).

Subsequently the bias voltage is reduced and plotted against the bias current. Even at bias currents much smaller than I_{crit} the bridge does not turn superconducting again, instead it is showing a hysteretic behavior. The ends of the bridge being cooled best through the heat sinks, turn superconducting in this biasing range, but at the center of the bridge a normal conducting hot-spot remains (hot-spot model). The *self-heating* power, dissipated in this hot spot area by the bias current, is high enough to keep it normal conducting (ch. 4.5). In contrast to the ends of the bridge, the heat cannot be transferred so fast from the center to the heat sinks.

When the bias voltage and the related power dissipation is decreased the hot spot shrinks in size, reducing the overall resistance of the bridge. A change in resistance again changes the power dissipation (ch. 4.5). The interdependence of hot-spot size and electrical power dissipation is called *electro/thermal feedback* and is seen in the nonlinear upwards bending of the curve towards small bias voltages. Hence the current-to-voltage derivative dI/dU can be used as indicator for the hot spot development and behavior. The electro-thermal feedback can be so strong, that we see a negative differential resistance. Below a certain bias voltage a second discontinuity is seen in the curve, when the bias switches to the superconducting region. This switch can be explained with a disappearance of the hot-spot, when the *self-heating* is not sufficient to sustain the hot-spot and the whole bridge turns superconducting. The smallest current still sustaining a hot spot is called I_{hyst} . With a RN of 16.49Ω and a critical current of $255 \mu A$ the shown device MHEB_B_1_c_17 is not different from other devices made on fused quartz. Overall there were hardly any differences to be seen in the I/V curves of the silicon nitride based devices compared with the ones on fused quartz.

9.3 Resistance-vs-Temperature measurement setup

9.3.1 Measurement principle

For the development of the superconducting thin films the knowledge about the critical temperature and sheet resistance is essential. These parameters are used for quantitative statements about film quality and its RF properties to optimize the many process parameters involved with the film sputtering. For the development of HEBs, as their response is directly connected to thermal effects, its resistance-versus-temperature curve is of even higher importance for the characterization. But there are a couple of points which make the measurement conditions very difficult in this case. As seen in the previous chapter the bias currents have a heating effect on the bolometer. Therefore the R/T curve depends on the current used to measure the resistance. On the other hand, this information can be used to calculate the electrical power needed to heat up the bridge and its thermal conductivity. Normally these measurements are done at bias currents of 1, 10 and 20 μA . With 1 μA and a device resistance of, for example, 10 Ohm the maximum voltage returned is 10 μV . This explains the need for an extremely low-noise high-resolution measurement setup with the capability of switchable measurement currents. As early setups had shown, the subtraction of offsets is another point of concern.

9.3.2 R/T measurement setup realization

In the context of this work, a R/T scan setup was developed and successfully implemented into the characterization process, using Lock-In-Amplifiers (LIA) to eliminate noise. It will be referred to as the RT-box. In principle a user selectable current is applied at two probes on the sample, causing a voltage drop over the sample. Two other probes are used to pick up the voltage proportional to the sample resistance. Synchronously the temperature at the sample is monitored and logged together with the measured resistance.

Two LIAs are needed to measure current and voltage separately and to calculate the resistance of the sample. An oscillating bias current I_{bias} with square waveform is generated and applied to the HEB. Hence the biasing switches between $+I_{bias}$ and $-I_{bias}$. The HEB is bidirectional, so this change in current direction should not have influence on the HEB characteristic. If the HEB would be biased with a sinusoidal waveform, as it is sometimes done in similar applications, the bias conditions would change continuously. In this case a signal, which has been averaged over different bias conditions, would be measured. The voltage drop at the HEB $U_1 = I_{bias}R_{sample}$ and at a reference resistor $U_2 = I_{bias}R_{ref}$ is amplified with the two LIAs, as seen in figure 37.

The used LIAs provide a differential input which filters noise signals induced into the connecting cables between the dipstick and the LIA. The Lock-In-Amplifier itself

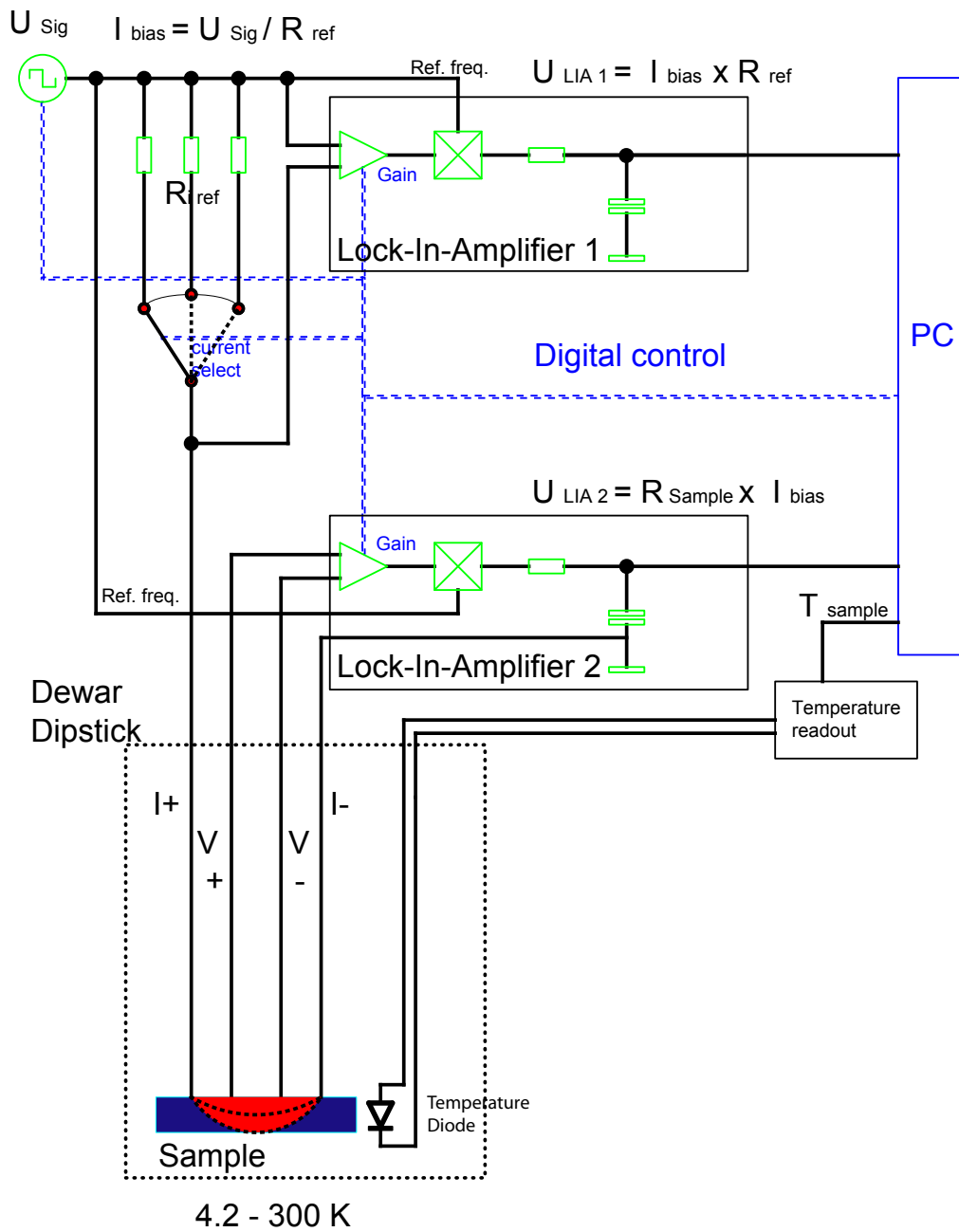


Figure 37: Schematic circuit of R/T measurement setup

only amplifies signals which have the same frequency and phase as the locked reference signal, in this case the mentioned oscillator. This allows to measure μV signals with nano-Volt resolution even when the computers in the vicinity apply noise in the milli-Volt range. This leads to a resolution in resistance of 20 mOhm which can resolve tiny resistance variation like the ones caused by proximity effects, or as it is needed for Van der Pauw measurements (sec. 9.3.4). Different measurement currents can be selected between 0.1 and 500 μA to measure sensitive devices or to characterize superconducting films. The temperature is measured with a calibrated [77] diode. The conversion of the voltage at the diode into the corresponding temperature is done in the PC with the matching calibration table. The whole system is remote controlled by the PC. During the actual scanning the digital communication of PC and RT-box is halted to prevent crosstalk of digital pulses into the analogue lines. The PC system provides a comfortable user interface and automatically sets the gains of the different LIAs and pre-amplifiers to the optimum ranges.

These units are mounted into a 19" rack with backside bus system for electric connections, together with various adapter cards to connect the R/T measurement system with the different dip-sticks or dewars. The latter can be easily exchanged or altered enabling a very flexible adaptation of the system to different tasks.

9.3.3 Performing the measurements

After the operator has selected a measurement current at the RT-box program (see fig. 38), the system is switched to this value on the hardware side. The voltage at the reference resistor is roughly known so the according LIA gain can be set directly. The gain setting for the LIA amplifying the signal at the HEB, is more complex as it switches between zero and $U = I \cdot RN_{HEB}$. Changing the gain setting of the LIA during measurements needs time until the LIA shows again a stable signal. This can lead to invalid data points. Hence the gain of the LIAs is set according to the maximum expected signal levels of the scan and locked. Commonly the maximum signal levels can be expected, when the HEB or the thin film is in normal conducting state. The signal is amplified before it is digitalized. The gain setting of this post LIA amplifier can be switched fast and is therefore used to automatically adapt the setup to the measurement conditions. Additionally the output of the LIA is displayed on the control screen for continuous surveillance. Of course the system can be run manually or automatically as preferred. To run a temperature scan the dip-stick is slowly drawn out of the liquid Helium and warms up while temperature and resistance are monitored and written into a file. As in the I/V setup, the important data is filed into the central data base together with the link to the R/T data file. An integrated data base browser can also handle and display the data and I/V curves of previously measurements to allow an online comparison (see fig. 38).

9.3.4 Van der Pauw measurements of sheet resistance

Another feature of the setup is the capability to determine the sheet resistance of thin films with the Van der Pauw method [78]. The sample film is structured into squares with four probes at the corners, which are used to measure the resistance R_1 and R_2 in two orthogonal directions. With the formula

$$R_{sheet} = \frac{\pi}{\ln 2((R_1 + R_2)/2)} \quad (55)$$

the sheet resistance can be calculated for a known thickness. The sheet resistances are rather small, for example 70-200 $\mu\Omega\text{cm}$ of NbTiN at 20 K or about 4 $\mu\Omega\text{cm}$ for Aluminium. The ability of the system to resolve these sheet resistances with $\mu\Omega\text{cm}$ resolution shows the power of the setup (fig. 39). The sheet resistance itself is a very important indicator for the film quality itself and for its RF properties, and it is therefore absolutely essential for the development of component superconductors. High performance NbTiN films have been developed with the help of this system for phonon cooled HEBs [36], [11] and for the Herschel Satellite band 2 SIS mixers [15].

9.4 Interpretation and discussion of R/T measurements

Figure 40 shows a typical R/T curve with two steps in the resistance. Starting at 7 K on the right hand side, the first drop in resistance occurs at what we interpret to be $T_{c_{bridge}}$, when the bridge becomes superconducting. This change in resistance is used for the heterodyne mixing as explained in chapter 4 and so the steepness of the slope ($\Delta T_{c_{bridge}}$) is an important parameter for the device characterization. The resistance value of the plateau above $T_{c_{bridge}}$ corresponds to the normal resistance of the bolometer. Measurements of $T_{c_{bridge}}$ at different bias conditions can reveal information about the cooling mechanisms of the bolometer.

At $T_{c_{bridge}}$ the step does not drop to zero resistance but remains on a second plateau as the ends of the bridge remain normal conducting at lower temperatures. The resistance of this part of the bridge drops to zero at a temperature about 1 K lower. The hypothesis is, that the T_c of the outer ends of the bridge is reduced due to the proximity effect of the adjacent Au heat sinks. In bi-layers consisting of a thin superconductor and a thicker normal conductor, reduction of the T_c in the superconductor is observed [79]. This temperature step will be referred to as the *proximity step* with the critical temperature $T_{c_{proximity step}}$ and the slope $\Delta T_{c_{proximity step}}$. The temperature difference at this second plateau between $T_{c_{bridge}}$ and $T_{c_{proximity step}}$ can be interpreted as an indicator for the quality of the Nb/Au interface as described by [30]. The interface transparency is important for diffusion cooling [30], [23].

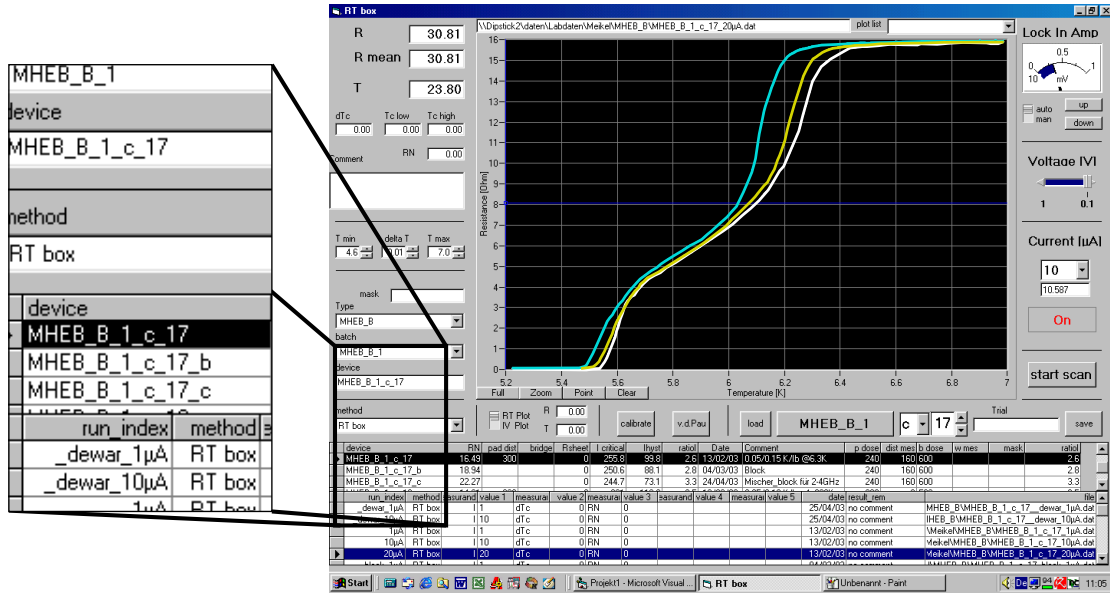


Figure 38: Screen shot of RT-box-1 program with characteristic R/T curve of a D-HEB

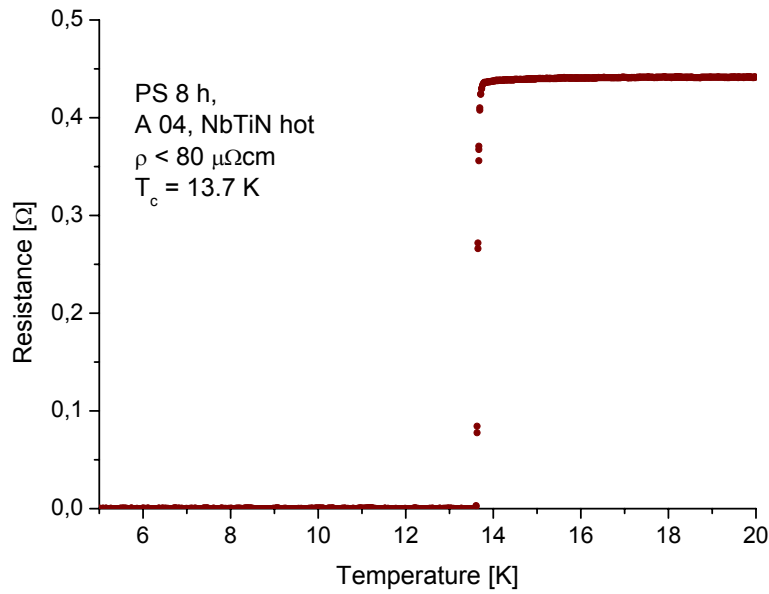


Figure 39: Van der Pauw measurement of a NbTiN film.

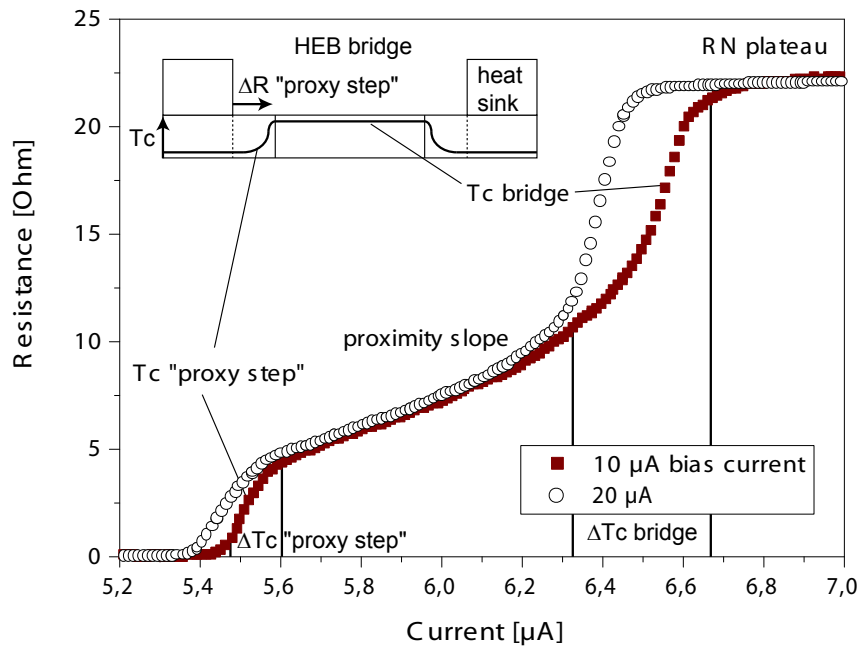


Figure 40: R vs T curve of a HEB made on a silicon nitride membrane

9.5 DC measurements interpretation

This section tries to interpret the measured DC data of various produced D-HEBs, which have been produced on membranes. The data of HEBs, which have shown good heterodyne response, and of devices which have not, are compared. The data are also compared with the data of HEBs made on other substrate material to investigate the influence.

9.5.1 Comparison of different devices

Figure 41 compares the R/T curves of bolometers of the same batch with different bridge length measured with 1 and 20 μA bias currents, respectively. Looking at the curve of the 170 nm long bolometer b_06, the T_c of the bridge is clearly reduced by 0.16 K for 20 μA bias current, due to the additional electrical heating effect. For shorter bolometers this heating effect is less. In a simple model calculation, this shift in the critical temperature can be used to make first estimations about the cooling characteristics, and therefore possibly the IF bandwidth. The temperature dependence of the thermal conductivity and the reduction of the critical temperature by the magnetic field of the bias current are neglected in this approximation.

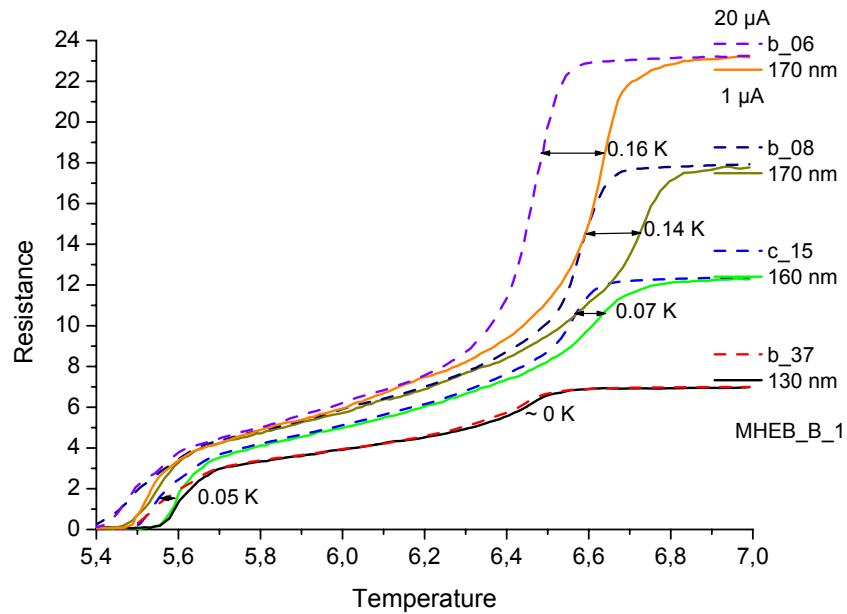


Figure 41: R/T curves of HEBs with different bridge lengths measured with 1 and 20 μA bias current respectively. The T_c of the bridge decreases with larger bias currents due to the additional electrical heating effect. Delta T_c decreases with bridge length.

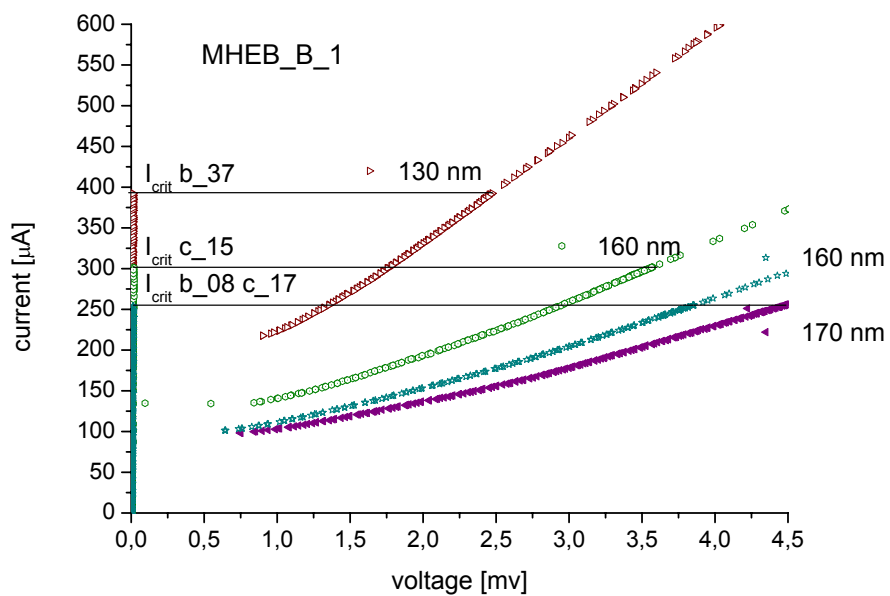


Figure 42: I/V characteristic curves of different devices from the same batch (same device as above).

MHEB_B_1 device	bridge length [nm]	therm. cond. G [nW/K]	time const. τ [ps]	expected bandwidth [GHz]
b_06	170	60	37	5.8
b_08	170	50	35	4.5
c_15	160	70	21	7.5
b_37	130	inf	0	?

Table 3: Thermal conductivity of different devices, estimated from the shift in the R/T curves with different bias currents (fig. 41).

Calculating the difference in dissipated DC power ΔP :

$$(I_1^2 - I_2^2)R = \Delta P \quad (56)$$

and relating it to the change in $T_{c1} - T_{c2}$ allows a rough estimation of the thermal conductivity G of the bridge:

$$G = \Delta P / \Delta T = \frac{(I_1^2 - I_2^2)R}{T_{c1} - T_{c2}} \quad (57)$$

In table 3 the thermal conductivities of the shown curves are listed together with an estimation of the time constant τ which is gained by dividing the thermal capacity of the bridge through the conductivity. The thermal capacity can be estimated from the volume V_{bridge} of the bridge with:

$$c = \gamma\theta V_{bridge} \quad (58)$$

Here θ is the electron temperature and γ is the Sommerfeld constant, which is about 700 J/Km^3 for Niobium [20]. It is difficult to measure the bridge width in the scanning electron microscope (SEM), because the bridge film is very thin. The visible contrast is extremely poor and there is the risk to damage the bridge with the electron beam and charge pick-up. The bridge length is defined by the heat sinks and can therefore be measured before the bridge is structured. The bridge width is estimated from RN in relation to the length of the bridge. The 170 nm long device b_06 for example seems to be considerably thinner than the others as it has a higher resistance than another device with the same length (b_08) and also shows a reduced Tc which can indicate a thin or even damaged bridge.

The shift of Tc with the bias current for bolometers is clearly reduced from about 0.15 K for 170 nm over 0.07 K for 160 nm to nearly zero for the 130 nm long one. The decrease corresponds to the increase of G from 50 nW/K to nearly infinity.

The properties of Tc and ΔT_c of the bridge largely depend, as expected, on the bridge geometries. The properties of a second *proximity step* should be device independent,

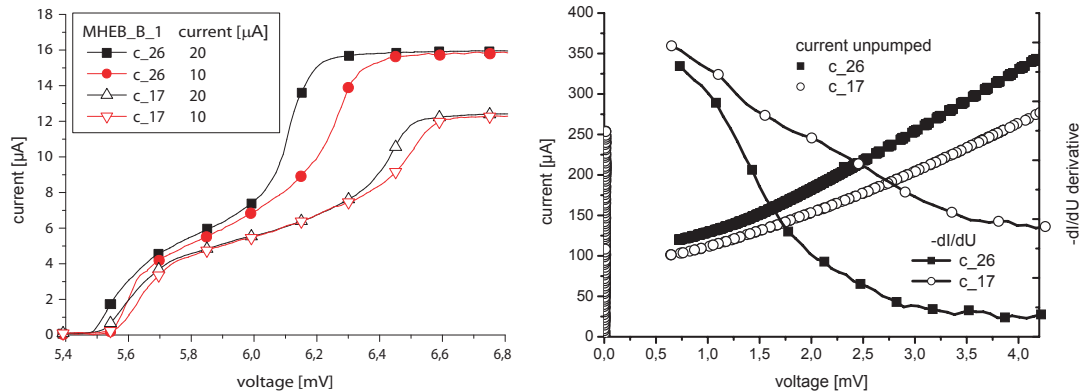


Figure 43: R/T, I/V and $-dI/dU$ characteristic curves of a working (c_17) and a non-working (c_26) devices from the same batch.

as they are related to the properties of the film and its interface to the heat sinks. The plateau presumably caused by the proximity effect, has not only the same level of resistance for all devices but also has the same T_c within a range of ± 0.05 K. This indicates the uniformity and quality of the heat sink interfaces as referred to by Stodolka [30]. The T_c of the proximity step shows a slight smearing and dependence on the bias current of 0.05 K which is acceptable.

In figure 42 I/V measurements of the devices, which have been characterized in the R/T measurements in figure 42, have been plotted. The curves of devices with a smaller RN show steeper I/V gradient and larger critical current. Otherwise they look similar. Still there are tiny variations in the gradients of the slopes which might be related to the hot-spot dynamics. In chapter 11 it is tried to further investigate details of the I/V curves on the basis of complex model calculations.

The presented devices have been chosen from batch MHEB_B_1 which has provided successful mixers like c_17. Except device b_37 all of them would be promising candidates for heterodyne measurements, but only a heterodyne measurement can tell, if these can really be used for heterodyne mixing. In figure 43 the R/T and I/V characteristics of a working (c_17) and a non-working device (c_26) from the same batch are plotted, to give an example, how small the differences in the DC characteristics are. In the R/T plot the working device (c_17) has a slightly lower bridge T_c which shows a slightly larger bias current dependence, than the non-working device (c_26). This might be the result of better cooling in device c_26. Otherwise there are no obvious differences which could be used for reliable prediction about the performance of the device. The I/V curves (right) do not show significant differences, either. The $-dI/dU$ derivative has been added to enhance and visualize tiny differences. Here we can see slight variations. In chapter 11 it is tried to model these variations in order to

find connections between the variations and the mixing process. At the current point of research we cannot make a reliable distinction between the two devices from the DC measurement data. The differences between different batches are sometimes more significant. Hence in the following paragraph the devices of a failed production are presented to visualize the differences.

9.5.2 Comparison of different batches in membrane technology

This chapter discusses the DC characteristics of the devices of batch MHEB_15 in comparison to the devices of MHEB_B_1 which has been discussed in the previous paragraph. The devices of batch MHEB_15 which have been measured showed a high sensitivity for direct detection and LO-power, but in all of these measurements no heterodyne response has been observed. Looking at the unpumped I/V characteristic of MHEB_15_d_64 (fig. 44, left), the non-linear region only spans a very small bias voltage region from 1.2 to 1.7 mV. Device c_17 from the other batch shows non-linearities from 0.5 to 3.5 mV. If LO-power is applied (fig. 44, right) the differences between the curves become more significant. The critical current of device c_17 is reduced to $40 \mu\text{A}$, but otherwise the characteristics of the curve are not significantly changed. A superconducting and a large non-linear region can be observed. The pumped curve of device d_64 is different. No superconductivity is measured, even at very low bias voltages. Instead we find a resistive curve starting at 0 V. In the following this region will be referred to as the *sub-hysteretic region*. At about $40 \mu\text{A}$ we find a critical current and a hysteretic voltage relation. The small non-linear range which we have seen without LO power has nearly disappeared. This non-linear region is normally used for biasing for heterodyne mixing. In the case presented here this bias region around 0.4 V is too small for stable biasing. Also the observed *self-heating* seems to be rather small.

A biasing in the 0.2 V region, where e.g. device c_17 would be biased, did not allow heterodyne detection, either. At 0.2 mV device d_64 would be biased in the resistive part of the *sub-hysteresis region*. This observation has led to the assumption, that the resistive *sub-hysteresis region* has influence on the mixing process.

In communication with Harald Merkel [80], a hypothesis to explain the origin of this curve has been developed. It assumes the development of hot-spots near or at the heat-sinks, where the T_c is reduced due to the proximity effect. Maybe even two hot-spots develop, one on each side of the bridge. The hypothesis is based on several observations. Looking closely at the I/V curve in the *sub-hysteresis region*, a slightly non-linear relation to the bias voltage can be observed. This is a strong indicator for a thermal effect, maybe a hot-spot. We cannot measure a superconducting bridge, even at low bias voltages. Hence at least part of the bridge is normal conducting in absence of a bias current. It is not likely the whole bridge, because then we would not see a hysteresis at higher bias voltages. It is also not likely that the center of the bridge is normal conducting. A hot-spot in the center would show the hysteretic behavior,

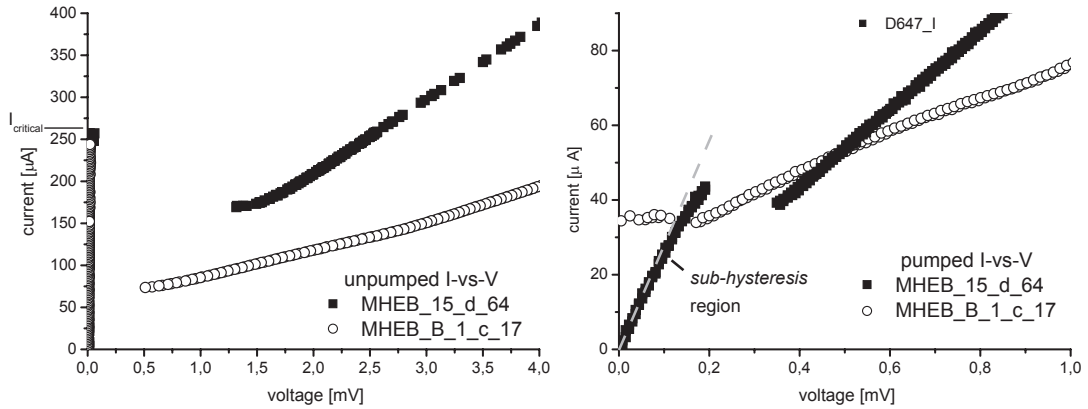


Figure 44: LO pumped and unpumped I/V characteristic curves of a working device (c_17) from batch MHEB_B_1 and a non-working (d_64) from batch MHEB_15. None of the devices of batch MHEB_15 showed heterodyne response.

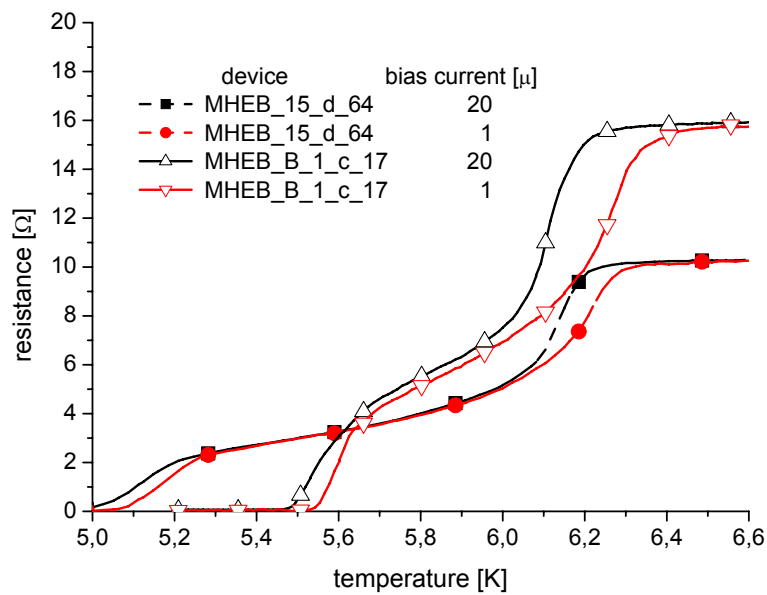


Figure 45: RT characteristic curves of a working device (c_17) from batch MHEB_B_1 and a non-working (d_64) from batch MHEB_15. None of the devices of batch MHEB_15 showed heterodyne response.

which we observe in the 0.2 to 0.4 mV bias range. Hence we can suspect an additional effect here. Assuming we have an electro/thermal effect, like a hot-spot, then the cooling at this part of the bridge must be very strong to allow biasing up to 0.2 mV without thermal runaway through *self-heating*. This would support the assumption of a hot-spot under or near the heat-sinks, because here the cooling is most efficient.

With these assumptions we can have a closer look at the R/T curves of the same device d_64 (fig. 45). We observe a similar R/T dependence around the critical temperature of the bridge as with device c_17. But the critical temperature of the *proximity step* is reduced nearly twice as much in relation to $T_{c_{bridge}}$, compared to device c_17. And the $\Delta T_{c_{proximity step}}$ was smeared and significantly larger. Note that $\Delta T_{c_{proximity step}}$ is significantly larger than $\Delta T_{c_{bridge}}$. If the $T_{c_{proximity step}}$ in the region of the heat-sinks is very low, this part might turn normal conducting, when the LO power is applied. Note, that the RF power is dissipated, even when the temperature is below T_c . If the HEB is additionally biased with a small bias current, heat would be dissipated in this normal conducting region. This might be an explanation for non-linear response of the LO pumped HEB at low bias voltages.

In summary, these observations and interpretations support the hypothesis of additional hot-spots underneath or near the heat-sinks. This leaves the question, how the HEB production can be improved to produce working devices. The comparison of process parameters and documentation has shown indications for correlation between the lift-off heat-sink fabrication and the R/T characteristic of the *proximity step*. In some batches, e.g. MHEB_15, the heat-sinks were poorly structured and the edges of the sinks were very rough. Overhanging gold flitter of more than 200 nm width has been observed, which sometimes has caused short-cuts of the HEB bridge. In these batches R/T curves with a significantly smeared proximity step have been measured. The lift-off quality of batch MHEB_B_1 has been significantly better than of batch MHEB_15 and other previous batches, due to changes in the fabrication. The heat-sinks on batch MHEB_B_1 were very smoothly structured with no overhanging gold residuals. Also very short bridges below 100 nm length came out without electrical shorts. A similar observation has been made with devices on fused quartz [60]. These observations are based on very few measurements and we cannot present a physical explanation, but it might be a hint for further research. In the following paragraph additional data of other batches is discussed. There this point of heat-sink fabrication is taken up again.

9.5.3 Comparison of devices made on Si_3N_4 membranes and on fused quartz

Comparing the characteristic RT curves of diffusion cooled HEBs made on silicon nitride membranes and on fused quartz in figure 46, shows only minor differences which are comparable to the fluctuations among different batches independent of the substrate material. The proximity step of the device of batch A on fused quartz looks even more similar to batch C made on the membrane than its brother of batch B, also

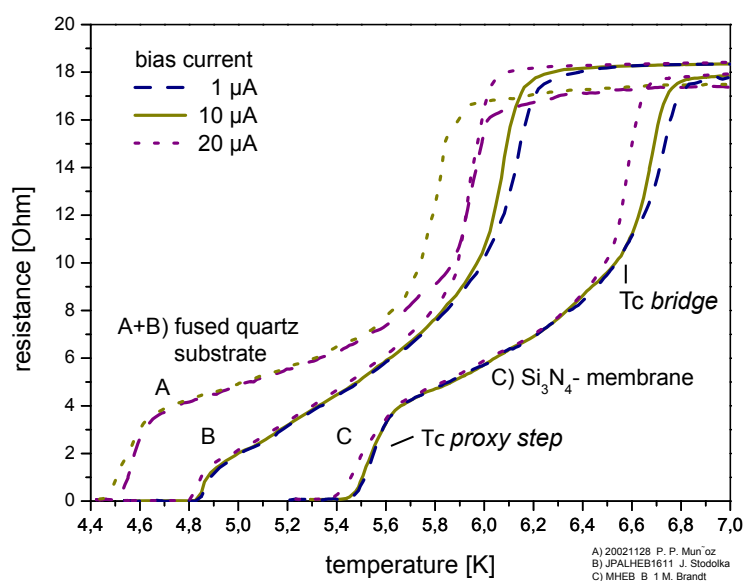


Figure 46: R vs T curves of HEBs made on fused quartz (A+B) and on silicon nitride membrane. The differences are rather small and comparable to the fluctuations among different batches, independent of the base material.

on fused quartz. This can be put down to the improvement of the fabrication process of the Au heat sinks between production of batch B and of batches A and C by P. Muñoz [60], leading to a steeper slope and increase of the proximity step by a factor of about two. The plateau between the proximity step and the Tc of the bridge, on the other hand, became more flat with sharper corners at the ends. The shift of the whole curve of batch C on the membrane of 1 K to higher temperatures cannot be explained in a satisfying way, but as it did not turn up on other batches on membrane it is very likely to be a singular problem. For phonon cooled devices, the absolute value of Tc might be an indicator for the IF bandwidth. The performance of diffusion cooled devices, however, is more dependent on the course of the curve. To sum up, the R/T measurements did not show any hints that the devices made on membranes would perform differently in a heterodyne experiment, than the ones made on fused quartz.

9.6 Thermal coupling of mixer device and copper mixer block

In the previous sections of this chapter, the HEB devices have been tested while they were still on the support wafer. Before the membrane mixer can be used as part of the heterodyne receiver, it has to be mounted in the mixer block. This section describes how the device mounting and receiver optics had to be changed for the new membrane technology. In chapter 5.2 the heat transfer between the HEB mixer device and the

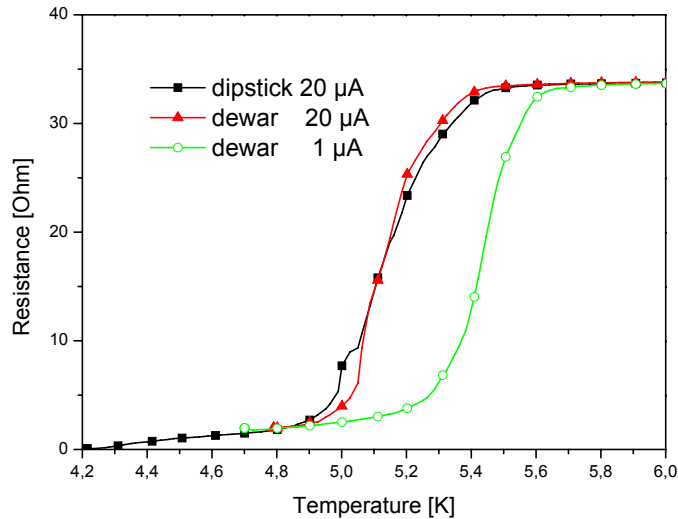


Figure 47: The characteristic R vs T curves did not show any shift in temperature when gained in a dipstick, where the liquid Helium provides perfect cooling, or in the vacuum of the dewar.

mixer block has been considered in a theoretical way. Here the thermal transport from the HEB to the mixer block is investigated while inside the dewar.

The standardly used CrystalBond to glue the fused quartz devices into the mixer, cannot be used to glue in the silicon frames which support the device membrane. The glue cracked and the frames broke off when cooled to 4.2 K. As the devices did not become superconducting, the cooling was not sufficient. It is assumed that the comparably larger gluing area of the frames caused the problems. Another material tested was W wax [57] by Apiezon. W Wax did not crack at temperatures down to 2.5 K, even when repeatedly thermo-cycled, and has shown sufficient thermal conductivity.

Figure 47 compares the characteristic R vs T curves of the same device measured in a dipstick and in the vacuum of the dewar. In the dipstick, the liquid Helium provides perfect cooling. Both curves with 20 μ A bias current show the same characteristic bath temperature dependence. In chapter 9.4 we have seen, how sensitive the R vs. T curve can respond to the bias current and thermal conductivity. As far as this DC characterization can tell, the HEB can be cooled through the freestanding membrane strip and the RF filter.

When the device was used in a heterodyne setup, the infrared (IR) radiation through the horn throat and the dewar windows heated the device slightly. The exact temperature was difficult to determine, but it was too high for a good mixer operation, as the

ends of the bolometer bridge became normal conducting. The ends of the bridge have a reduced T_c due to the proximity effect. In a first test the IR radiation was filtered with a fused quartz window which already reduced this effect. Then the fused quartz was replaced by Zitex [81]. Zitex is sintered Teflon with grain size matching the wavelength to be blocked. This leads to diffractive scattering of the unwanted frequencies, while the sub-millimeter band is only attenuated a few percent. It was positioned right at the 4 K window and thermally connected. With 8 layers of Zitex the IR radiation was totally suppressed, but fewer layers might be sufficient.

There are several possible causes why the IR heating effect seems to be stronger than with the classical fused quartz substrates. Unfortunately it is rather difficult to discriminate between them. One reason could be the freestanding design. Another reason would be the lower thermal conductivity of the membrane or the higher infrared absorption of the silicon nitride compared to fused quartz. Another uncertainty comes from the devices used for the IR filtering tests. These devices did not show heterodyne mixing, even when they were sufficiently cooled. It has not been tested, if working devices can be operated with less IR filtering.

9.7 Summary and conclusions of the DC measurements

The new I/V and R/T systems have been successfully developed and integrated into the thin film and device production chain and have significantly improved and sped up the device development at KOSMA. The following table gives an overview of some of the parameters which can be determined with these systems.

sample :	HEB	SIS	thin film
automatic determination	RN I critical I hyst. dI/dU	RN V gap I edge I sub-gap quality	RN Van der Pauw
manual determination	Tc bridge ΔT_c bridge Tc prox. step ΔT_c prox. step ΔR prox. step	tuning circuit- resonances	Tc R sheet RRR

Table 4: Characteristic parameters from the I/V and R/T measurements

In this chapter the diffusion cooled HEBs on Silicon Nitride membranes have been DC characterized and no obstacles for the heterodyne use have been found. Unfortunately these DC measurements can only provide guidelines to sort out devices which are

not likely to show mixing performance. At the current point of our research, it is very difficult to make reliable distinctions between working and non-working D-HEB devices with the information gathered from the DC measurements.

Phonon cooled HEBs have also been characterized with the described setups, but these developments are not in the focus of this work, but of [36] and [60].

10 Heterodyne measurements of HEB mixers on freestanding membranes

The following chapter describes the mixer operating as a heterodyne mixer in the receiver, and the parameters to be measured. To describe a receiver system several parameters are needed:

- the receiver noise temperature for the system sensitivity,
- the IF bandwidth to define the width of the detectable spectrum,
- the RF bandwidth defining the frequency band which can be detected,
- the stability which is needed for signal accumulation and integration.

The chapter starts with a general description of the heterodyne receiver setup. In the heterodyne setup, the receiver noise, gain and IF bandwidth are measured at various biasing conditions. In a second setup, described at the end of this chapter, the RF bandwidth is measured with the help of a Fourier Transform Spectrometer. The measured data is analyzed and compared with theoretical considerations to extract valuable information for further optimization of the fabrication process and for device selection.

10.1 Heterodyne setup description and basic theory

10.1.1 Heterodyne measurement setup

For the heterodyne measurements, the antenna horn is fixed to the finished mixer and both are mounted onto the 4.2 K cold plate of the liquid Helium dewar. Also inside the dewar, the first focusing mirror, the bias-T and the cold IF amplifier electronics are assembled.

The mixer is electrically connected to a bias-T, where IF signal and DC bias are separated. In the bias-T the IF signal is capacitively coupled to the IF amplifier. On a third DC port, a DC current is added to bias the mixer. The IF signal cannot leave through the DC port, because of inductive filter elements. The DC bias lines also have to be protected against high voltage pulses which can, for example, be caused by electrostatic discharge (ESD). These voltage pulses might otherwise destroy the extremely sensitive HEBs. The bias electronics are connected to a computer controllable DC-Bias-Box, where the DC bias voltage and current can be set and monitored. The amplified IF signal is led to the warm IF amplifier chain and to the power detector outside the dewar via stainless steel coax lines.

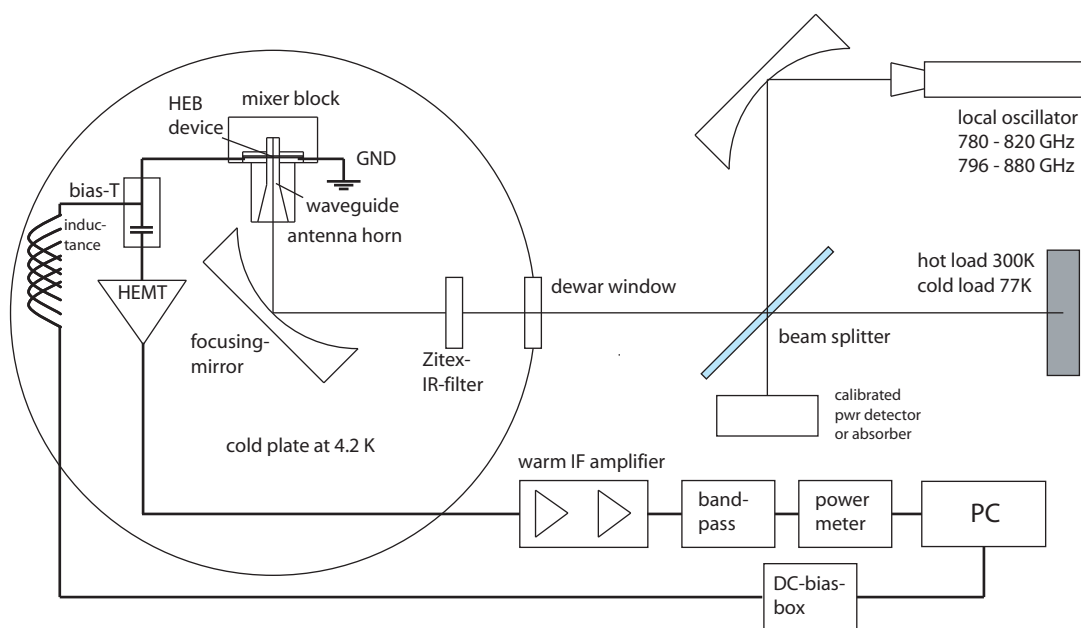


Figure 48: Heterodyne measurement schematic setup. The incoming signal of the hot or cold load, respectively, is overlaid by the local oscillator signal and fed through the dewar window to the HEB mixer on the 4.2 K cold plate. The down-converted IF signal is amplified and led outside for further processing and analyzing.

With a tunable band pass in the IF chain, a IF detection frequency can be chosen at which the noise temperature and the conversion gain are to be measured. The measured IF output power and the bias current and voltage are logged and filed by a PC for later analyzing.

The local oscillator signal, provided by a Gunn-diode with a multiplier, is combined with the RF signal at the beam splitter. Both are coupled into the dewar through the Teflon dewar window and the IR filter. The focusing mirror is needed to fold the expanding beam of the horn with its focus in the dewar window. For the measurements, black body radiation of an absorber is used as constant source of RF radiation (CW-source) instead of the astronomical signal. In this setup the signal is switched between a hot load at room temperature, and a cold load at 77 K liquid nitrogen temperature. Measuring the IF output power in relation to the RF signal power, the receiver gain can be calculated as described in the following section.

10.1.2 Sensitivity of a heterodyne receiver system

The sensitivity of a heterodyne receiver is defined by the minimum difference of the source temperature ΔT which can be detected in the observation time interval τ . It is described by the radiometer equation with the equivalent noise temperature T_{sys} of the receiver system:

$$\Delta T = \frac{T_{sys}}{\sqrt{\Delta\nu\tau}} \quad (59)$$

Here $\Delta\nu$ is the detection bandwidth. In the case of the heterodyne receiver it is the IF detection bandwidth. The signal is integrated over the time interval τ . Solving the equation for τ , we see that the observation time increases with the square of the noise temperature. Therefore the reduction of the noise temperature is of utmost importance.

The detector system consists of several components which convert and amplify the incoming signal, while a certain amount of unwanted noise is added. To simplify the calculation each component is modelled by a noise-less amplifier and a noise source at the input port. In this model, the noise source has the equivalent noise power of all the noise contribution from its real counterpart. So an input signal P_{in}^{sig} becomes amplified to $P_{out} = G(P_{in}^{sig} + P_{in}^{noise})$ which includes the input noise of the component P_{in}^{noise} . With two signals of known power and the corresponding ratio of output power, G_{sys} and P_{in}^{noise} can be determined. In the *hot/cold-method* the signal comes from two loads at two different physical temperatures, for example the 77 K and the 300 K absorber in figure 48.

$$y := \frac{P_{out,hot}}{P_{out,cold}} = \frac{G(P_{in,hot}^{sig} + P_{in}^{noise})}{G(P_{in,cold}^{sig} + P_{in}^{noise})} \quad (60)$$

$$P_{in}^{noise} = \frac{P_{in,hot}^{sig} - y \cdot P_{in,cold}^{sig}}{y - 1} \quad (61)$$

The y factor is introduced to simplify this calculation. Sometimes this method is referred to as the *Y-factor-method*.

The signal input power can be calculated from the physical temperature of the absorber with the help of the black body radiation formula by Callen and Welton, including the vacuum fluctuations:

$$P_{th}(f, T_{phys}) \equiv \frac{h \cdot f}{e^{\frac{h \cdot f}{k \cdot T_{phys}}} - 1} + \frac{h \cdot f}{2} \quad (62)$$

For high temperatures and low frequencies it linearizes to:

$$P_{th}(T_{phys}) \equiv k_B \Delta f \cdot T_{phys} \quad (63)$$

Because of this linear correlation, the power in equation 60 can be substituted and the noise temperature can be directly calculated from the known physical source temperatures T_{cold}^{phys} and T_{hot}^{phys} of the hot and cold source:

$$T_{noise} = \frac{T_{hot}^{phys} - y \cdot T_{cold}^{phys}}{y - 1} \quad (64)$$

Plotting the output power $P_{out}(P_{in})$ versus the input power we get a linear gradient which equals the total receiver gain. Substituting the input power with the source temperatures according to 63 the receiver gain can be calculated.

$$G_{sys}^{DSB} = \frac{P_{hot} - P_{cold}}{(T_{hot} - T_{cold})k_B \Delta \nu} \quad (65)$$

The receiver consists of several components in series, whereby each part contributes a certain noise and gain. The gains, which can also be smaller 1, e.g., for lossy components, multiply to the total gain. The noise contributions add up to the total noise T_{tot} with the following equation:

$$T_{tot} = T_1 + \frac{T_2}{G_1} + \frac{T_3}{G_1 \cdot G_2} + \frac{T_4}{G_1 \cdot G_2 \cdot G_3} \dots \quad (66)$$

When the mixer is measured in the heterodyne setup, noise is added to the measurement. The sole mixer noise can be calculated, if the noise temperatures and gains of all other components and the whole chain are known. Some of the components have to be measured in separate calibration measurements, while the noise contribution value of other components can be calculated. If the gain G is known, the equivalent noise temperature of passive components, for example optics and filters, can be calculated by:

$$T_{noise} = \frac{1 - G}{G} \cdot T_{phys} \quad (67)$$

In this case the gain is below 1 and is also referred to as *loss* (L) with $L=1/G$.

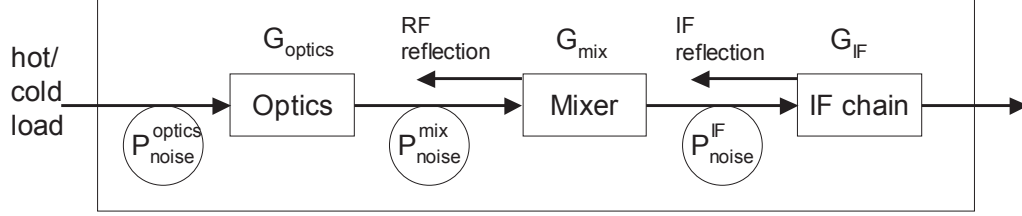


Figure 49: The components of the heterodyne receiver setup can be sorted into three basic parts: The optics to guide and process the RF signal, the mixer to convert the RF signal down to the intermediate frequency, and the IF chain for the final amplification and signal processing.

The *hot/cold-method* described earlier can also be used to determine the gain and the noise temperature of active components, e.g. the IF amplifier chain. In this case a resistor is used as Johnson noise source with known power according to 64. It is heated to different physical temperatures while the corresponding output power is plotted against temperature. From the gradient the gain of the components can be determined:

$$G = \frac{\Delta P(T)}{\Delta T k_B \Delta \nu} \quad (68)$$

The noise temperature can be calculated in analogy to the y-factor and equation 64.

10.1.3 Noise contribution and losses in the heterodyne receiver

The heterodyne receiver setup can be divided into three sections: The optics to guide and process the RF signal, the mixer to convert the RF signal down to the intermediate frequency, and the IF chain for the final amplification and signal processing.

In figure 49 the signal path has been sketched with the gains and noise contributions of the components. Note that the signal reflection at the input of the components due to mismatch have to be considered, too. The total noise of the system is then determined from the gains and noise value of the components by:

$$T_{sys} = T_{optics} + \frac{T_{mix}}{G_{optics}} + \frac{T_{IF\ 4.2K}}{G_{optics} G_{mix}} + \frac{T_{IF\ 300K}}{G_{mix} G_{optics} G_{IF\ 4.2K}} \quad (69)$$

The noise contribution of the IF amplifier at 4.2 K, and the one outside the dewar at 300 K have been considered separately.

The optics consist of

Component	G [dB]	T_{phys}	T_{noise} [K]
Beam splitter	-0.26	300	18.2
Dewar window 1	-0.026	300	1.9
Dewar window 2	-0.013	77	0.3
Zitex filter	-0.8	4.2-10	0.85-2

with the corresponding noise temperatures and gains at 820 GHz. The Zitex infrared filter has only a small noise value, although it causes rather high loss. The optical gain adds to -1.1 dB according to the listed components. The total noise contribution of the optics adds up to 21.4-22.5 K.

The incoming RF signal reaches the mixer via the antenna horn, matching the free space wave to the waveguide, and is coupled to the HEB with the waveguide probe. The mismatch between the bolometer impedance Z_{HEB} and the probe impedance Z_{probe} leads to RF reflection losses of Γ_{RF}^2 with

$$\Gamma_{RF} = \frac{Z_{probe} - Z_{HEB}}{Z_{probe} + Z_{HEB}} \quad (70)$$

The impedance of the probe as well as the coupling of the antenna horn are frequency dependent, the overall reflection losses vary significantly for different RF signal frequencies, as described in chapter 8.1 and measured with the FTS in chapter 10.4. On the other hand undesired out-of-band noise is strongly suppressed.

The mixer gain of HEBs is typically between -10 and -20 dB. This is small compared, e.g., to SIS devices. Hence the already small astronomical signal is further reduced and the noise of the following IF amplifier has more effect on the total system noise. This effect is seen in eq. 69, where the IF noise contribution is divided by the mixer gain. Good IF amplifiers, cooled down to 4.2 K, can reach noise temperatures of 5 K with 30 dB gain. After the first amplifier stage at 4.2 K the signal has become large enough, so that the noise contributions and losses of the following cables and amplifiers can be neglected (see equation 69).

10.2 Mixer measurements of diffusion cooled HEBs on membranes

10.2.1 Sensitivity and stability of diffusion cooled HEBs on membranes

The heterodyne mixer performance of the D-HEBs on membranes and on fused quartz have been measured in a liquid He cryostat. The devices were pumped with a solid

state local oscillator through a Mylar beam splitter (3% reflection @ 800 GHz) at frequencies between 660 GHz and 850 GHz. The output power of the intermediate frequency (IF) was measured when the receiver was looking at a hot load at 300K and at a cold load at 77K, respectively. With these data the receiver noise temperature (T_{sys}) and the receiver gain can be determined.

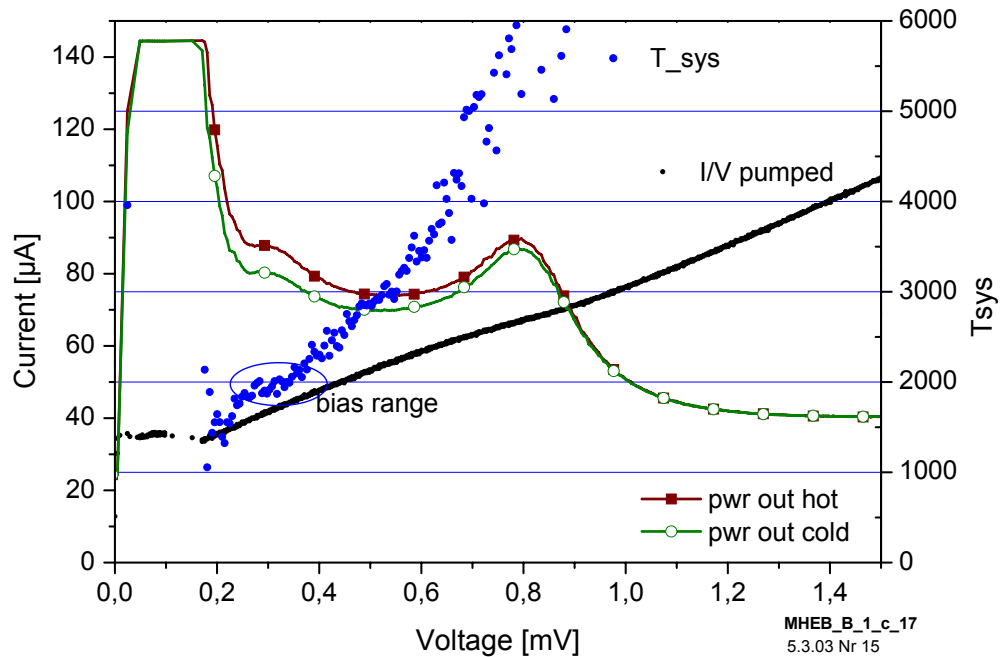


Figure 50: Performance of a diffusion cooled HEB on a 2 μm thick, freestanding Si_3N_4 membrane. System noise temperature below 2000 K for 0.2-0.35 mV biasing range (820 GHz, 4.2 K bath, IF 1.2 GHz, IF BW 50 MHz).

A minimum receiver noise temperature of 2000 K on the Si_3N_4 membrane at 820 GHz RF, 4.2 K bath temperature and a stable bias point of 0.3 mV was obtained. These seem to be the first heterodyne measurements of diffusion cooled HEBs on freestanding membranes used in waveguides. Figure 50 shows the corresponding IF output power and noise temperatures plotted against the bias voltage. The first striking feature in this graph are the two peaks in the IF output power. This effect is also seen in bolometers produced on fused quartz as seen in figure 51. In the plots of D-HEBs earlier produced, the IF output power monotonously increases towards smaller biasing voltages ([30]). In chapter 11, these two peaks will be discussed in more detail. Here a very practical aspect for the use of the bolometer is in the foreground.

The slope of the IF power between the peaks, especially in the region of the optimum bias point, is very flat. There is even a plateau between 0.25 and 0.35 mV as seen in figure 50. This plateau enables a stable mixer operation, as small changes of the bias voltage do not affect the IF output power level. At 0.2 mV the IF output power increases exponentially. Here the noise temperature drops below 2000 K, but a stable biasing is not possible. The bias voltage at the described plateau is distinctively higher than this critical bias region hence a stable biasing with good noise temperatures is possible there. With devices which only showed one peak, the optimum bias point has been found adjacent to the critical region and the biasing was less stable.

The bias voltage can be swept with a low frequency of a few Hertz, to scan the bias region. In this case, the mixer is measured repeatedly at critical bias conditions, but always only for a short time. In these short intervals, the output power can be measured and plotted against the bias voltage. Hence a sweep measurement can give good results even at unstable conditions, as long as the scanning is done fast enough. Manual biasing to a fixed point cannot reproduce these noise temperatures, because the IF output power varies significantly during the measurement. Because of the stable measurements with the devices presented here, the same results are found with constant biasing and with a swept bias.

Broadband RF radiation of the hot and cold load can change the average hot-spot temperature of the HEB. This effect is called direct detection. In the heterodyne detection, the temperature oscillates with the IF, while the average temperature remains constant. Direct detection can also change the level of the IF output power and can therefore be mistaken for a heterodyne response. Hence the bias voltage and current have to be monitored during the hot/cold measurement, because the changes in the average temperature can be determined as changes in the bolometer resistance. With the device presented here, no significant changes in the bias voltage were seen when the RF signal was switched.

It is possible to pump the D-HEB to normal resistance with a solid state local oscillator (LO) with about 20-40 μW of maximum output power, and a beamsplitter coupling factor of 3 %. For the optimum LO power the tripler, the last stage of the LO, was detuned to reduce the output power. This reduction is very difficult to estimate, so an exact figure for the total power needed for the optimum mixer performance can only be guessed to be below 500 nW.

10.2.2 Direct comparison of D-HEBs on membranes and on fused quartz

D-HEBs made on fused quartz but with otherwise identical fabrication process, were measured in the same heterodyne setup to enable direct comparisons.

Here we measured a receiver noise temperature of 1800 K on fused quartz at 4.2 K bath temperature. In the figures 50 and 51 the characteristic parameters for the two types of

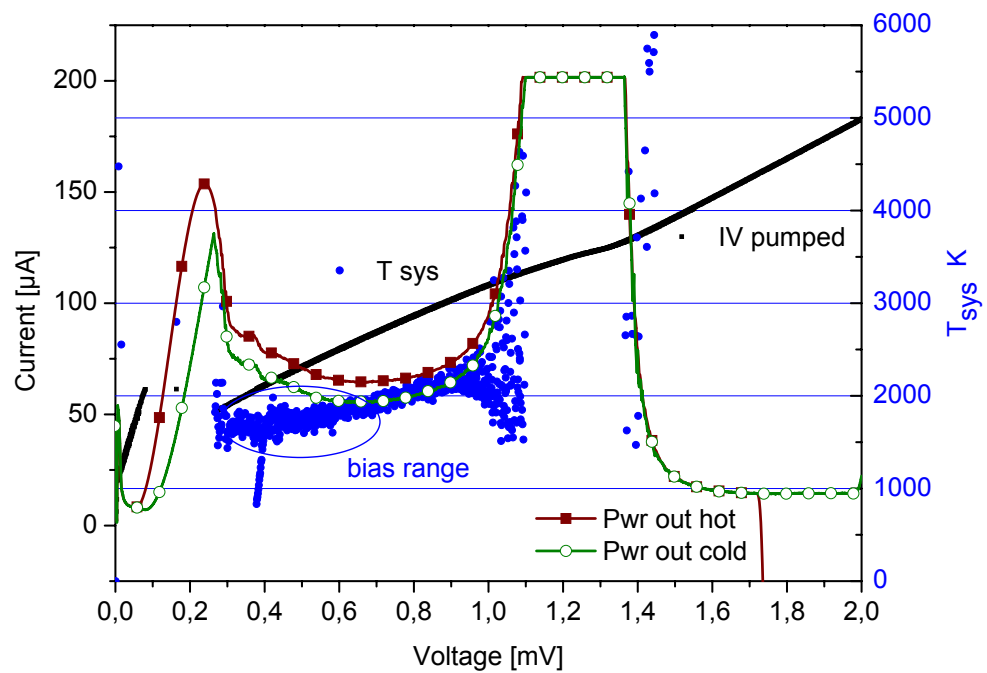


Figure 51: Performance of a diffusion cooled HEB on fused quartz. System noise temperature of 1800 K for 0.3-0.5 mV biasing range (820 GHz, 4.2 K bath, IF 1.2 GHz, IF BW 50 MHz).

mixers can be compared. IF output power, bias current, as well as noise temperature show a very similar dependence on the bias voltage. The two peaks in the IF output power are also found here. Differences in the characteristic curves and the device parameters are comparable to the fluctuations among different devices from different batches. This leads to the conclusion that diffusion cooled HEBs can be fabricated on membranes with a performance comparable to the ones produced on fused quartz

Increasing the substrate channel width from 100 μm for fused quartz at 800 GHz towards 172 μm for the Si_3N_4 membranes in this experiment did not significantly change the mixer performance. This confirms the results of the earlier mentioned CST microwave simulations with a 150 μm wide channel. The channel of the mixer used here was made wider than in the simulation, leaving a margin for later fabrication uncertainties. These considerations are also discussed in the following chapter which deals with the RF bandwidth measurements with the FTS.

10.2.3 D-HEB mixer performance at different bath temperatures

The mixer was tested at temperatures from 2.69 to 4.65 K. The bath and the mixer temperature were decreased by pumping on the liquid He.

At 2.69 K bath temperature, a 2 dB higher mixer gain has been measured than at 4.2 K. It also showed that more LO power has to be used at lower bath temperatures to optimally bias the mixer. We can assume that here more LO power is needed to heat the hot-spot to sufficient size.

According to the simple bolometer model discussed in chapter 4.2, the gain should increase when more LO-power is applied (eq. 13). So the observed increase in gain is in good agreement with this model. In general, a higher gain should also improve the signal-to-noise ratio. In contrast a very similar noise temperature is measured at 2.69 and at 4.2 K.

The plot of IF power versus bias voltage has changed significantly at the lower bath temperature as the second peak in IF output power has moved to higher biasing voltages and is significantly reduced in height. Increasing the temperature of the mixer block on the other hand, caused a rise of the peak and a shift to very small voltages. A noise temperature of 1200 K was measured here, but it becomes rather difficult to distinguish between heterodyne and direct detection under these conditions. It looks as if more complex mechanisms than those discussed in chapter 4, have to be taken into account in order to model these measurements. Chapter 11 tries to find a concept which might explain some of these phenomena.

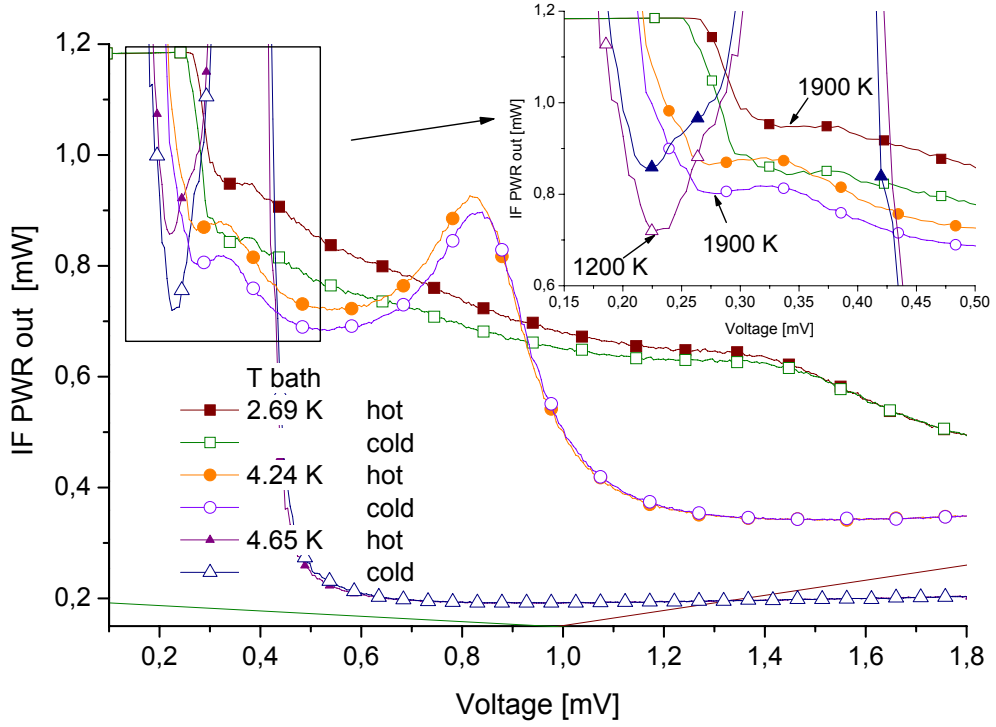


Figure 52: IF output power of D-HEB at different bath temperatures. The heterodyne biasing region is magnified in the insert with receiver noise temperatures printed in at the indicated bias points. The second peak in the IF output power, for example at 0.9 mV for 4.24 K bath temperature, shifts significantly with temperature.

10.2.4 IF bandwidth measurements of D-HEBs

The mixer gain and its dependence on the intermediate frequency (IF) was determined with hot/cold measurements, integrating a tunable bandpass. The tunable bandpass (bandwidth 60/80 MHz) was used to select the IF center frequency. The IF chains used for the D-HEBs were calibrated by heating the mixer block to temperatures between 6 and 22 K, thus producing a known thermal noise input with the bolometer as Johnson noise source (eq. 64). With 68 and 64, the gain and the noise figure of the chain can be calculated.

$$G = \frac{\Delta P(T)}{\Delta T k_B \Delta \nu} \quad (71)$$

$$T_{noise} = \frac{T_{hot}^{phys} - y \cdot T_{cold}^{phys}}{y - 1} \quad (72)$$

Two IF chains were used to measure the diffusion cooled HEBs. A 1-2 GHz chain was used with very good noise temperatures going down to 6 K, but rising to 38 K

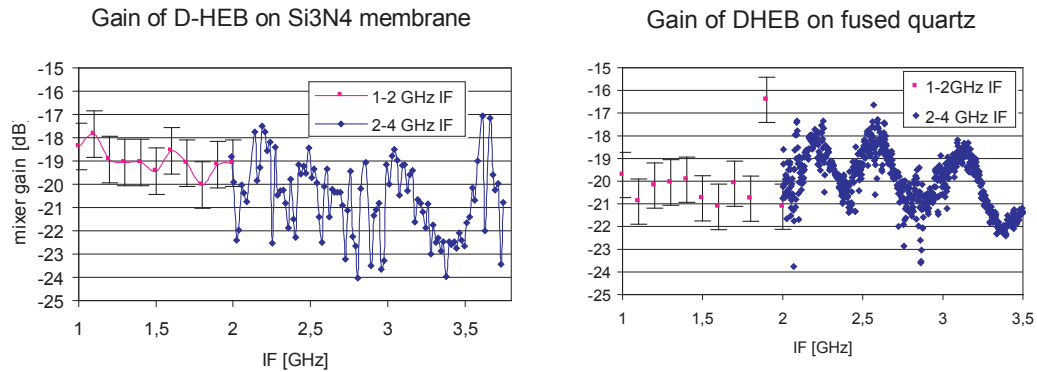


Figure 53: Mixer gain as function of the center frequency of the IF bandpass. No obvious roll-off appears up to 4 GHz for both types.

at 2 GHz. The 2-4 GHz band was measured with a chain which uses a YIG bandpass filter of 80 MHz bandwidth. The center frequency of the YIG can be tuned by applying a current. Unfortunately, problems with the current control circuit and software at the time of the measurements led to rather high uncertainty in these measurements.

Between 1 and 2 GHz the mixer gain remained flat at -19 dB within the measuring uncertainty of ± 1 dB. For 2-4 GHz the measurements did not show the same good quality, but no obvious roll-off appeared.

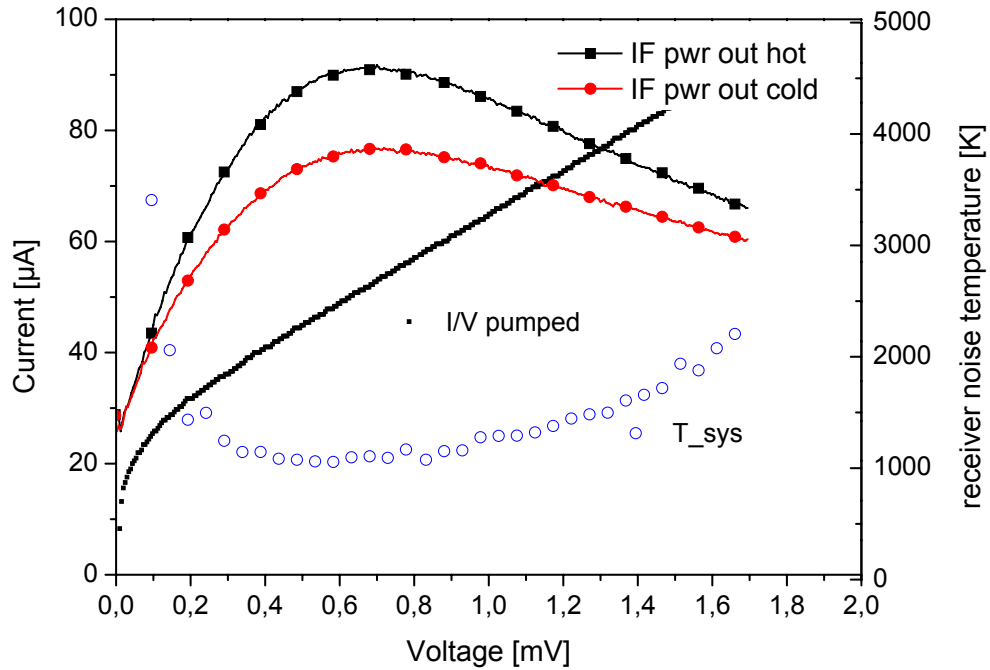


Figure 54: Performance of a phonon cooled HEB on a $2\ \mu\text{m}$ thick, freestanding Si_3N_4 membrane. System noise temperature of 1000 K for 0.5-0.7 mV biasing range (4.2 K bath, IF 1.0 GHz, IF BW 60 MHz).

10.3 Mixer measurements of phonon cooled HEBs on membranes

10.3.1 Sensitivity and stability of phonon cooled HEBs on membranes

Figure 54 shows the performance of a phonon cooled HEB on a $2\ \mu\text{m}$ thick, freestanding Si_3N_4 membrane inside a waveguide. To our knowledge these are the first measurements which have been done with P-HEBs on membranes with waveguides. A prototype HEB with a rather small bridge T_c of 6 K of a 4-5 nm thick NbTiN film and a significantly mismatched waveguide antenna probe was used. It showed a receiver noise temperature of 1000 K at 1 GHz IF (see fig. 54). Note that the best noise temperatures are found around the maximum IF output power. This enables a very stable biasing, compared to diffusion cooled HEBs, which is of utmost importance for the telescope operation.

There might be several causes, why the noise temperatures of other groups have not quite been reached. First of all it had been one of the first phonon cooled HEBs measured at KOSMA. Also the mask used for the production of this HEB was originally

designed for SIS mixers on fused quartz, therefore the RF coupling of HEB and waveguide is not ideal. Another point of concern is the very low T_c of the bridge. It looks as if the T_c has been decreased 3 K during the device production. The reduction of the T_c seems to be a problem of the general P-HEB device production at KOSMA, and it is currently under investigation.

The slight rise of the noise temperature between 1.0 and 1.2 GHz, described in the following paragraph, indicates an IF gain roll-off even below 1.0 GHz. In this case the noise temperature at lower intermediate frequencies might even be less than 1000 K. But the accuracy of the data is far too poor for a definite conclusion.

It was possible to pump the system with a standard solid state local oscillator at 800 GHz, which is not always the case for phonon cooled HEBs. A calibrated power detector was used to assess the needed LO power. It had been positioned on the other side of the beam splitter, opposite to the LO. So it measures the part of the LO power which is not reflected into the dewar, but the remaining 95% in transmission. The mixer was optimally pumped, when 4-5 μW LO power were measured at the power detector. 5% of the LO power have been reflected from the beam splitter into the dewar, which would correspond to about 200-250 nW LO power at the mixer.

A comparison of the unpumped and the pumped I/V curve can be used to calculate the LO power absorbed in the HEB. A LO power need of 5 nW calculated this way does not fit to the previously described values, even under consideration of the uncertainties. The same discrepancy is also reported from other groups.

10.3.2 IF bandwidth measurement of P-HEBs on membranes

Two methods were applied to calibrate the IF chain used for the P-HEB measurements.

One method used an unpumped SIS junction as calibration source. For the SIS junction the shot noise can be determined from the current-vs-voltage curve. It can be related to the measured IF output power to calculate gain and noise temperature of the IF chain. The other way was to heat the mixer block to different temperatures while the corresponding noise output was measured (10.1.2). With this data the gain and noise temperature can be measured as described in chapter 10.2.4 for the D-HEBs.

In some of the measurements an isolator was introduced between the mixer and the first IF amplifier. It absorbs the power which has been reflected at the amplifier input and would otherwise cause standing waves. The isolator which was used for this setup limited the IF bandwidth to 1.2-1.7 GHz. The measurements from 1.0-2.0 GHz were done without the isolator.

In contrast to the D-HEB measurements, the gain of the phonon cooled HEB clearly degrades from -12.5 to -19 dB in the range of the 1-2 GHz IF measured (see fig. 55, right). This corresponds to the rise in receiver noise temperatures measured, towards

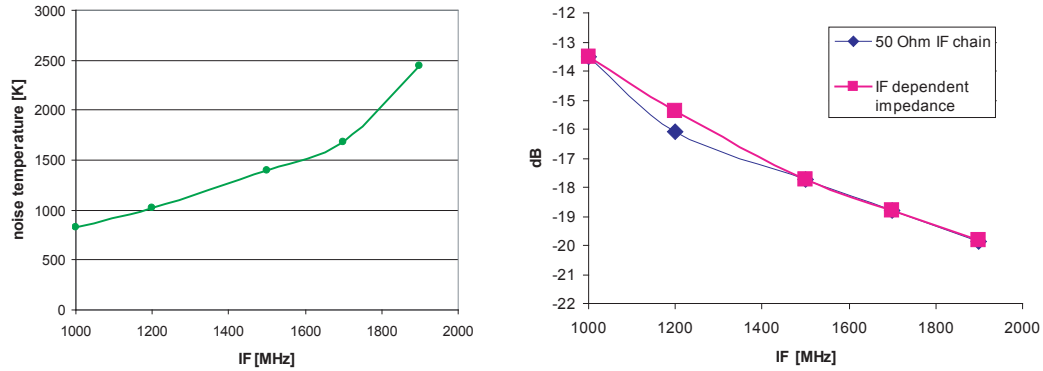


Figure 55: Left: P-HEB receiver noise temperature with a calculated flat IF of 5 K noise temperature. Right: Mixer gain as function of the center frequency of the IF bandpass. The gain decreases because the roll off seems to be below 1.0 GHz

higher intermediate frequencies. The noise of the used IF has been subtracted, as it varied significantly from 4 to 38 K noise temperature, and it has been replaced in the calculation by a state-of-the-art 5 K flat IF (fig. 55, left). The 3 dB noise bandwidth lays about 1.6 GHz. The mixer gain roll-off seems to lie even below 1.0 GHz. So on the one hand, even better noise temperatures might be expected there. But this also means on the other hand, that the IF bandwidth of this device is considerably small. There is hope, though, that the reduced bandwidth is related to the very low T_c of the device.

The T_c of the bridge had significantly degraded from 9 K down to 6 K during the production of the HEBs. It was measured before the membranes were freed from the support wafer, therefore it seems to be linked to the original HEB fabrication process and not to the membrane process. On this particular wafer, a comparably strong Ar ion clean step for the HEB contact pads was introduced, which very likely caused the degradation. There is no obvious reason why the film thickness of the bridge might have been reduced. Hence the reduction of T_c is more likely caused by a change in the film texture. This change might explain the small IF bandwidth, because the bandwidth strongly depends on a perfect lattice matching of film and substrate.

Thus the data of this first prototype experiment is not sufficient to tell whether there is a fundamental reason for phonon cooled HEBs on membranes to be inferior to the ones on bulk silicon, or if a comparable performance can be achieved with a better matched RF antenna design and improved HEB fabrication. Nevertheless the high sensitivity and stability of the prototype have allowed its use as detector in the SMART array receiver [14] at the KOSMA telescope at Gornergrat, Switzerland (ch. 12).

10.4 Fourier Transform Spectrometer measurements FTS

10.4.1 Introduction

The signal frequency response of the heterodyne receiver defines the RF bandwidth. It is determined by the optics, the horn antenna and the coupling of the waveguide probes with the HEB. It is difficult to measure the RF response with the heterodyne setup, as the local oscillator has to be tuned to a large number of frequencies to scan the spectrum. It cannot be secured that the biasing conditions remain constant throughout the scan, because the LO power has to be optimized anew for every frequency point. So the measurement is not only difficult and time consuming, but also afflicted with significant uncertainty. Hence a Fourier Transform Spectrometer FTS is used with the HEB as the direct detector. The idea is to apply a comb-like multi-line spectrum to the detector, instead of a single frequency line. This spectrum can be generated comparably easy with an interferometer. Thus an interferogram can be obtained by changing the line pattern while detecting the response of the HEB. This can be Fourier transformed to deduce the signal frequency response of the receiver.

10.4.2 FTS setup

The FTS is based on a Michelson interferometer with a white light source of the spectral density $S_{source}(k)$. The light is separated with a beam splitter (BS). Two mirrors, one of them moveable, define the spectral density of the signal $S_{signal}(k, x)$ exiting the FTS. The other frequencies are cancelled out through destructive interference. Hence we obtain the mentioned comb-like multi-line spectrum, which is entering the receiver through the dewar windows. It will be referred to as the *FTS light signal* in the following. The interference condition is defined by the optical path difference x between the beam splitter and the two mirrors, respectively. ($x = 2(l_1 - l_2)$, $l_{1/2}$ distance beam splitter to mirror $_{1/2}$).

$$S_{signal}(k, x) = S_{source}(k) (R_k T_k)^2 (1 + \cos kx) \quad (73)$$

R_k and T_k are the transmission and reflection coefficients of the beam splitter in relation to the wave number k . The HEB response to the RF signal is measured against the mirror displacement x . In general this is done by monitoring the bias current or voltage. The FTS response is the product of the response of the receiver setup $S_{rec}(k)$ and the spectra leaving the interferometer $S_{signal}(k, x)$. It is integrated over the wave numbers k of the signal spectrum.

$$S_{FTS}(x) = \int_0^{\infty} S_{rec}(k) S_{source}(k, x) (R_k T_k)^2 (1 + \cos kx) dk \quad (74)$$

$$= S(0) + \int_0^{\infty} S_{rec}(k) S_{source}(k, x) (R_k T_k)^2 \cos kx dk \quad (75)$$

$$= \frac{1}{2}S(0) + \mathcal{F}^{-1}\{S_{rec}(k) S_{source}(k) (R_k T_k)^2\} \quad (76)$$

\mathcal{F}^{-1} is the inverse Fourier cosine transform while $S(0)$ is the maximum detected signal at $x = 0$, which has to be subtracted before the transformation is done:

$$S_{rec}(k) = \frac{\mathcal{F}\{S_{FTS}(x) - \frac{1}{2}S(0)\}}{S_{source}(k) (R_k T_k)^2} \quad (77)$$

The frequency dependence of the FTS components is calibrated in a reference measurement. Because of the fourier transformation, the frequency resolution is defined by the maximum mirror displacement. In the FTS setup at KOSMA, a maximum mirror travel path of 43 mm leads to a resolution of 3.5 GHz. The whole FTS optics and nearly the total path towards the dewar can be evacuated to reduce the absorption by water vapour in the room air.

The same dewar assembly used for the heterodyne setup can be used unaltered for the FTS measurement during the same cooling cycle. It can be set in front of the FTS signal output, making it easy to switch from one setup to the other. The diffusion cooled HEBs are then heated to the superconducting transition temperature of the bolometer bridge. They are biased, so that the variations in the *FTS light signal* cause a linear response in the bolometer resistance. The biasing conditions are critical, as non-linearities of the hysteretic behavior of the HEB can cause artefacts in the fourier spectrum.

The phonon cooled HEBs need not to be heated and are much easier to bias. The bias range is larger and the biasing is more stable. The HEBs are normally shunted with a 25 Ohm resistor to stabilize the heterodyne biasing. Only the sum of bias current and shunt current can be measured in the setup used so far. Hence the signal is reduced compared to the non-shunted HEB. With an additional current sense line from the bias-T to the bias box, the bias current can be measured unaltered from the shunt. Then the optimum signal quality can be expected for both setups.

10.4.3 FTS measurements of D-HEBs and P-HEBs

The first tests of the HEBs on freestanding membranes as direct detectors for a Fourier Transform Spectrometer (FTS) confirmed the broadband RF coupling predicted by the CST microwave simulations.

In figure 56 the optimized RF filter design for the diffusion cooled HEBs on membranes shows a RF band from 600 GHz to 850 GHz (FWHM) with a large plateau.

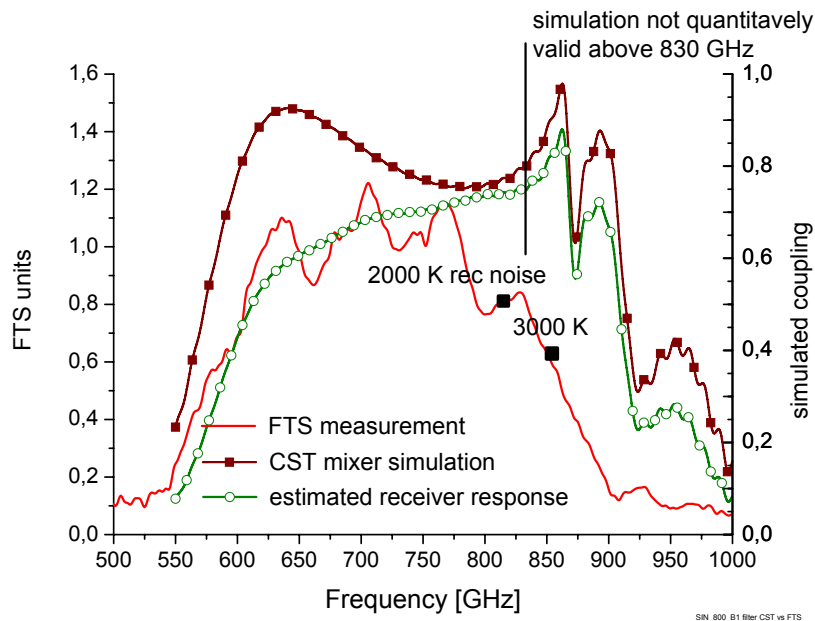


Figure 56: Fourier Transform Spectrometer measurement of a diffusion cooled HEB on a freestanding membrane. The broadband coupling of the mixer is limited at high frequency because the substrate channel had been fabricated too wide, and at low frequencies due to the bandwidth limitations of the used Potter horn. The receiver noise temperatures measured at 820 and 860 GHz respectively, confirm the FTS data. The simulations above 830 GHz cannot be used quantitatively.

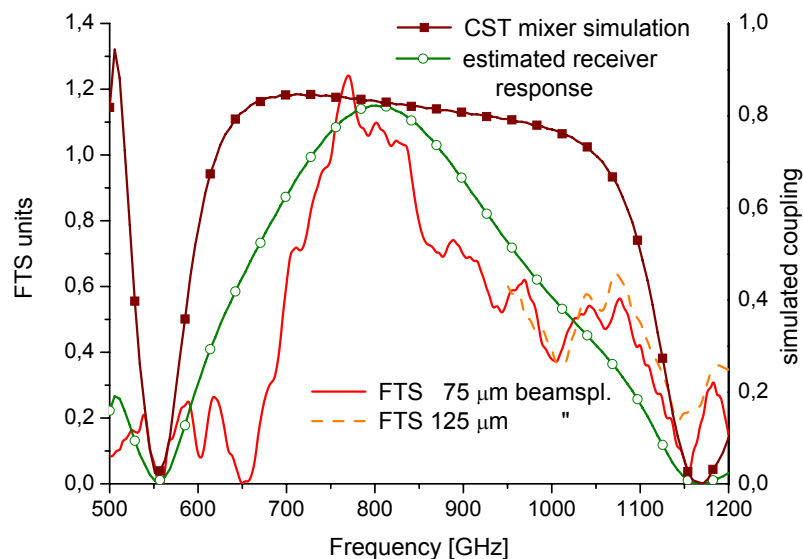


Figure 57: Fourier Transform Spectrometer measurement of a phonon cooled HEB on a freestanding membrane. The broadband coupling of the mixer is limited by the bandwidth limitations of the used Potter horn.

The fast oscillations are more likely to be artefacts of the measurement than to be caused by the waveguide mixer. The mixer-to-waveguide coupling simulated by CST is still below 1, because the measured HEB has the impedance of only 16 Ohm, and the design has been optimized for 20 Ohm D-HEBs. The waveguide impedance is above 300 Ohm, therefore the transformation is much more difficult than for P-HEBS with an impedance of about 100 Ohm.

The decrease in the FTS response above 830 GHz can be expected, because the substrate channel of this mixer block was made 22 μm wider, than the originally designed 150 μm . Here we get into the range of the cut-off frequency of the substrate channel, and RF can leak into the substrate channel. The used simulation program by CST cannot model this complex mode structure, so here the simulations cannot be used. We find a sharp transition and spikes instead of the expected decrease in sensitivity between 830 and 900 GHz. For comparison an empty waveguide without dielectric or IF micro-strip filter would have a cut-off frequency of 870 GHz. Hence above 830 GHz, the simulated results have to be used with caution. It can be estimated that the mixer response drops drastically when the RF blocking becomes leaky. This would match the reduced FTS response seen above 820 GHz in the plot. The measured increase of the receiver noise temperatures from 2000 K at 820 GHz to 3000 K at 850 GHz, also written into the graph for the overview, additionally confirms the FTS measurement.

It is very important to support the simulated results regarding the influence of the substrate channel width, because the production of the channel is very difficult at the aimed 1.9 THz RF. Hence one would prefer to design the channel as wide as possible, while also taking the production tolerances into account. Here trustworthy simulations would considerably reduce the number of experiments necessary at 1.9 THz.

Below 700 GHz the frequency response of the receiver drops faster than in the simulation of the waveguide mixer. In the following section the additional losses due to horn optics and waveguides are discussed, which might explain this decrease.

The phonon cooled HEB has been built into a mixer block with correct substrate channel dimensions. Here we can measure a broader RF response. It is plotted in figure 57, together with the corresponding CST simulation of the waveguide mixer. Again we have to consider the frequency response of the horn antenna, which will be discussed in the following section. The FTS measurement has been done with two different beam splitters (BS) of 125 and 75 μm . The optimum frequency response of the 125 μm BS lies at 1200 GHz while the optimum of the 75 μm BS lies at 900 GHz, whereby both can be used for the higher end of the measured band. Here the two corresponding FTS measurements of the receiver match, corroborating the measured data.

The IF filter and waveguide probes used were originally designed for SIS junctions on fused quartz, as described in section 10.3. The membrane had been built into the substrate channel only 5 μm below the top of the channel. The CST simulations have predicted that the assembly of the membrane at half the height of the channel would

have led to a strong RF mismatch and to high reflection losses. Any assembly tolerance is expected to significantly alter the RF response, because of the very limited distance between the micro-strip line and the counter electrode of the ground plane. In this light the comparison of measurement and simulation looks very promising.

10.4.4 Comparison of FTS results and CST simulations

In both plots of the D-HEB and the P-HEB the predictions of CST simulation have been added. It looks as if an even broader RF bandwidth could be expected than it has been measured with the spectrometer. The simulations were focused on the waveguide channel and probe design, thus the influence of the antenna horn has not been integrated into the calculations. There are two main points which have been neglected in the CST simulations, and which are also frequency dependent:

- waveguide transmission losses from the horn throat to the mixer cavity,
- frequency dependent beam mismatch between the used potter horn and the receiver optics.

These two aspects are discussed as follows.

The first aspect concerns the losses from horn throat to mixer cavity. At a wavelength of about $300\ \mu\text{m}$, RF losses in the waveguide have to be taken into account, even if the distance between the horn throat and the mixer cavity is only 3 mm. The losses become larger when the frequency comes near the ends of the RF band. In figure 58 the losses for a 3 mm waveguide with an assumed surface resistance of $2\ \mu\Omega\text{cm}$ have been calculated. This is the room temperature DC value of bulk material. It is very difficult to determine the microwave surface resistance inside the waveguide, as it not only depends on the resistance of the gold used as coating material, but also on the surface roughness. So the plot can only provide qualitative information.

In the plot the increasing losses below 600 GHz can be seen. At the high end of the band at 930 GHz the waveguide becomes over-moded, when the wavelength of the signal becomes as large as the width of the channel. In this case the coupling of the signal to the waveguide probe drops drastically. In the simulation the coupling to the probe has not been modeled, because it would have taken significantly more calculation power and would still not lead to accurate results. The capability of CST to simulate over-moded structures is only limited, as mentioned before. Hence the decreased coupling, expected for higher frequencies, is not found in the plot.

The second aspect concerns the beam mismatch between the horn and the receiver optics. The horn transmission on its own is mostly defined by the waveguide frequency response as mentioned above. But more important, the beam pattern or profile of

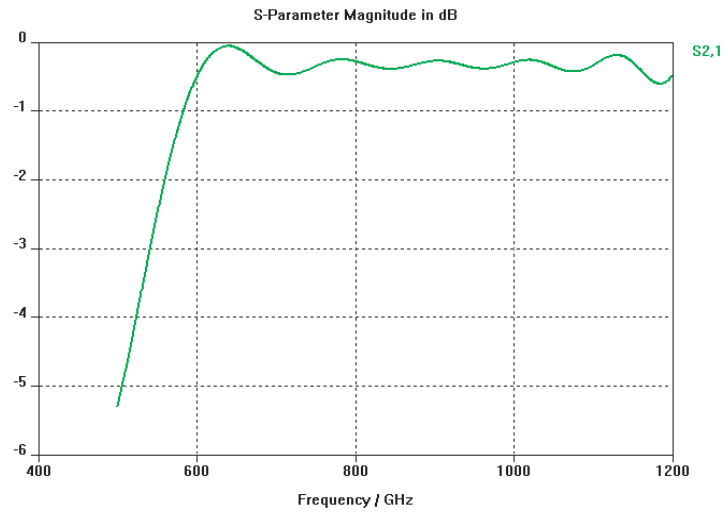


Figure 58: Transmission losses for a 3 mm waveguide with an assumed surface resistance of $2 \mu\Omega/cm$. The reduced coupling above 930 GHz, when the waveguide becomes over-moded, has not been considered.

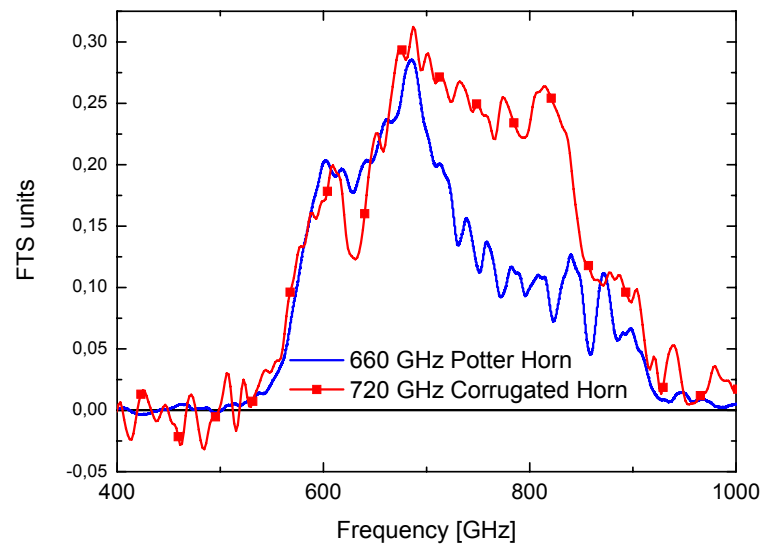


Figure 59: Comparison of two FTS measurements with the same SIS device with different horn antennas to estimate the bandwidth of a potter horn.

the used potter horn varies also with the frequency. At the center frequency of 800 GHz of the horn, the beam should be nearly single-moded and gaussian. Going to other frequencies, the beam profile changes and the beam widens. In this case the beam can be truncated by the first mirror and the dewar window, reducing the receiver sensitivity. The frequency dependent coupling between the optical components has not been calculated in detail, because it is very complex and would go beyond the focus of this work. A lower limit of the frequency dependence can be estimated from the comparison of the potter horn with a much more broadband corrugated horn, described in chapter 7.5. This has been done with a SIS detector as seen in figure 59.

In the next step, the influence of both aspects on the frequency response of the receiver are discussed. For this purpose, an assumed frequency response of the horn and the waveguide has been added to the two FTS plots in 56 and 57. It is later referred to as the *expected receiver response*. Here the losses have been used as calculated in figure 58, together with a simple parabolic frequency response of the receiver optics with:

$$beam\ coupling(f_{RF}) = \left(1 + \frac{(f_{center} - f_{RF})^2}{50000}\right)^{-1} \quad (78)$$

This corresponds to a 1dB bandwidth of the horn of 36%.

The expected receiver response with the D-HEB in the lower frequency band is well modeled as can be seen in figure 56. The upper band can only be modelled qualitatively as mentioned in the previous section. Here the leakage of RF into the substrate channel cannot be calculated quantitatively.

The expected receiver response with the P-HEB looks similar to the FTS response of the receiver. However, the FTS response seems to drop faster towards lower frequencies than in the model. Maybe the losses due to the horn and the waveguide have been underestimated in the described model. In the range of 930 GHz, where the waveguide becomes over-moded, the FTS response is smaller than estimated. As mentioned before, the simulations and estimations do not consider the higher modes correctly. We can summarize: the RF bandwidth is limited mainly by the potter horn and its waveguide section not so much by the coupling of the HEB to the waveguide signal.

10.5 Final discussion of the RF measurements

Diffusion cooled and phonon cooled Hot Electron Bolometers have been fabricated on freestanding silicon nitride membrane strips and successfully used in heterodyne measurements. A modified flip-chip process is used to bond the devices to a separately fabricated silicon frame. The Si_3N_4 membranes with a thickness of $2\ \mu\text{m}$ can be safely mounted and positioned with the KOSMA Micro Assembly Station.

The DC and RF heterodyne device characteristics of the diffusion cooled HEBs are very similar to bolometers fabricated on quartz substrates. A sensitivity of 2000 K has been measured with membrane devices under stable bias conditions. This is a similar value as it has been obtained with other diffusion cooled HEBs on fused quartz by P. P. Muñoz [60] and J. Stodolka [30]. IF bandwidth measurements did not show a gain roll-off below 4 GHz. Note that most groups have stopped their D-HEB programs due to problems in the reproducibility of the fabrication.

The phonon cooled HEB showed a high sensitivity of 1000 K and a very good stability in the heterodyne measurement and has therefore been integrated into the SMART array receiver [14] at the KOSMA telescope at Goernergrat, Switzerland (ch. 12). To compare the results of this work with the achievements in the HEB development and fabrication of other groups, a brief summary of the current status can be found in table 5.

Diffusion cooled HEB mixers comparison

Group	Author	f [GHz]	mixer	T _{sys} [K]	Gain [dB]	T _{bath} [K]
KOSMA	this work	820	wave	2000	-19 _{DSB}	4.2
KOSMA	Muñoz [60]	820	wave	1800	-20 _{DSB}	4.2
KOSMA	Stodolka [30]	780-800	wave	2200 _{uk}	-18 _{SSB}	4.7
KOSMA	Fiegle [82]	800	wave	4300 _{uk}	-	4.2
KOSMA/ IRAM	Frommberger [83]	800	wave	6300 _{uk}	-	4.2
SRON, DIMES	Wilms-Floet [23]	700	wave	1650	-19.3 _{SSB}	4.2
SRON, DIMES	Ganzefles [84]	640	q.opt.	1500	-16 _{SSB}	4.2
NASA/JPL	Skalare [85]	630	wave	3000 _{uk}	-19 _{SSB}	4.2
NASA/JPL	Karasik [86]	2500	q.opt.	2500 _{uk}	-	4.2
	Wyss [87]	2500	q.opt.	1800 _{uk}	-	2.3

Phonon cooled HEB mixers comparison

Group	Author	f [GHz]	mixer	T _{sys} [K]	IF [GHz]	material
KOSMA	this work + [60]	820	wave	1000	1	NbTiN
KOSMA	Bedorf [36], [11]	1600	q.opt.	1600	1.5	NbTiN
KOSMA/ IRAM	Frommberger [83]	800	q.opt.	675 _{uk}	?	NbN
KOSMA/ Chalmers	Bedorf / Khosropanah [11]	700	q.opt.	700	1.5	NbTiN
KOSMA/ Chalmers	Bedorf / Khosropanah [11]	1600	q.opt.	1100	1.5	NbTiN
KOSMA/ Chalmers	Bedorf / Khosropanah [11]	2600	q.opt.	3000	1.5	NbTiN
Chalmers	Cherednichenko [35]	600	q.opt.	450	1-2	NbN
		600	q.opt.	700	3	NbN
		1600	q.opt.	700	1-2	NbN
		2500	q.opt.	1100	1-2	NbN
SRON, DIMES	Baselmans [12]	2500	q.opt.	950	1.1-1.8	NbN

Table 5: Comparison of different phonon and diffusion cooled Hot Electron Bolometer mixers. (wave: waveguide, q.opt.: quasi-optic mixer)

11 Finite element simulation of diffusion cooling in HEBs

The measurements of diffusion cooled HEBs on membranes and on fused quartz presented here showed two significant peaks in the IF output power plotted against the bias voltage. As the bolometers with this effect showed much better biasing stability and good noise temperatures, it is interesting to further investigate this phenomenon. Hence a simulation program has been written, which will be presented and discussed in this chapter. These investigations might help to analyze and better understand the dipstick measurement data and might allow pre-selection of good devices before they are integrated into the mixer block.

11.1 Problem description

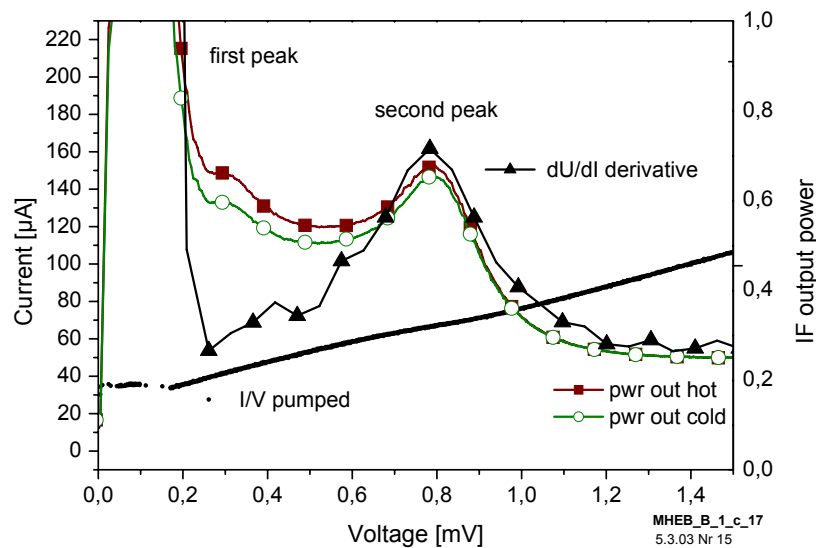


Figure 60: Measured IF output power and dU/dI derivative in relation to the bias voltage.

One of the peaks of the IF output power plotted against the bias voltage is found at high bias voltages where the hot-spot is large and the normal conductor/superconductor interface is near the heat sinks. In this region the critical temperature is reduced due to the proximity effect. The increase of the IF output power might be connected with the spatial profile of the critical temperature in this region. In the context of this work a Finite Element (FE) simulation program has been developed and applied to investigate this matter. In this program complex critical temperature profiles across the HEB

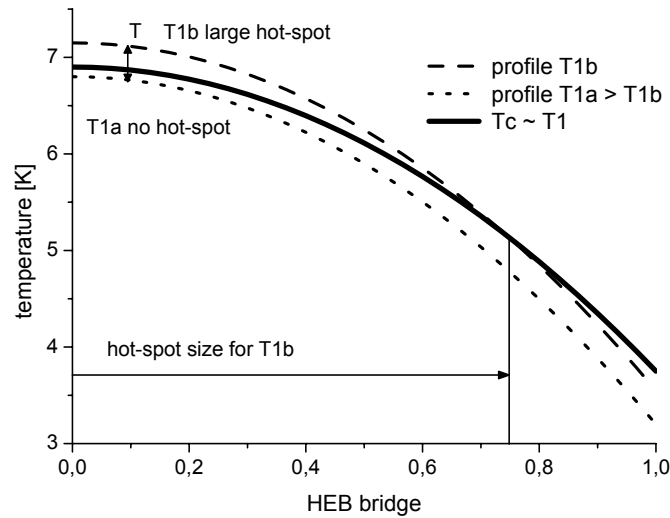


Figure 61: If the temperature profile of the hot-spot resembles the profile of the critical temperature T_c , large parts of the bridge turn normal conducting as response to small temperature variations ΔT .

bridge can be modelled to calculate the corresponding electron temperature profiles for various biasing conditions. The first discrete modelling of a HEB has been done by Anders Skalare [88]. The model presented here is based on the thermal transport equations of the hot-spot model, developed by Wilms Floet [23]. Wilms Floet analytically solved the corresponding differential equation. To allow an analytical solution, however, Floet used simplifications like temperature independent thermal conductivity. Therefore it is not possible to insert different critical temperatures for different regions of the bridge into Floet's model. H. Merkel [89] introduced several additional physical aspects for phonon cooled HEBs into the differential equations and has used numerical approaches to solve these equations. It might be possible to insert further additional aspects of diffusion cooling and different critical temperatures into Merkel's model, but it would then be even more difficult to apply this model because of its complexity. Therefore the program developed in this work is kept simple and is specially adapted to investigate the influence of the T_c profile across the bridge on the hot-spot. This approach is described in the following.

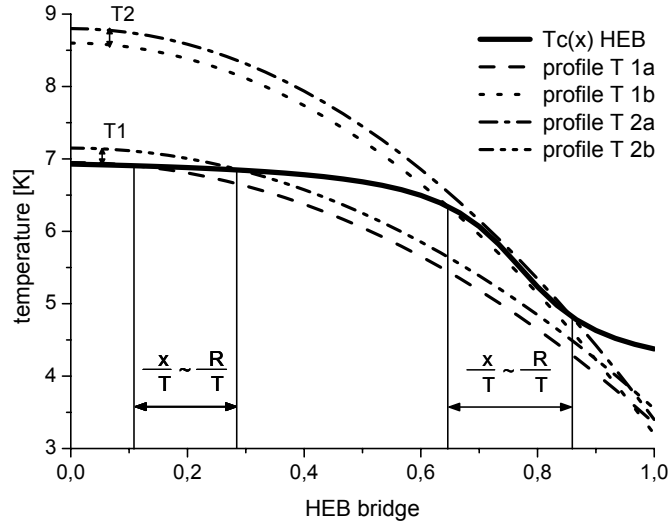


Figure 62: The critical temperature at the end of the bridge is reduced. The HEB response increases when the temperature profile of the hot-spot resembles the T_c slope near the heat sinks (T2a/T2b).

11.2 HEB response and its dependence on the biasing conditions

The signal response S_{HEB} of the HEB is proportional to the resistance versus temperature (dR/dT) gradient as described by the lumped-element model (eq.4).

$$S_{HEB} \propto C \frac{dR}{dQ} = \frac{dR}{dT} = \frac{dU}{dI dT} \quad (79)$$

The differential resistance can be written as $dR = dU/dI$. Note, that the *self-heating* and the corresponding effective cooling also depends on the gradient dR/dT (ch. 4.5)

$$G_{eff} = G - I_0^2 dR/dT \quad (80)$$

Hence we can expect a correlation between the *self-heating* and the HEB response.

In the hot-spot model, the HEB response is deduced to variations of the hot-spot size as a function of its temperature (hot-spot model [23]). The HEB resistance can be determined from the normal conducting section L_{HS} of the bridge:

$$R_0 = L_{HS} RN_x \quad (81)$$

Here RN_x is the resistance per length of the bridge. The hot-spot is described by a temperature profile. Hence the relation between absorbed power dQ and change in resistance dR is much more complex than the linear relation in eq. 79.

Figure 61 visualizes an example hot-spot temperature profile with parabolic shape. In this example the critical temperature is also modelled with parabolic shape. When the hot-spot temperature profile increases a little from T1a to T1b, a large part of the bridge exceeds the critical temperature and becomes normal conducting. The corresponding increase in resistance R relates to a large gradient $\Delta R/\Delta T$ and HEB response S_{HEB} , respectively. The T_c profile of a real diffusion cooled HEBs is approximately flat in the center of the bridge and decreasing towards the heat sinks where the T_c is reduced due to the proximity effect (fig. 62). There are two cases in which the temperature profile resembles the T_c profile in sections of the bridge: First, when only the approximately flat center of the temperature profile exceeds the critical temperature and a small hot-spot develops; Second, when the slopes of the temperature profile of a large hot-spot approach the slopes of the decreasing T_c profile at the heat sinks.

In figure 60 the measured IF output power, bias current and (dU/dI) derivative of a LO pumped HEB have been plotted against the bias voltage. The relation of the IF output power to the dU/dI derivative are obvious. At 0.7 mV a local maximum of IF power and dU/dI can be found. This peak will be further referred to as the *second peak*. Both functions also show a drastic increase towards 0.2 mV at the *first peak*.

The simulations presented in the subsequent sections try to model the HEB response on the basis of the available I/V and R/T data. This modelled response can be compared with the measured response in order to investigate whether the earlier described *second peak* can be related to such a case.

11.3 Simulation concept

The bridge and the adjacent heat sinks were divided into a finite number (80) of elements (figure in table 6). Hence the single elements have a macroscopic size (e.g. $\Delta x = 2.5$ nm) [88]. This is the main difference to other approaches, for example by Floet or Merkel, where the equations are solved by letting $\Delta x \rightarrow 0$.

The physical properties along the bridge are set differently for each element and anew for each time step Δt . Several aspects of the device physics can thus be included in a comfortable way.

1. the profile of critical temperature and current, respectively, to model the proximity effect,
2. the temperature dependence of the thermal conductivity G ,
3. the reduced thermal conductivity at the NC to SC interface due to Andreev reflection,
4. *self-heating* and *electro/thermal feedback*.

This list can be easily extended or adapted to incorporate additional features, e.g. phonon cooling. In a repeat loop the heat input and output for each element (tab. 6) is determined with simple heat exchange equations. This cycle is repeated until the bias heat input and the heat outflow through the heat sinks have been balanced to a stationary temperature profile.

11.4 Simulation routine

Table 6, bottom, sketches the heat input and transfer at the elements. If the critical current I_c at the element is smaller than the applied DC bias current, the power $P = I^2 R N_x$ is dissipated and heats the element. The incoming LO RF power is dissipated independent of the actual temperature, because the LO frequency is above the gap frequency. The heat transport between two systems at different temperatures is simply described by:

$$\Delta Q = A(T_2 - T_1)/G, \quad (82)$$

whereby A is the cross-section of the bridge and G the thermal conductivity. The change in temperature is related to the heat input via the heat capacity C :

$$\Delta T = \Delta Q/C \quad (83)$$

To each section the critical temperature $T_c(I = 0)$ and the critical current at 0 K $I_c(K = 0)$ were assigned. The T_c in the center of the bridge drops towards the heat sinks, because of the proximity effect. The T_c and $I_c(0)$ values have been estimated from the R/T and I/V curves of devices MHEB-B-1-c17 which has also been measured in the heterodyne setup (fig. 60). The simulation program was used to calculate R/T curves at a constant bias current with the estimated T_c profile. These were compared with the measurements to further refine the estimations.

The critical current $I_c(T)$ in each section is calculated anew from the actual local temperature for every time step.

$$I_c(T) = I_c(0) \left(1 - \frac{T}{T_c}\right)^{\frac{3}{2}} \left(1 + \frac{T}{T_c}\right)^{\frac{1}{2}} \quad (84)$$

In the simulation the criterium $I_{bias} > I_c(T)$ has been used to decide which elements of the bridge are normal conducting. The critical current depends on the difference of the electron temperature and T_c . The critical temperature depends on the bias current, because the bias current generates a magnetic field. At the transition temperature between normal and superconducting state we find $T = T_c$ and $I_{bias} = I_c$. Hence I_c and T_c can be used equally as critical criteria. In some of the plots the reduced $T_c(I_{bias})$ profile is plotted for transparency.

repeat		
power dissipation:		
for i = 0 to nr. elements		
$I_c(i)$	$= I_c(T = 0) \left(1 - \frac{T(i)}{T_c(i)}\right)^{\frac{3}{2}} \left(1 + \frac{T(i)}{T_c(i)}\right)^{\frac{1}{2}}$	critical current [μA]
$\Delta Q_{DC}(i)$	$= RN_x I_{bias}^2 \Delta x \Delta t 10^{-12}$ if $I > I_c$	DC power diss. [W fs]
$\Delta Q_{RF}(i)$	$= \phi_{LO} \Delta x \Delta t 10^{-6}$	RF power diss. [W fs]
$T(i)$	$= T(i) + (\Delta Q_{DC} + \Delta Q_{RF})/C$	T at element i [K]
next i		
heat transport:		
for i = 0 to nr. elements		
$G(i)$	$= G_{cor} G_{Nb} (8 \cdot T(i)/T_c(i))$	thermal conduc. [W/mK]
$G(i)$	$= G(i)/\Lambda$ if NC/SC interface at i	red. G due to Andreev ref.
$\Delta Q_{trans}(i)$	$= (T(i) - T(i+1)) A G(i) \frac{\Delta x}{\Delta t} 10^{-9}$	trans. from i to i+1 [W fs]
$T(i)$	$= T(i) - \Delta Q_{trans}(i)/C + \Delta Q_{trans}(i-1)/C$	ΔQ from i-1 and to i+1 [K]
next i		

calculate total HEB resistance R_{HEB} from temperature profile ($T > T_c$ or $I > I_c$)

$$U_{bias} = I_{bias} \cdot R_{HEB}$$

until thermal equilibrium has been achieved

I_{bias}	DC bias current [μA]	RN_x	normal resistance bridge
ϕ_{LO}	LO power [$\mu\text{W/nm}$]		per length Δx [Ω/nm]
$G_{Nb}(T/T_c)$	thermal cond. Nb (tab.7) [W/mK]	$I_c(T = 0)$	critical current at 0K [μA]
		Δx	bridge length interval [nm]
C	heat capacity [W fs/K]	Δt	time interval [fs]
Λ	Andreev reflection > 1	A	bridge cross section [nm^2]

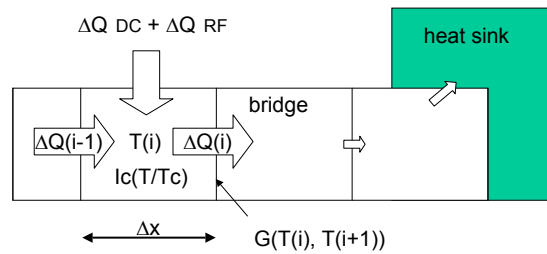


Table 6: Top) Calculation procedure for Finite Element D-HEB simulation. Bottom) Heat flow schematic at the section i of the HEB bridge

To model the temperature dependence of G , the values for G_{Nb} of cured, bulk Nb (RRR=300) have been scaled. The bulk values have been divided by 10 which results in a thermal conductivity of 50 W/mK at $T = T_c$. The factor 10 has been chosen as start value to roughly fit the temperature profile to the dissipated power, but in this specific case it might have been chosen too large. The resulting simulated LO power levels and DC bias values are slightly larger than in the measurement. Also the estimations from the measured R/T data of D-HEBs (ch. 9.5) support the thermal conductivity of 1-5 W/mK. Hence further research and simulations would be necessary if this simulations should be used for quantitative interpretations. The temperature scale has been normalized to the ratio of T/T_c , because this ratio determines the number of quasi-particles which are mainly responsible for the thermal transport. In the following table the corresponding values of T/T_c and $G_{Nb}^{thin\,film}$ can be looked up. [90]:

$T(i)/T_c(i)$	0.22	0.32	0.34	0.54	0.65	0.75	0.86	0.97	1.08	
G_{Nb}^{bulk} [90]	3	20	70	200	300	400	450	500	500	[W/mK]
$G_{Nb}^{thin\,film}$	0.3	2	7	20	30	40	45	50	50	[W/mK]

Table 7: Thermal conductivity G_{Nb} of bulk Nb

Around $T = T_c$ the thermal conductivity converges for the normal conducting and the superconducting states. This model tries to consider the high thermal conductivity of superconductors near to T_c , when the density of states of quasi-particles is still high.

The thermal conductivity G from one element to the other not only depends on the local temperature at element i , but also on the temperature of the adjacent one at $i+1$. At the interface from a normal conducting element to a superconducting element the heat transfer is reduced due to Andreev reflection (ch. 4.4.3). If element i is in the normal conducting state and the adjacent element $i+1$ is in the superconducting state, the thermal conductivity is reduced by the factor Λ to account for the Andreev reflection $G = G/\Lambda$. Λ has been set arbitrarily to 3 in the simulation. In the simulation the effect of the reduced thermal conductivity can be seen in a small step in the temperature profile at the NC/SC interface.

The heat capacity C has been set to a fixed value across the bridge. The heat capacity of Nb drops considerably below the critical temperature. This temperature dependence has a considerable effect on the hot-spot dynamics and the thermal time constant of the mixer. But here only the stationary DC bias characteristics are considered and therefore the temperature dependence of C has been neglected.

The main loop of the simulation program counts the element index i from $i=0$ to the last element. For each element, first the temperature dependent parameters are calculated, and then the heat exchange from and to the adjacent elements. After each loop, the overall HEB resistance is calculated from the temperature profile. The program can simulate constant voltage or constant current bias. The other value is calculated with the HEB resistance, respectively. After a set number of loops (e.g. 200) the element

parameters temperature and critical current etc. are plotted online into a diagram of the bridge. Hence the dynamics of the temperature profile can be observed in slow motion. The changes in this profile are monitored by summing over the squares of the temperature differences of each element. This χ^2 value is an indicator of the stability of the profile. In the case of a stationary profile, this value converges to zero. A minimum χ^2 value can be chosen as an abort condition for the main loop. Then the corresponding current and voltage values are plotted into an I/V diagram and the temperature and critical current profile are saved to a file.

The program user interface has two interleaving loops which can be used for scans. The inner loop scans different bias voltages or currents from a start value to zero. The outer loop triggers these I/V scans for different LO power levels and bath temperatures. For every calculated DC bias point the temperature and critical current profiles are saved to files. The current, voltage and resistance values are summarized in an I/V data file. The files are labelled automatically with the scan parameters for later evaluation. From the I/V scans the dU/dI derivative can be calculated which are in focus of this chapter.

11.5 Simulation results and comparison with measurements

In figure 64 the simulated I/V curve and the corresponding dU/dI derivative are plotted. The bath temperature is set to 4.2 K. The characteristics of the curve, e.g. the two peaks in the dU/dI derivative, are obvious, although the height and position are shifted with respect to the measurement (fig. 63). This is only a rough simulation and quantitative differences can be expected. But as the characteristics are similar, we can now examine the corresponding temperature profiles to investigate the hot-spot thermodynamics. In the beginning of this chapter, the correlation of dR/dT and dU/dI are illuminated. The *first peak* can be found at 0.2 mV in the simulation. If we look at the temperature profile for this value in figure 65 (plot f) we find a very shallow gradient dT/dx at the NC/SC interface at the edge of the hot-spot. It resembles the situation described in figure 61. With an apex temperature near T_c a large dR/dT gradient and HEB response, respectively, can be expected.

The *second peak* in the simulation can be found at 1.4 mV bias voltage. To investigate the rise of the $-dI/dU$ derivative at 1.4 mV, several temperature profiles for bias voltages have been plotted in figure 66. Furthermore the critical temperature profile has been added. The first striking feature is the large hot-spot variation of 25% bridge length. Along the T_c slope towards the heat sinks the temperature profiles runs approximately parallel. Hence only a small change in the overall temperature is needed to move the intersection point of T and T_c from one side of the slope to the other. The result is a large resistance variation dR in relation to a small temperature variation dT . In the simulation, the system stabilizes to nearly identical bias currents of 145 μA at 1.1 mV, and 148 μA at 1.7 mV bias voltage. This results in large corresponding dU/dI and

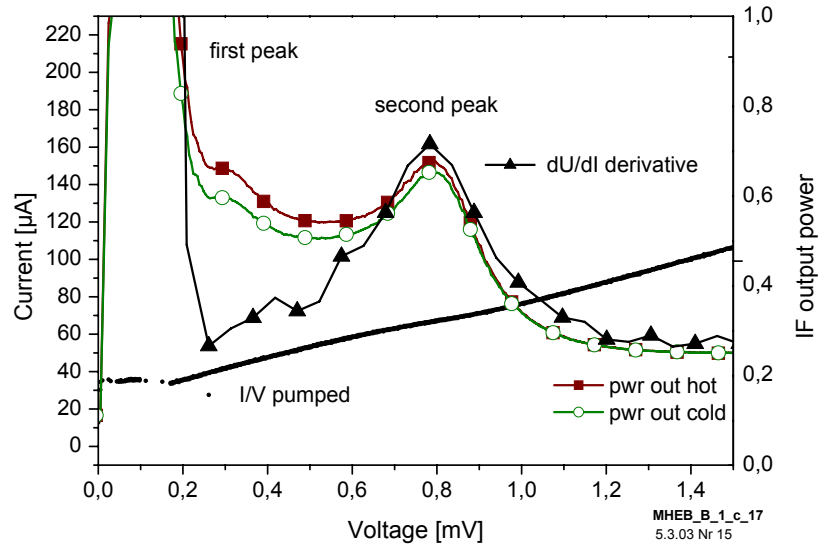


Figure 63: Measured IF output power and dU/dI derivative in relation to the bias voltage. Note the similar maximums at 0.7 mV, which indicate the correlation of the IF output power and the characteristic DC I/V curve.

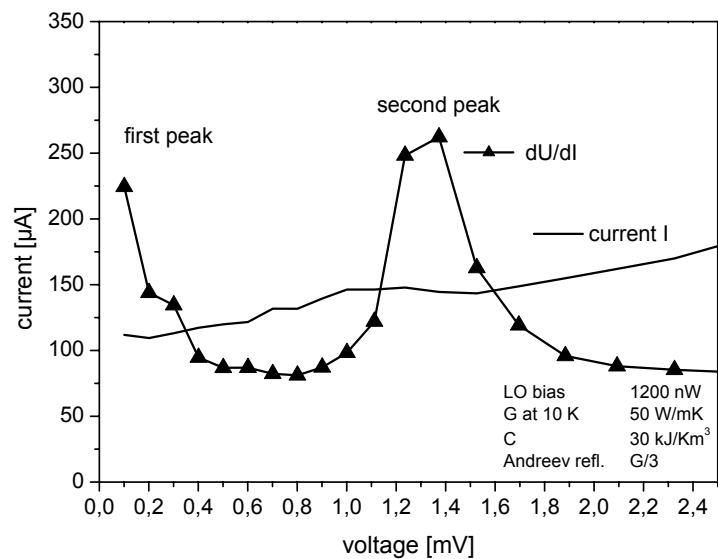


Figure 64: Simulated current-vs-voltage curve and the corresponding dU/dI derivative in relation to the bias voltage. Note the similarities with the measured plot above. The voltage values are higher, but the curve characteristics are matching.

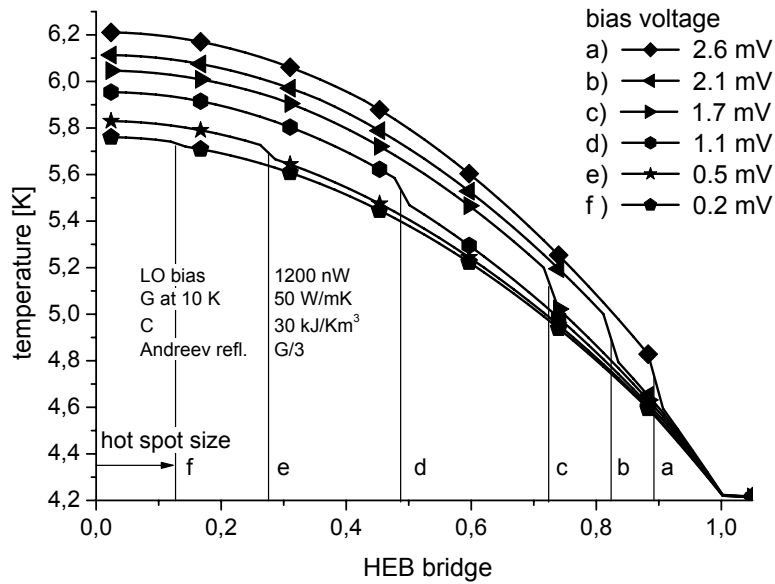


Figure 65: Simple finite element simulation of the hot spot temperature profile inside the bolometer bridge for different bias voltages.

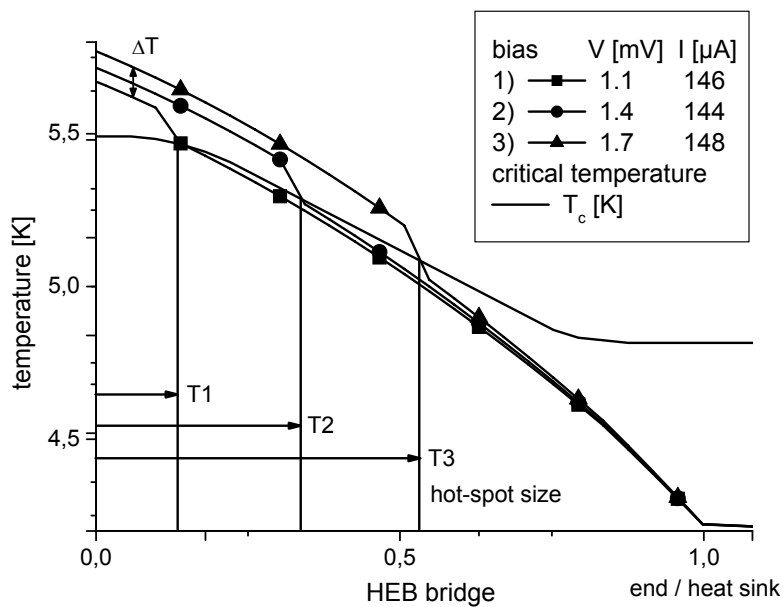


Figure 66: Temperature profiles at bias voltages around the *second peak* and the critical temperature profile. Note the large hot-spot size variation.

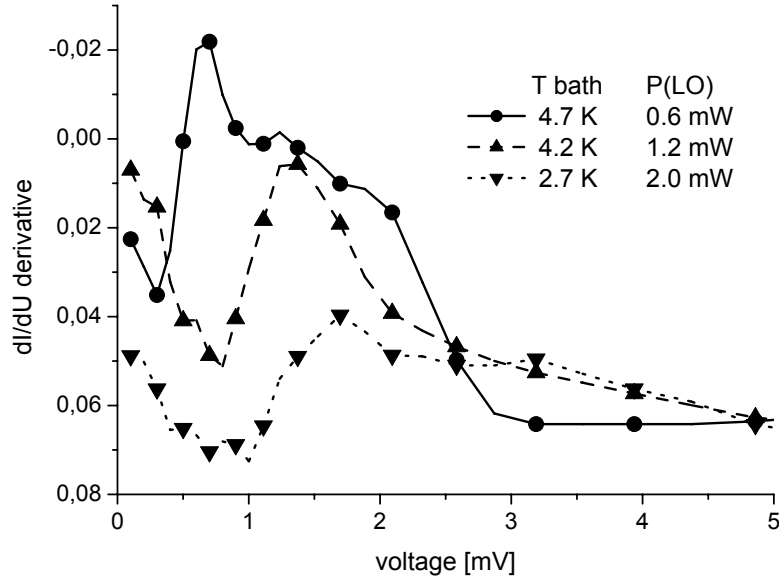


Figure 67: Simulated $-dI/dU$ derivative for different bath temperatures.

dR/dT derivatives, respectively. This scenario could be an explanation of the second dU/dI peak seen in the measurements.

Simulations have also been done at different bath temperatures. In figure 67 the $-dI/dU$ derivatives are plotted for bath temperatures of 2.7, 4.2 and 4.7 K.³ Heterodyne measurements have been done at similar temperatures (fig. 52). At 4.7 K the second peak in the simulation is significantly larger than at 2.7 K. The position of the peak shifts from 0.8 to 1.9 mV bias voltage and more LO power is needed to pump the device. A similar effect has been observed in the heterodyne measurements (fig. 52, ch. 10.2.3). The scenario described in the previous paragraph would be consistent with this observation. If the bath temperature is near to the T_c underneath the heat sinks, a significant effect of a slope in the T_c profile can be expected. If the difference is large, the comparably small T_c variation would have a minor effect and the second peak would become smaller. If we assume that the second peak is related to a certain hot-spot size, then a higher bias voltage is needed to sustain this size at lower bath temperatures than at high ones. Hence when the bath temperature decreases a decrease and shift of position of the second peak towards higher bias voltages can be expected.

In this model the second peak is related to the T_c profile near the heat sinks, which is defined by the proximity effect. This would explain, why the second peak was first measured in devices, where the lift-off process of the heat sinks was improved. The

³ The dI/dU derivative is easier to determine than dU/dI , because dU/dI can become infinite.

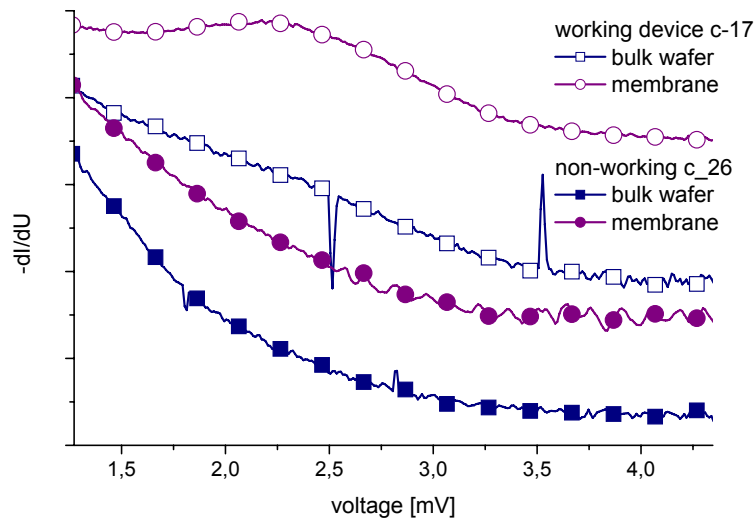


Figure 68: Comparison of the $-dI/dU$ derivative of functional and non-functional devices, measured in liquid helium in a dipstick. While the devices are left on the bulk support wafer, the significant second rise in the curve of the functional device is suppressed.

Au/Nb interface transparency (see [30]) and maybe the lift-off edge profile play an important role here.

However this model does not explain the good performance of these devices. It can be guessed that the IF output power plateau in optimum regions is more likely to turn up in devices with a second peak. As the second peak seems to be related to the proximity effect, it might be an indicator for interface quality at the heat sink and therefore for the diffusion cooling.

11.6 Pre-selection of devices on the basis of dipstick measurements and simulations

It needs to be further investigated whether the characteristic I/V curves can be used for pre-selection of devices. Thus the dipstick curves have been looked upon in more detail. A program plug-in was written for the automated I-versus-V measurement system to calculate and filter the dI/dU derivative of the data. The dI/dU derivative is easier to determine than the dU/dI derivative. Note that these I/V curves are obtained without LO pumping. Its result was that devices which later showed a second peak also showed a slight variation in the dI/dU dipstick curve. In figure 68, device c_17 which

has shown mixing performance, and device c_26 which has not, have been compared. c_26 shows a strictly monotonic increase of $-dI/dU$ with the bias voltage, while the membrane curve of c_17 shows a significant recess at 2.3 mV. A slight recess is also indicated in the bulk wafer curve, but it is difficult to detect. Unfortunately the effect is strongly suppressed, while the devices are still on the bulk support wafer. Hence we cannot make a clear distinction at this point up to now. This leads to the conclusion that more research is necessary to allow reproducible predictions from the dipstick curves.

11.7 Summary and conclusion

A program for simple finite element simulations of diffusion cooled HEBs has been written and successfully tested. The characteristic I/V curves show qualitative agreement with the measured data. Especially the dU/dI derivative, which can be used as an indicator for the HEB mixer response, shows similar characteristics. Changes in the model parameters, e.g. bath temperature or LO power are altering the curves in analogy to their real counterpart. Hence the simulated temperature profiles inside the bridge at different bias conditions have been used to explain the observations in the heterodyne measurements. The absolute values of bias voltage and LO power are larger in the simulation than in the measurements. The reason might be the difficult estimation of the local physical properties inside the bridge, or the insufficiency of the used model for exact quantitative propositions. The latter had not been the motivation for these efforts, anyway.

The dipstick data of devices which showed good heterodyne performance and of ones which did not, have been compared in the focus of the dI/dU derivative. There are indications for a correlation, but more heterodyne data is necessary for reliable distinctions.

12 Waveguide membrane mixer operation at the KOSMA telescope

Measurements with the HEB @KOSMA

5th February 2004, Martin Bruell, data in T_A^*

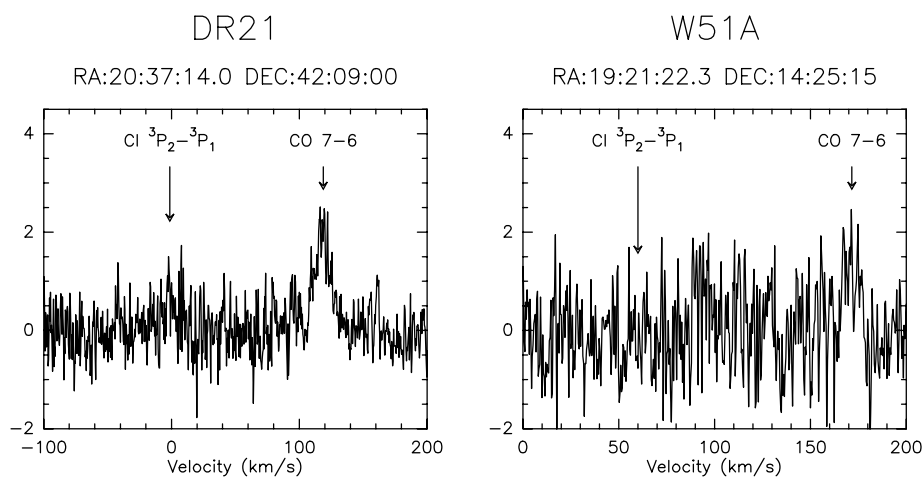


Figure 69: CO 7-6 and CI line in DR21 and W51. (courtesy by M. Brüll [91])

The phonon cooled HEB mixer on a freestanding membrane which has been presented in this work (ch. 10.3) was subsequently mounted into a free channel of an 2×8 pixel dual frequency array receiver [14] at the KOSMA telescope on Gornergrat, Switzerland in mid December 2003. This receiver uses a Sumitomo closed cycle 4K refrigerator. The mixer was operated in parallel to 4 SIS mixers at 800 GHz, so that comparisons in stability and local oscillator power requirements could be made. Allan variance measurements [92] showed similar stability to the SIS channels, and the LO power for the bolometer was about a factor of 5-10 less than that for the SIS mixers. A spectral line of the $J=7-6$ Carbon Monoxide transition towards the galactic sources DR21 and W51 measured with the HEB device in January 2004, is shown in Fig. 69.

13 Conclusion and Outlook

800 GHz HEB mixers on freestanding Silicon Nitride membranes have been fabricated with the fabrication concepts developed in this work and have been successfully tested on the KOSMA telescope at Gornergrat. The 800 GHz design is a proof of concept for the mixers at 1.5 to 2.0 THz we are developing for SOFIA.

An obstacle for the further mixer development have been the continuing problems in the fabrication yield of low noise HEB devices. Hence large effort is spent on HEB research and the improvement of the HEB fabrication. The new membrane concept also offers the unique opportunity to investigate and improve the performance of phonon cooled HEBs on thin membranes.

The heterodyne measurement setup at KOSMA is currently expanded for measurements at 1-3 THz with an Far InfraRed (FIR) laser local oscillator. The two halves of a Silicon micro-machined corrugated horn for 1.85 THz have been fabricated with laser induced etching at the University of Arizona and are on their way for their final assembly at KOSMA.

With the recent acquisition of an Inductively Coupled Plasma (ICP) etcher at KOSMA, new ways for the production of substrate membranes and waveguide structures have become feasible. In this context further improvements in the presented fabrication processes are to be expected.

Appendix

A Electro/thermal feedback

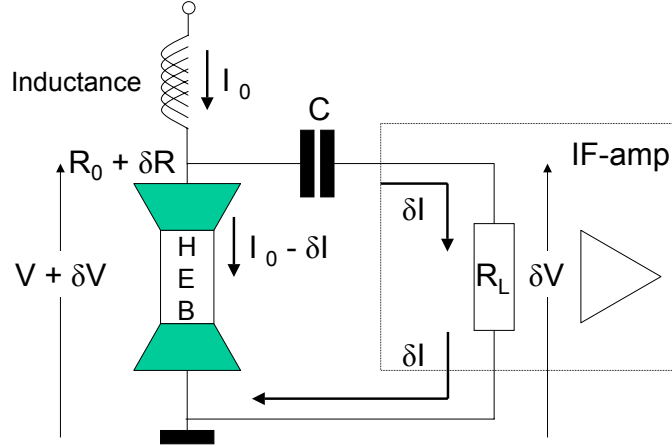


Figure 70: HEB-circuit

Chapter 4.5 introduces the *self-heating* and the *electro/thermal feedback*. The *self-heating* affects the dissipated power which again affects the HEB temperature. In the lumped element model by Ekström [43] this effect is considered in form of a change in the effective cooling. It has been expanded here to the case of constant voltage biasing.

The HEB responds to power variations:

$$dT = \frac{dP}{G} \quad (85)$$

G is the thermal conductivity towards the cold reservoir in the lumped element model. Voltage and current at the HEB are changed, when the resistance of the HEB changes:

$$V + dV = (I - dI)(R_0 + dR) \quad (86)$$

This again changes the dissipated power:

$$P + dP = (V + dV)(I - dI) = P + IdV - VdI - dIdV \quad (87)$$

$$dP \approx IdV - VdI = IdV - IRdI \quad (\text{neg. } dIdV) \quad (88)$$

Both equations are combined and solved for two simple cases $dV = 0$ and $dI = 0$, respectively.

Constant current bias $dI = 0$

$$dP = IdV \quad (89)$$

$$dV = I(R_0 + dR) - V \quad (90)$$

$$\Rightarrow dP = I^2(R_0 + dR) - VI = I^2 dR \quad (91)$$

The additional power dissipation can be interpreted as reduction in the efficient cooling (with 85):

$$G_{eff}^{cI} = G_\theta - I^2 \frac{dR}{dT} \quad (92)$$

Constant voltage bias $dV = 0$

$$dP = -VdI \quad (93)$$

$$dI = \frac{-V}{R_0 + dR} + I \quad (94)$$

$$\Rightarrow dP = V \frac{V}{R_0 + dR} - VI \quad (95)$$

$$\text{with } \frac{V}{R_0} \frac{1}{1 + \frac{dR}{R_0}} \approx \frac{V}{R_0} \left(1 - \frac{dR}{R_0}\right) \quad (96)$$

$$\Rightarrow dP \approx \frac{V^2}{R_0} - VI - \frac{V^2}{R_0^2} dR = -\frac{V^2}{R_0^2} dR \quad (97)$$

Hence the power dissipation is reduced and, in contrast to 92, the efficient cooling increases:

$$G_{eff}^{cV} = G_\theta + \frac{V^2}{R_0^2} \frac{dR}{dT} \quad (98)$$

IF power To detect the IF oscillations, an IF amplifier with the load resistance R_L is capacitively coupled to the HEB (fig. 70). The voltage at this load is:

$$dV = dIR_L \quad (99)$$

This can be inserted into 87:

$$dP = IdV - VdI = \frac{V}{R_0} dV - V \frac{dV}{R_L} = VdV \left(\frac{1}{R_0} - \frac{1}{R_L} \right) \quad (100)$$

$$= VdV \left(\frac{R_L - R_0}{R_L R_0} \right) \quad (101)$$

dV can be deduced from 93:

$$V + dV = IR_0 + IdR - R_0 dI - dIdR \quad (102)$$

$$\Rightarrow dV = IdR - R_0 \frac{dV}{R_L} - dIdR \quad (\text{negl. } dIdR) \quad (103)$$

$$\Rightarrow dV \approx \frac{IdR}{1 + \frac{R_0}{R_L}} = \frac{IR_L dR}{R_L + R_0} \quad (104)$$

and inserted into 100 we get the effect of the *el/th feedback* on the heat dissipation and the effective cooling, respectively:

$$dP^{IF} = V \frac{IR_L dR}{R_L + R_0} \frac{R_L - R_0}{R_L R_0} = I^2 dR \frac{R_L - R_0}{R_L + R_0} \quad (105)$$

$$G_{eff}^{IF} = G_{\Theta} - I^2 \frac{R_L - R_0}{R_L + R_0} \frac{dR}{dT} \quad (106)$$

In the case of $R_L > R_0$ we have positive feedback with reduced effective cooling, similar to the constant bias current case (eq. 92). Hence the bolometer is slowed down for the IF oscillations and the roll-off frequency is reduced. If R_L is smaller than R_0 the algebraic sign of the equation above changes and less heat is dissipated. With this negative feedback the effective cooling is enhanced and therefore the IF bandwidth increases.

B Mixer Gain

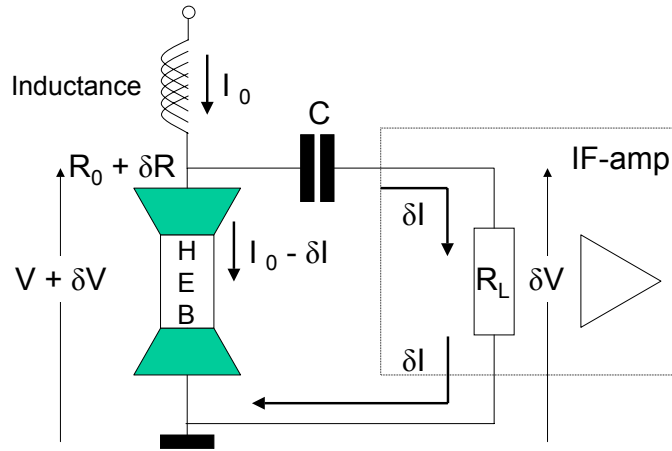


Figure 71: HEB-circuit

In chapter 4 the bolometric principle, the change of the bolometer resistance due to changes and fluctuations in the incoming power, has been deduced:

$$\delta R = (C_{RF sig} \delta P_{RF sig} + C_{DC} \delta P_{DC}) \frac{1}{\sqrt{1 + (2\pi f \tau_{\theta})^2}} \quad (107)$$

The power oscillation of the IF frequency in the heterodyne mixing is determined by:

$$\delta P_{RF\ sig} = 2\sqrt{P_{LO}P_{RF\ sig}} \quad (108)$$

According to [43] the thermal efficiency $C_{DC} = \frac{dR}{dP_{DC}}$ in 107 can be determined from the derivatives $d(V/I)$ and $d(VI)$ in the the pumped I/V curve.

$$dR = \frac{V_0 + dV}{I_0 + dI} - \frac{V_0}{I_0} \approx \frac{V_0}{I_0} \frac{dI}{I_0} \left(\frac{dV}{dI} \frac{I_0}{V_0} - 1 \right) \quad (109)$$

$$dP = (V_0 + dV)(I_0 + dI) - V_0I_0 \approx V_0dI \left(\frac{dV}{dI} \frac{I_0}{V_0} + 1 \right) \quad (110)$$

Introducing the differential resistance $R_D = (dV/dI)_{DC}$ and the resistance $V_0/I_0 = R_0$ at the bias point into 109, C_{DC} can be determined:

$$C_{DC} = \frac{dR}{dP_{DC}} = \frac{d(V/I)}{d(VI)} = \frac{1}{I_0^2} \left(\frac{\frac{dV}{dI} \frac{I_0}{V_0} - 1}{\frac{dV}{dI} \frac{I_0}{V_0} + 1} \right) \quad (111)$$

$$= \frac{1}{I_0^2} \frac{R_D/R_0 - 1}{R_D/R_0 + 1} = \frac{1}{I_0^2} \frac{R_D - R_0}{R_D + R_0} \quad (112)$$

The DC heating is the product of voltage at the bolometer and the bias current I_0 minus the IF current δI running through the IF load resistance R_L . Here we are only interested in the power fluctuations, so the constant terms are dropped.

$$P_{DC} = (I_0 - \delta I)(V_0 + \delta V) = I_0V_0 - \delta IV_0 + I_0\delta V - \delta I\delta V \quad (113)$$

$$\Rightarrow \delta P_{DC} = I_0\delta V - V_0\delta I \quad (114)$$

$\delta I\delta V$ is assumed to be small and has been neglected. Note that the coupling capacitor blocks I_0 so the voltage across the load resistance is only $\delta V = R_L\delta I$. With $V = R_0I_0$ for the static system we can eliminate the voltages in the above equation.

$$\delta P_{DC} = I_0(R_L\delta I) - \delta I(I_0R_0) = I_0\delta I(R_L - R_0) \quad (115)$$

Now we can calculate the resistance variations of the bolometer:

$$\delta R = (I_0\delta I C_{DC}(R_L - R_0) + C_{RF}2\sqrt{P_{LO}P_{RF\ sig}}) \frac{1}{\sqrt{1 + (2\pi f \tau_{mix})^2}} \quad (116)$$

This resistance variation causes the changes in the flowing currents and the voltage variation δV . As mentioned before the voltage at the load resistance is:

$$\delta V = R_L\delta I \quad (117)$$

The current running through the bolometer is reduced by δI . The voltage across the bolometer is generated by this reduced current and the actual resistance $R = R_0 + \delta R$. Similar to 113 we can calculate the total voltage and the voltage variations at the bolometer:

$$V + \delta V = (R_0 + \delta R)(I_0 - \delta I) = R_0 I_0 - R_0 \delta I + I_0 \delta R - \delta R \delta I \quad (118)$$

$$\Rightarrow \delta V = -R_0 \delta I + I_0 \delta R \quad (119)$$

$V = R_0 I_0$ has been subtracted and $\delta R \delta I$ has been neglected. δV at the bolometer and at the load resistance are equal because of the coupling capacitor.

$$I_0 \delta R - R_0 \delta I = R_L \delta I \quad (120)$$

$$\Leftrightarrow \delta I (R_L + R_0) = I_0 \delta R \quad (121)$$

Now we can determine the current variation from the resistance variation by inserting δR from 116 into the equation above.

$$\delta I (R_L + R_0) = (\delta I I_0^2 C_{DC} (R_L - R_0) + I_0 C_{RF} 2 \sqrt{P_{LO} P_{RF sig}}) \frac{1}{\sqrt{1 + (2\pi f \tau_{mix})^2}} \quad (122)$$

$$\Leftrightarrow \delta I = \frac{I_0 C_{RF} 2 \sqrt{P_{LO} P_{RF sig}}}{(R_L + R_0) (1 - I_0^2 C_{DC} \frac{R_L - R_0}{R_L + R_0})} \frac{1}{\sqrt{1 + (2\pi f \tau_{mix})^2}} \quad (123)$$

δI is coupled into the amplifier load and is generating the IF signal which we can detect subsequently. With $\delta P_{IF} = 1/2 \delta I^2 R_L$ the conversion gain η between the RF input power and the IF output power can be calculated.

$$\eta = \frac{P_{IF}}{P_{RF sig}} = \frac{2 I_0^2 C_{RF}^2 P_{LO} R_L}{(R_L + R_0)^2 (1 - I_0^2 C_{DC} \frac{R_L - R_0}{R_L + R_0})^2} \frac{1}{(1 + (2\pi f \tau_{mix})^2)} \quad (124)$$

In this equation the *electro/thermal feedback* is considered in the gain magnitude as well as in gain roll-off frequency. Note, that:

$$\tau_{mix} = \frac{\tau_\theta}{1 - \frac{I_{bias}^2}{G_\theta} \frac{dR}{dT} \frac{R_L - R_0}{R_L + R_0}} \quad (125)$$

C Fabrication and measurement data base for advanced process development

C.1 Data Base Concept

The HEB and SIS fabrication at KOSMA is based on long term experience in device fabrication. The new approaches with micro-machining presented here, and the implementation of the superconducting devices demand a large number of different experiments. The traditional way of writing chronological process report sheets thus has become time consuming and difficult to manage. Therefore a new database tool has been developed which simplifies and supports the process design and documentation.

Every complex process chain can be divided into smaller process parts. Normally the number of these smaller sections is limited and they are often repeated inside the chain with different process parameters. In analogy to "LEGO®" a concept was developed where "process step bricks", chosen from a pull down menu, can be set on top of each other on the computer screen. Each "brick" is a virtual data object in an Access® data base representing a process step, e.g. the sputtering process for Niobium or a UV lithography step. It contains all the necessary information to describe its general procedure sub-step by sub-step, and the according set points. When this particular process step has been gone through, the actual describing parameters of the process are filed into this object to enable later evaluation and quality management for the complete process chain. The whole concept is embedded into the project hierarchy of the data base Process2 (see fig 72) where every produced batch of devices is filed in, assigned to certain types of projects. A batch in the KOSMA production represents one wafer with its devices. The main projects are, for example, FIRST, HEB, MHEB and so on. Every batch is separated into three branches to link it with :

1. the parameters of the devices of this batch (left),
2. the device geometries defined by the masks (bottom),
3. the process chain and its parameters (right).

The three branches follow a linear structure down to the basic sub steps or mask parameters. This keeps the data base structure lean and comprehensible, despite the power and flexibility of the system. The automated measurement and device characterization software described in ch. 9 uses this hierarchy to automatically link the gathered data to the corresponding batch and its process. It makes the feedback to the process chain very comfortable, secure and definite.

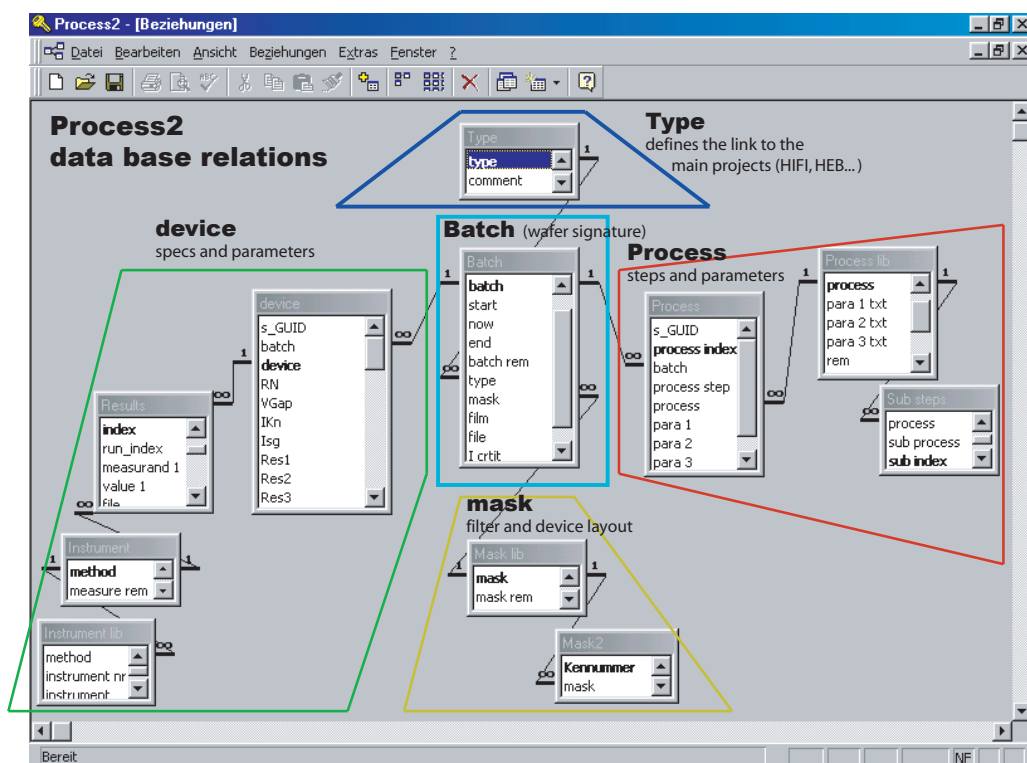


Figure 72: Data base concept overview.

C.2 Data Base realization

The data base Process2 was programmed in Access97 by Microsoft. Figure 73 shows a typical example of the data base forms to design a process, and the resulting recipe which is printed out to take along into the clean room. In the form in the foreground the pull down menu is seen from which the needed steps can be chosen. A double click leads into the corresponding process library entry with the whole recipe and its sub steps. Each line in the process form presents the three most important parameters and the actual values that turned up during the production of this particular batch. This allows to check, and if necessary change, these parameters in the overview of the process. A special data base structure is needed to combine the recipes which are not altered from batch to batch, and the parameters which change from batch to batch. The data base consists of a list of batch entries and a library list of the available processes. The two lists are linked with a third list where every entry represents a cross reference between a batch and a process step. This way every batch can be linked with an endless number of process steps. The same process step can also appear several times in the process flow. The chronological order of the steps is defined by a running index. The values of the three parameters which are unique to every batch and process step, are also filed in the cross reference list. The form seen in the figure selects all the steps related to the particular batch, and presents them together with these parameters. The Access program also supervises the new entries and blocks unreferenced ones. In the background of the picture an inactive form with measured device parameters is seen.

D Micro Production Line on the Hannover Fair Industry

The Klocke Nanotechnik micro assembly stage and its application at KOSMA is unique in the field of micro mechanics. There are only few companies which are able to assemble micro-parts with micrometer precision for real products. Several references on international technology fairs and industry publications led to the invitation by the Hanover Messe GmbH and the Verband Deutscher Anlagen- und Maschinenbau (VDMA[93]) to participate on the Hannover Messe Industrie 2003(HMI[94]). The task was to set up a micro production line on the fair for live assembly of micro parts which can be handed out to the visitors. A give-away product was developed on the basis of the KOSMA Terahertz detectors and successfully built in line right on the fair ground, implementing the different specializations of the project partners:

- 3D MID laser systems (LPKF Laser and Electronics AG, Suhl)
- Nanorobotic systems (Klocke Nanotechnik, Aachen)

The screenshot shows a software interface with a menu bar (Datei, Bearbeiten, Ansicht, Einfügen, Format, Datengänge, Extras, Fenster) and a toolbar. Below the menu is a control panel with fields for 'batch' (MHEB_B_1), 'type' (MHEB_B), 'Process', 'Results', and 'Data Disp'. A table lists process parameters:

device	RN	p	dose	p d	REM	bridge	width	R Sheet	I crit	Ityst	Ratio I	status	Com
MHEB_B_1_b_19	190,7	260	170	500				0	0	0,4	0	open ?	
MHEB_B_1_b_20	1619,35	260	150	500				0	1,2	0,4	3	no comment	
MHEB_B_1_b_21	18,28	260	150	500				0	221,6	93,1	2,4	0.06K_0.15K	

Below the table is a 'Process' window showing a detailed recipe for 'Au Pad dampfen ohne Kühlung'. It includes a table of steps:

step	rem	process	para 1 txt	para 1	para 2 txt	para 2	para 3 txt	para 3
5		wafer clean						
6	Au cross	litho 7212	exposure	0.25	develop	0:30	picture	
10		load sputter	main chamber pre					
11		O2 clean	flow		pressure		time	
12	Au cross	Nb 75 W low s	thickness	20	time	1:12	pressure	1.30
13		Nb 75 W low s	0.275 nm/s		time	3:30	cool step	0.3:
14	direkt US	Nb 75W	0.325 nm/s		time	4:00	Swap	no
16	Blenden clean 100W (nicht e	NbTi			pressure	3Pa	time	10.00
17	HEB film	O2 clean						
18		O2 precond			pressure		time	
19	HEB film	open step			time	0:37	pressure	1.30
20		RF Au <-> Nb	0.25 nm/s		pressure	0.6 mBar	gas	Ar
21		RIE C CL2 F2			time	0:45	cool step	0.3:
22	bake ohne Vakuum auf HP	RIE NF3			thickness	220 nm	spin	4000
23	neuer Versuch	RT Box			thickness	220 nm	spin	4000
25	Au Pad	saw			layer	P_B_1	dose rem/pc:	13/14.6
26		Si CuNO3 Wisc			develop	4.00		
27	neuer Versuch	SIN etch 100pB	2.78 nm/s		thickness	220 nm	spin	4000
28	Au Pad	SIN etch 200pB			layer	P_B_1b	dose rem/pc:	13/14.6
--		SiO2 150 W	25 nm/min					

MHEB_B_1

45 load sputter main chamber press.

1	le = 10, IG1	Hauptkammerdruck
10		Turbo Vollast, Panel Teillast
11	Kathode, Substrat, Ätzst.	Kühlung
12		Gas auf
13		Schmetterling zu
14		vent load lock
15		load pellet
16		RF Schirm hochziehen, fixieren
17		Gas zu, Kammer zu
20		Foreline off, rough on
21	< 6 E-2 mBar	rough off, Foreline on
22		Schmetterling auf
23	le = 1, IG2	Vorkammerdruck
24	< 5 E-6 mBar	RF clean

46 Ar clean 6W

	flow/PWR	20
	pressure	3
	time	1:00

1	20 sccm, 3 Pa	Ar
2	6 W, 1:00	RF
3	5:00	wait, Kühlung Ätzstation aus
4	le = 1, IG2 on	Vorkammerdruck
5	4 E-6 mBar	load main chamber
6	2:00	wait after load main ch.

47 Nb 75 W low s 0.275 nm/s

RF Filter	thickness	80
	time	4:51
	pressure	

1	200 sccm	flow
2	1.34 Pa	presputter press. (2.8.01)
3	300 W, 3:00	presputter
4	75 W (1.30 Pa)	sputter (ab 2.8.01)

48 Au 50 W 0.885 nm/s

	thickness	300
	time	5:38
	cool step	2 @2:00

1	50 W, 1.75 Pa, 1:00	pre sputter
2	50 W, 1.75 Pa	sputter

11. Aug. 03 MHEB_B_1 Seite 8 von 25

Figure 73: Data base form and a typical page from a corresponding recipe.

- Base translation stages for the Nanorobotic system (LPKF Motion and Control GmbH, Suhl)
- Micro Adhesive Bonding Technology (FHG-IFAM, Berlin)
- Process Control Software (SH-Systems, Aachen)
- Metrology, Inspection Systems (FRT, Bergisch Gladbach)
- Terahertz Detector Technology (KOSMA, Köln)

A new setup for the HMI 2004 is planned, integrating the company IBM, Mainz.

References

- [1] Wright *et al.*, “Preliminary spectral observations of the galaxy with a 7° beam by the cosmic background explorer (COBE,” in *The Astrophysical Journal*, November 1991.
- [2] N. Schneider, R. Simon, C. Kramer, J. Stutzki, and G. Winnewisser, “Submm- and far-observations of the s106 photon dominated region,” *The Physics and Chemistry of the Interstellar Medium*, 1998.
- [3] S. Lord, “A new software tool for computing the earth’s atmospheric transmission of near- and far infrared radiation.” Nasa Technical Memorandum 103957, Dec. 1992.
- [4] M. C. Wiedner, G. Schmidt, U. U. Graf, C. E. Honingh, K. Jacobs, J. Stutzki, R. Güsten, K. M. Menten, and P. Schilke, “1.4 THz receiver,” in *4th Cologne-Bonn-Zermatt-Symposium*, September 2003.
- [5] “SOFIA homepage :<http://sofia.arc.nasa.gov/>.”
- [6] Kölner Observatorium für SubMM Astronomie Homepage:, “<http://www.ph1.uni-koeln.de/>.”
- [7] R. Güsten *et al.*, “GREAT the first-generation german heterodyne receiver,” in *SPIE Airborne Telescope Systems*, vol. 4014, pp. 23–30, 2000.
- [8] E. A. Michael *et al.*, “SOFIA Terahertz Array Receiver STAR,” in *SPIE Airborne Telescope Systems*, vol. 4014, pp. 109–115, 2000.
- [9] R. A. Shafer, S. H. Moseley, P. A. Ade, D. J. Benford, G. Bjoraker, E. Dwek, D. A. Neufeld, F. Pajot, T. G. Phillips, and G. J. Stacey, “Submillimeter and far-infrared experiment (safire): A pi class instrument for sofia,” in *SPIE Astronomical Telescopes and Instrumentation*, March 2000.
- [10] A. I. Harris, T. D. Jaffe, J. Stutzki, and R. Genzel, “-,” *Int. J. InfraRed Millimeter waves*, vol. 8, p. 857, 1987.
- [11] P. Khosropanah, S. Bedorf, S. Cherednichenko, V. Drakinskiy, K. Jacobs, H. Merckel, and E. Kollberg, “Fabrication and noise measurement of NbTiN hot electron bolometer heterodyne mixers at THz frequencies,” in *Proc. 14th Int’l. Symp. on Space THz Techn*, 2003.
- [12] J. J. A. Baselmans, M. Hajenius, J. R. Gao, T. M. Klapwijk, P. A. J. de Korte, B. Voronov, and G. Goltsman, “Doubling of sensitivity and bandwidth in phonon cooled hot electron bolometer mixers,” *Appl. Phys. Lett.*, vol. 84, no. 11, 2004.

- [13] D. Marrone, J. Battat, F. Bensch, R. Blundell, T. Hunter, D. Loudkov, S. Paine, C. Y. Tong, D. Meledin, H. Gibson, S. Radford, and M. Diaz, "A map of OMC-1 in CO J=9-8 (1.037 THz)," *American Astronomical Society Meeting 203*, 12 2003.
- [14] U. U. Graf, S. Heyminck, E. A. Michael, S. Stanko, C. E. Honingh, K. Jacobs, and J. Stutzki, "SMART: The KOSMA Sub-Millimeter Array Receiver for Two Frequencies," in *Proceedings of the 13th International Symposium on Space Terahertz Technology*, (Boston), 2002.
- [15] S. Glenz, M. Justen, P. Pütz, R. Teipen, T. Tils, C. Honingh, and K. Jacobs, "Broadband nbtin based sis mixers for hifi band 2," *Proc. 27th Int. Conf. Infrared and Millimeter waves*, pp. 257–258, 2002.
- [16] M. Justen, T. Tils, S. Glenz, P. Pütz, M. Schultz, R. Teipen, C. Honingh, and K. Jacobs, "Broadband NbTiN based SIS mixer for Band 2 of the HIFI Instrument for the Herschel spacecraft," in *European Con. on Apl. Superconductivity*, 2003.
- [17] C. Honingh, "Low noise broadband fixed tuned SIS waveguide mixers at 660 and 800 GHz," *IEEE Trans. Appl. Supercond.*, vol. 7, pp. 2582–2586, Juni 1997.
- [18] P. Santhanam and D. Prober, "Inelastic electron scattering mechanisms in clean aluminium films," *Phys.Rev. B*, vol. 24, no. 6, 1984.
- [19] E. Gershenzon, G. Gol'tsman, A. Lyuk'kin, A. Semenov, and A. Sergeev, "Electron-phonon interaction in ultrathin Nb films," *Journal of Exp. and Theor. Phys.*, vol. 70, no. 3, p. 505, 1990.
- [20] C. Kittel, *Einführung in die Festkörperphysik*. München: R. Oldenbourg Verlag, 11 ed., 1996.
- [21] D. Prober, "Superconducting terahertz mixer using a transition-edge microbolometer," *Appl. Phys. Lett.*, vol. 62, pp. 2119–2121, April 1993.
- [22] W.J.Skocpol, M. Beasley, and M. Tinkham, "Self-heating hotspots in superconducting thin-film microbridges," *J. Appl. Phys.*, vol. 45, p. 4054, September 1974.
- [23] D. W. Floet, *Hotspot Mixing in THz Niobium Superconducting Hot Electron Bolometer Mixers*. PhD thesis, Technische Universiteit Delft, 2001.
- [24] D. W. Floet, E. Miedema, T. Klapwijk, and J. Gao, "Hotspot mixing: a new framework for heterodyne mixing in superconducting hot electron bolometers," *Appl. Phys. Lett.*, vol. 74, p. 433, 1999.

- [25] Y. Gousev, G. Golt'sman, A. Semenov, E. Gershenzon, R. Nebosis, M. Heusinger, and K. Renk, "Broadband ultrafast superconducting NbN detector for electromagnetic radiation," *J. Appl. Phys.*, vol. 75, no. 7, pp. 3695–3697, 1994.
- [26] G. Golt'sman, M. Finkel, Y. Vachtomin, S. Antipov, V. Drakinskiy, N. Kaurova, and B. Voronov, "Gain bandwidth and noise temperature of NbTiN HEB mixer," *In Proc. 14th Int'l. Symp. Space THz Techn.*, 2004.
- [27] C. Tong, J. Stern, K. Megerian, H. LeDuc, T. Sridharan, H. Gibson, and R. Blundell, "A low-noise nbtin hot electron bolometer mixer," *Proc. 12th Int'l. Symp. on Space THz Techn.*, pp. 253–261, 2001.
- [28] B. Karasik, W. McGrath, and R. Wyss, "Optimal choice of material for HEB superconducting mixers," *IEEE Trans. Appl. Supercond.*, vol. 9, Juni 1999.
- [29] A. Skalare, W. McGrath, B. Bumble, and H. LeDuc, "Tantalum hot-electron bolometers for low-noise heterodyne receivers," *Proc. 12th Int'l. Symp. Space THz Techn.*, pp. 245–248, 2002.
- [30] J. Stodolka, *Fabrication und Analyse supraleitender diffusionsgekühlter Hot-Electron-Bolometer als Terahertz-Heterodyn timer*. PhD thesis, Universität zu Köln, 2002.
- [31] P. Khosropanah, *NbN and NbTiN Hot Electron Bolometer THz Mixers*. PhD thesis, Chalmers University of Technology, 2003.
- [32] A. D. Semenov, G. N. Gol'tsman, and R. Sobolewski, "Hot-electron effect in superconductors and its applications for radiation sensors - progress in coherent detection methods," *Supercond. Sci. Technol.*, vol. 15, 2001.
- [33] S. Cherednichenko, P. Yagoubov, K. Il'in, G. Gol'tsman, and E. Gershenzon, "Large bandwidth of phonon-cooled bolometer mixers on sapphire substrates," *8th Int. Symp. on Space Terahertz Technology, Harvard University*, 1997.
- [34] A. Sergeev and M. Y. Reizer, "Photoresponse mechanisms of thin superconducting films and superconducting detectors," *Int. J. Mod. Phys. B*, vol. 10, no. 6, 1996.
- [35] S. Cherednichenko, M. Kroug, P. Khosropanah, A. Adam, H. Merkel, and E. Kollberg, "A broadband terahertz heterodyne receiver with an NbN HEB mixer," *Proc. 13th Int'l. Symp. Space THz Techn.*, pp. 85–94, 2002.
- [36] S. Bedorf, *open titel*. PhD thesis, Universität Köln, to be published.

- [37] M. Frommberger, P. Sabon, M. Schicke, and K. Schuster, "Characterization of NbN thin films produced on quartz substrates using MgO seed layers for phonon cooled hot-electron bolometer devices," *Proc. 12th Int'l. Symp. Space THz Techn.*, 2001.
- [38] P. Burke, R. J. Schoelkopf, D. Prober, A. Skalare, W. McGrath, B. Bumble, and H. LeDuc, "Length scaling of bandwidth and noise in hot-electron superconducting mixers," *Appl. Phys. Lett.*, vol. 68, p. 23, 1996.
- [39] W. McGrath, "Hot-electron bolometer mixers for submillimeter wavelength: An overview of recent developments," *Proc. 6th Int'l. Symp. Space THz Techn.*, pp. 216–228, 1995.
- [40] P. J. Burke, *High Frequency Electron Dynamics in Thin Superconductors and Applications to Fast, Sensitive THz Detectors*. PhD thesis, University of Yale, Dezember 1997.
- [41] I. Didschuns, *Supraleitung in Zinnschichten auf InSb*. PhD thesis, Freie Universität Berlin, August 2000.
- [42] H. Ekström and B. Karasik, "Electron temperature fluctuation noise in hot-electron superconducting mixers," *Appl. Phys. Lett.*, vol. 66, no. 23, 1995.
- [43] H. Ekström, B. Karasik, E. Kollberg, and S. Yngvesson, "Investigation of superconducting hot electron mixers," *Proc. 5th Int'l. Symp. on Space Terahertz Technology, University of Michigan*, pp. 169–188, 1994.
- [44] H. Ekström, E. K. P. Yagoubov, G. Gol'tsman, E. Gershenzon, and S. Yngvesson, "Gain and noise bandwidth of NbN hot-electron bolometer mixers," *Appl. Phys. Lett.*, vol. 70, no. 24, 1997.
- [45] P. H. Siegel, R. P. Smith, M. Gaidis, S. Martin, J. Podosek, and U. Zimmermann, "2.5 THz GaAs monolithic membrane-diode mixer," in *Proc. 9th Int'l. Symp. on Space THz Techn*, p. 147, 1998.
- [46] J. Bruston, S. Martin, A. Maestrini, E. Schlecht, P. Smith, and I. Mehdi, "The frameless membrane: A novel technology for THz circuits," in *Int. Symp. on Space Terahertz Technology*, (Ann Arbor, MI), p. 277, 2000.
- [47] J. W. Kooi, J. Pety, B. Bumble, and C. K. Walker, "A 850 ghz waveguide receiver employing a Niobium SIS junction fabricated on a $1\mu\text{m}$ Si_3N_4 membrane," *IEEE Trans. on Microwave theo. and tech.*, vol. 46, February 1998.
- [48] R. Bass, *Diffusion-Cooled Hot-Electron Bolometers on Beam Lead Chips for a 585GHz Receiver*. PhD thesis, University of Virginia, 2003.

- [49] N. Ashcroft and N. Mermin, *Solid State Physics*. Hartcourt Brace College Publishers, 1976.
- [50] W. Holmes, “Measurements of thermal transport in low stress silicon nitride films,” *Appl. Phys. Lett.*, vol. 72, pp. 2250–2252, may 1998.
- [51] M. M. Leivo and J. P. Pekola, “Thermal characteristics of silicon nitride membranes at sub-Kelvin temperatures,” *Appl. Phys. Lett.*, vol. 72, pp. 1305–1307, march 1998.
- [52] J. Baubert, H. Merkel, M. Salez, and P. Khosropanah, “A hot-spot model for membrane-based heb mixer,” in *14th Int. Symp. on Space THz Technology*, (Tucson, Arizona, USA), April 2003.
- [53] Technische Universität, München, “private communication.”
- [54] “Berkeley Microfabrication Laboratory, University of California, Berkeley.”
- [55] “Aremco Products Inc.,” New York, USA Ossining.
- [56] X. Elwenspoek and H. V. Jansen, *Silicon Micromachining*. Cambridge University Press, ?
- [57] “W Wax by Apiezon, Manchester UK.”
- [58] V. Lehmann, “private communication.”
- [59] V. Lehmann, W. Hönlein, H. Reisinger, A. Spitzer, H. Wendt, and J. Willer, “A new capacitor technology based on porous silicon,” *Solid State Technology*, p. 99, 1995.
- [60] P. P. Muñoz, *open titel*. PhD thesis, Universität zu Köln, to be published.
- [61] Shipley AZ-series resist.
- [62] “Stycast, Emerson Cuming, USA.”
- [63] O. Hachenberg and B. Vowinkel, *Technische Grundlagen der Radioastronomie*. B.I. Wissenschaftsverlag, 1982.
- [64] “CST Computer Simulation Technology, MICROWAVE STUDIO 2, darmstadt, germany.”
- [65] “SU-8 photo resist, EPON, USA.”
- [66] H. M. Picket, J. Hardy, and J. Farhoomad, “Characterization of a dual-mode horn for submillimeter wavelengths,” *IEEE Trans. on Microwave Theory and Tech.*, vol. 32 (8), 1984.

- [67] B. Thomas and A. Mac, "Design of corrugated conical horns," *IEEE Trans. Ant. and Prob.*, vol. AP26, no. 2, p. 367, 1978.
- [68] M. Brandt, J. Stodolka, C. Honingh, and K. Jacobs, "Micromechanical waveguide mounts for HEB THz mixers," in *Proc. Far-IR, Sub-MM and MM Detector Techn. Workshop*, 2002.
- [69] T. Crowe, "private communication."
- [70] C. Walker, "University of Arizona, private communication."
- [71] "Micro-Tec, Dortmund, Germany."
- [72] Radiometer Physics GmbH, Meckenheim, Germany.
- [73] Dr. Voker Klocke Nanotechnology, Aachen Germany.
- [74] T. Tils, *open*. PhD thesis, Universität zu Köln, to be published.
- [75] A. V. Gurevich and R. G. Mints, "Self-heating in normal metals and superconductors," *Rev. Mod. Physics*, vol. 59, pp. 941–999, 1987.
- [76] Y. Zhuang, D. Gu, and S. Yngveeson, "Bistability in nbn heb mixer devices," in *14th Intern. Symp. Space THz Technology, Tucson, Az.*, (University of Massachusetts, MA, USA), 2003.
- [77] Lakeshore Cryotronics, Westerville, OH, USA.
- [78] L. J. van der Pauw, *A method of measuring specific Resistivity and Hall effect of discs of arbitrary shape*, vol. 13. Philips Res. Repts., 1958.
- [79] J. R. Gao, "Superconducting transition and heterodyne performance at 730 ghz of a diffusion cooled Nb hot electron bolometer mixer," *In Proc. 8th Int'l. Symp. Space THz Techn.*, pp. 36–42, 1997.
- [80] H. Merkel, "private communication."
- [81] Zitex, "Saint-Gobain, France."
- [82] K. Fiegle, *Herstellung und Charakterisierung von supraleitenden diffusionsgekühlten Hot-Electron-Bolometern für Terahertz-Heterodynischer*. PhD thesis, Universität zu Köln, 1997.
- [83] M. Frommberger, *Herstellung und Charakterisierung supraleitender Nb und NbN Hot-Electron Bolometer Mischererelemente*. PhD thesis, Universität zu Köln, Juni 2001.
- [84] W. Ganzefles, *A Quasi-Optical THz Mixer Based on a Nb Diffusion-Cooled Hot Electron Bolometer*. PhD thesis, Technische Universiteit Delft, 2002.

- [85] A. Skalare, W. McGrath, B. Bumble, and H. LeDuc, "Large bandwidth and low noise in a diffusion-cooled hot-electron bolometer mixer," *Appl. Phys. Lett.*, vol. 68, no. 11, pp. 1558–1560, 1996.
- [86] B. Karasik, M. Gaidis, W. McGrath, B. Bumble, and H. LeDuc, "Low noise in a diffusion-cooled hot-electron mixer at 2.5 thz," *Appl. Phys. Lett.*, vol. 71, no. 11, 1997.
- [87] R. Wyss, B. S. Karasik, W. McGrath, B. Bumble, and H. L. Duc, "Noise and bandwidth measurements of diffusion-cooled nb hot-electron bolometer mixers at frequencies above the superconductive energy gap," *Proc. 10th Int'l Symp. on Space Terahertz Techn., University of Virginia*, pp. 215–228, 1999.
- [88] A. Skalare, W. Grath, B. Bumble, and H. G. LeDuc, "Frequency-domain analysis of diffusion-cooled hot-electron bolometer mixers," in *Proc. 10th Int'l Symp. on Space Terahertz Techn. University of Virginia*, March 1999.
- [89] H. Merkel, P. Khosropanah, D. W. Floet, P. Yagoubov, and E. Kollberg, "Conversion gain and fluctuation noise of phonon-cooled hot-electron bolometers in hot-spot regime," *IEEE Trans. Microwave Theory and Techn.*, vol. 48, p. 690, 2000.
- [90] B. Aune *et al.*, "Superconducting TESLA cavities," *Phys. Rev. Special Topics - ACCELERATORS AND BEAMS*, vol. 3, 2000.
- [91] M. Brüll, "private communication."
- [92] D. Allan, "Statistics of atomic frequency standards," *Proc. IEEE*, vol. 54, no. 2, p. 221, 1969.
- [93] Verband Deutscher Maschinen-und Anlagenbau VDMA.
- [94] Hannover Messe Industrie.

Danksagung

Ganz herzlich möchte ich mich bedanken bei:

Prof. Dr. Jürgen Stutzki für die Möglichkeit und die Unterstützung, diese spannende Arbeit am I. Physikalischen Institut der Universität zu Köln durchführen zu können,

Prof. Dr. Peter Reiter, der sich freundlicherweise bereit erklärt hat, das Zweitgutachten zu erstellen,

Prof. Dr. Michael Kerschgens für die Übernahme des Prüfungsvorsitzes,

Dr. Karl Jacobs, Leiter der HEB/SIS Mischerguppe, und Dr. Netty Honingh für die Leitung, Anleitung und Berichtigungen, sowie für das tatkräftigen Engagement den kleinen Mischern und ihren Partnern das Fliegen beizubringen,

der mechanischen Werkstatt des I. Physikalischen Instituts für die Fabrikation von astronomisch kleinen Hohlleiterstrukturen und anderen Werkstücken,

den vielen Mitstreitern und Vorstreitern der HEB/SIS Mischerguppe und der Empfängergruppe von KOSMA,

für die externe Beratung von Harald Merkel, Volker Lehman und Jian Liu,

meine Eltern für die umfassende Unterstützung und Beistand.

Erklärung

Ich versichere, dass ich die von mir vorgelegte Dissertation selbständig angefertigt, die benutzten Quellen und Hilfsmittel vollständig angegeben und die Stellen der Arbeit - einschließlich Tabellen, Karten und Abbildungen -, die anderen Werken im Wortlaut oder dem Sinn nach entnommen sind, in jedem Einzelfall als Entlehnung kenntlich gemacht habe; dass diese Dissertation noch keiner anderen Fakultät oder Universität zur Prüfung vorgelegen hat; dass sie - abgesehen von unten angegebenen Teilpublikationen - noch nicht veröffentlicht worden ist, sowie dass ich eine solche Veröffentlichung vor Abschluß des Promotionsverfahrens nicht vornehmen werde. Die Bestimmungen dieser Promotionsordnung sind mir bekannt. Die von mir vorgelegte Dissertation ist von Jürgen Stutzki betreut worden.

Michael Brandt

Teilpublikationen:

M. Brandt, J. Stodolka, C. Honingh, and K. Jacobs, "Superconducting hot electron bolometers on free-standing silicon nitride-membrane strips using flip-chip mounting," in *Proc. 13th Int'l. Symp. on Space THz Techn*, 2002.

M. Brandt, J. Stodolka, C. Honingh, and K. Jacobs, "Micromechanical waveguide mounts for HEB THz mixers," in *Proc. Far-IR, Sub-MM and MM Detector Techn. Workshop*, 2002.

M. Brandt, P. P. Muñoz, J. Stodolka, T. Tils, C. E. Honingh, and K. Jacobs, "Superconducting hot electron bolometers on fused quartz and on freestanding silicon nitride membrane strips," in *European Con. on Apl. Superconductivity*, 2003.

M. Brandt, P. P. Muñoz, S. Bedorf, T. Tils, C. E. Honingh, K. Jacobs, M. Brüll, and M. Wiedner, "Superconducting phonon cooled hot electron bolometers on freestanding silicon nitride membrane strips," *IEEE, Microwave and wireless components letters*, in prep.

Lebenslauf

Michael Brandt

Tübinger Straße 10
50739 Köln
Telefon: (0221) 170 6579

Geburtsdatum : 17. Dezember 1971
Geburtsort : London (GB)
Staatsangehörigkeit: Deutsch
Familienstand : nicht verheiratet

Schulausbildung:

1978 - 1982 kath. Grundschule Reumontstraße, Aachen
1988 - 1991 Gymnasium Viktoria Schule, Aachen
1991 Abitur

Studium:

1991 Lubos & Bayer, Maschinenbaupraktikum
Okt. 1992 – Dez. 1998 Physikstudium an der RWTH-Aachen
1994 Vordiplom in Physik
Dezember 1998 Abschluss der Diplomarbeit: *"Entwicklung eines Tieftemperatur- Rastersondenmikroskops zur Untersuchung von Nanostrukturen"*

Promotion:

Februar 1999 Beginn des Promotionsstudiums Promotion am
I. Physikalischen Institut der Universität zu Köln
April 2004 Abschluss der Doktorarbeit: *"Superconducting Hot Electron Bolometers on Silicon Nitride Membranes for Terahertz Waveguide Mixers"*

Beschäftigung:

Okt. 1992 – Dez. 1998 Studentische Hilfskraft
Feb. 1999 – Juni 2004 Wissenschaftliche Hilfskraft
1996-1997 Dr. Volker Klocke & Stephan Kleindiek Nanotechnologie,
Aachen, Nebentätigkeit
1998 Fries Research & Technology (FRT), Bergisch-Gladbach
Nebentätigkeit
2002-heute VDMA, Frankfurt/Main
Nebentätigkeit